# UNIVERSITÀ DELLA CALABRIA

**Facoltà di Scienze Matematiche Fisiche e Naturali**


Dottorato di ricerca in Fisica
XX ciclo

TESI
(Settore scientifico-disciplinare: FIS/04)

# Measurement of Deeply Virtual Compton Scattering cross sections at HERA and a new model for the DVCS amplitude


**Salvatore Fazio**

**Supervisori:**
Prof. Giancarlo Susinno

Dott.$^{ssa}$ Marcella Capua

**Coordinatore dottorato:**
Prof. Giovanni Falcone

**Alla memoria dei miei cari nonni**
**con riconoscenza ed affetto**

# Contents

# Introduction

The HERA electron-proton collider, in operation since 1992 to 2007, was a Deep Inelastic Scattering (DIS) facility dedicated to the study of the inner structure of the proton described, in the the framework of the Quantum Cromodynamics (QCD), the quantum field theory of the strong interactions, in terms of gauge bosons (gluons) exchange between partons (quarks and gluons).

Since the first operation period ZEUS and H1, the two experiments dedicated to the DIS physics at HERA, observed that an amount ($\sim$ 10%) of lepton-proton DIS events have a *diffractive origin*. The diffractive scattering is a particular process where the colliding particles scatter at very small angles and they either remain intact (elastic diffraction) or with the same quantum numbers (quasielastic diffraction) without any color flux in the final state. This involves a propagator carrying the quantum numbers of the vacuum, which is called Pomeron and is described within the Regge theory.

Previously diffractive events were studied only in soft interactions. The discover of a big amount of them in DIS regime opened a new area of studies in diffractive production mechanism, providing an hard scale which can be varied over a wide range and therefore it is an ideal testing for QCD models of diffractive scattering.

To improve the precision of DIS diffractive measurements in the ZEUS experiment was designed and installed the Leading Proton Spectrometer (LPS) which is a component of the main detector, operating till 2000 data taking period, composed of six silicon trackers along the proton beam pipe and it is dedicated to the high precision measurement of the momentum of the proton scattered at a very small angle and escaping the main ZEUS detector trough the beam hole.

The aim of this thesis is the study of a particular diffractive process called Deeply Virtual Compton Scattering (DVCS) for which perturbative QCD calculations are expected to be reliable and which open the possibility to extract Generalized Parton Distributions (GPD), containing more informations on the proton structure beyond the well known Parton Density

Functions (PDF). GPD generalize the ordinary PDF functions and show also informations about elastic form factors and the spin structure of the proton.

The GPD-based calculations will be very helpfull in the description of the Higgs boson production mechanism in the diffractive channel, which will be experimentally studied with the LHC accelerator at the CERN laboratory in Geneve.

This thesis presents the extraction of the DVCS cross sections from the data collected by ZEUS during the 1999 - 2000 $e^+p$ HERA running period as a function of $Q^2$, the four-momentum transferred at the lepton vertex, $W$, the energy available in the $\gamma^*p$ centre of mass and $t$, the four-momentum transferred at the proton vertex. In particular the DVCS differential cross section as a function $t$, directly measured with the LPS spectrometer, has been measured and will be presented here for the first time. Moreover a new model for DVCS amplitude in the framework of the Regge theory was proposed [1], tested on experimental data and presented in this work.

This thesis is organized as follows:

The first chapter of this work gives an overview on the DIS physics at HERA and an introduction to the diffractive physics and the DVCS process. The second chapter describes the ZEUS detector. The third chapter contains the Monte Carlo simulation used in this analisis. In the fourth chapter, the event reconstruction procedure is summarized and, in the fifth chapter, the DVCS selection and background subtraction strategy is introduced. The sixth chapter shows the cross section measurement procedure and the achieved experimental results and finally, in the last chapter, the new theoretical model proposed for the DVCS amplitude description in the framework of the Regge theory is presented.

# Chapter 1

# Theoretical background

HERA is an accelerator designed for the Deep Inelastic Scattering (DIS) events production. A relevant sample ($\sim 10\%$) of the total amount of DIS events collected by ZEUS and H1 experiments at HERA contains diffractive events, for which the interaction is described by an excange of a particle carrying the quantum numbers of the vacuum.

Deeply virtual Compton scattering (DVCS) is a diffractive *ep* interaction observed in the deep inelastic scattering (DIS) regime. This process provides the possibility to extract information on the internal structure of the proton via generalised parton distributions (GPD). In the following, the theoretical bases for DIS and diffractive physics are presented together with a description of DVCS processes and the experimental results already achieved.

## 1.1 Lepton-proton scattering

In lepton-proton scattering the lepton, considered as a point-like particle, interacts via the electromagnetic or weak force with the proton, which has a complex substructure. Two types of processes in *ep* scattering can be distinguished: neutral current (NC) and charge current (CC) processes. In NC processes a virtual photon $\gamma^*$ or a $Z^0$ boson is exchanged and the lepton flavour is conserved. In CC processes the outgoing lepton is a neutrino or antineutrino as a consequence of the $W^\pm$ boson exchange. The NC interaction can be described by the exchange of a photon transferring a four-momentum $q$ from the lepton to the proton as shown in fig. 1.1. The contribution from $Z^0$ and $W^\pm$ exchange is neglected in the kinematic range of this analysis. The relevant variables are the four-momenta of the incoming lepton $k$, of the scattered lepton $k'$, of the initial proton $P$ and of the hadron final state $P'$.

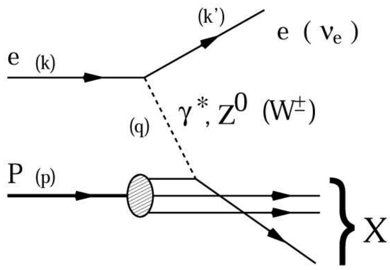


Figure 1.1: Diagram of a typical *ep* scattering by a neutral or charged current exchange.

The following variables provide a relativistically invariant formulation of the inelastic ep event kinematics[1]

- the centre-of-mass energy squared

$$s = (P + k)^2 \approx 4E_e E_p \tag{1.1}$$

where $E_e$ and $E_p$ are the energies of the incoming lepton and proton beam, respectively,

- the negative square of the exchanged photon four-momentum

$$Q^2 = -q^2 = -(k - k')^2 \tag{1.2}$$

which is also called virtuality,

- the fraction of the incoming lepton energy carried by the virtual photon in the rest frame of the initial state proton

$$y = \frac{P\cdot q}{P\cdot k} \qquad 0 \le y \le 1 \tag{1.3}$$

which is also known as inelasticity,

- the fraction of the proton momentum carried by the struck quark

$$x = \frac{Q^2}{2P\cdot q} \approx \frac{Q^2}{sy} \qquad 0 \le x \le 1 \tag{1.4}$$

- the photon-proton centre-of-mass energy squared

$$W^2 = (q + P)^2 \approx \frac{Q^2}{x}(1 - x) \tag{1.5}$$

Quantities $x$ and $y$ are also called Bjorken scaling variables.

[1] In this thesis the natural system of units is used, where $\hbar = c = 1$

# 1.2 Deep inelastic scattering

Deep Inelastic Scattering (DIS) is a high $Q^2$ process in which leptons scatter off protons at large transverse momenta and a substantial number of particles can be produced with high total invariant mass.

The scattering process is referred as *inclusive* when only a scattered lepton is detected and all other particles are recognised as the hadronic final state and summed over. Another type of scattering is the *exclusive* process, in which usually all final-state particles are determined. The kinematics of inclusive DIS events for a given centre-of-mass energy can be described by any two independent relativistic invariant variables defined in Sec. 1.1.

## 1.2.1 Cross section and structure functions

The $ep$ cross section in a general formalism can be expressed as a function of the leptonic $L^{\mu\nu}$ and hadronic tensor $W_{\mu\nu}$ describing the lepton and proton vertices of the diagram in fig. 1.1

$$d\sigma \propto L^{\mu\nu} W_{\mu\nu}. \tag{1.6}$$

The leptonic tensor is calculable in Quantum Electrodynamics (QED), while the hadronic one can not be calculated from first principles due to extended hadronic structure but must be parametrised in terms of functions. Symmetry properties, gauge invariance and conservation laws of QED allow to reduce the hadronic tensor for unpolarised ep scattering to two real functions $W_1$ and $W_2$, which are $x$- and $Q^2$-dependent. Thus, the hadronic tensor can be expressed as

$$\begin{aligned} W_{\mu\nu} = & \left(-g_{\mu\nu} + \frac{q_\mu q_\nu}{q^2}\right) W_1(x,Q^2) \\ & + \left(P_\mu - \frac{P\cdot q}{q^2} q_\mu\right)\left(P_\nu - \frac{P\cdot q}{q^2} q_\nu\right) \frac{W_2(x,Q^2)}{m_p^2}, \end{aligned} \tag{1.7}$$

where $m_p$ denotes the proton mass, $g_{\mu\nu}$ is the metric tensor, $q$ and $P$ represent the virtual photon and proton four-momenta, respectively.

The proton structure functions are related to $W_1$ and $W_2$ via

$$F_1(x,Q^2) = m_p W_1(x,Q^2) \qquad \text{and} \qquad F_2(x,Q^2) = \nu W_2(x,Q^2), \tag{1.8}$$

where $\nu = q\cdot \frac{P}{m_p}$ is the energy transferred from the lepton to the proton in the proton rest frame. The cross section for unpolarised NC events can now be written as

$$\frac{d^2\sigma^{NC}}{dxdQ^2} = \frac{2\pi\alpha^2}{xQ^4}\left[\left(1+(1-y)^2\right)F_2(x,Q^2) - y^2 F_L(x,Q^2)\right], \tag{1.9}$$

where $F_L = F_2 - 2xF_1$ and $\alpha$ is the fine structure constant. The structure function $F_3$, which measures parity violating contributions resulting from $Z^0$ exchange, contributes only at $Q^2 \gg 10^3\ GeV^2$ and has been omitted.

The *ep* cross section can be interpreted as the product of the virtual photon flux [4]

$$\Gamma = \nu - \frac{Q^2}{2m_p}, \tag{1.10}$$

and the total cross section $\sigma_{tot}^{\gamma^* p}$ for scattering of virtual photons on the proton

$$\sigma^{ep} = \Gamma \cdot \sigma_{tot}^{\gamma^* p}, \tag{1.11}$$

were $\sigma_{tot}^{\gamma^* p}$ is split to the cross sections for scattering of transverse $\sigma_T^{\gamma^* p}$ and longitudinally $\sigma_L^{\gamma^* p}$ polarised photons

$$\sigma_{tot}^{\gamma^* p} = \sigma_T^{\gamma^* p} + \sigma_L^{\gamma^* p}. \tag{1.12}$$

The relations between the structure functions and the virtual photon-proton cross sections can be expressed as

$$F_2(x, Q^2) \approx \frac{Q^2}{4\pi^2\alpha}\left(\sigma_T^{\gamma^* p} + \sigma_L^{\gamma^* p}\right), \tag{1.13}$$

$$F_L(x, Q^2) \approx \frac{Q^2}{4\pi^2\alpha}\left(\sigma_L^{\gamma^* p}\right), \tag{1.14}$$

where the approximations are valid for small values of $x$. In the kinematic region of not too large $y$ the contribution of $F_L$ can be neglected and the cross section mainly depends on $F_2$.

In fig. 1.2 measurements of the structure function $F_2$ is depicted as a function of $Q^2$ for different values of $x$. One can see that $F_2$ is independent on $Q^2$ at large values of $x$. This was first observed at SLAC [5] for $Q^2 < 7$ GeV$^2$ and $0.02 < x < 0.2$ and is known as *scaling* or *scale invariance*. In fact, at low $x$, a rapid increase of $F_2$ with $Q^2$ has been observed [6], while $F_2$ decreases at large values of $x$. This $Q^2$ dependence of $F_2$ for fixed $x$ is known as *scaling violation*. The interpretation of the onset of scaling, where $F_1$ and $F_2$ can be written as functions of only one variable, $F(x, Q^2) = F(x)$, is that the virtual photon no longer scatters off the whole target proton but only off a part of the proton being a consequence of its partonic structure [7]. The discovery of a substructure of the proton led to the formulation of the *Quark Parton Model* (QPM), in which the proton consists of three point-like partons which can be identified with the quarks introduced by Gell-Mann and Zweig [8] to explain the spectroscopic hadron data. The $Q^2$-independent

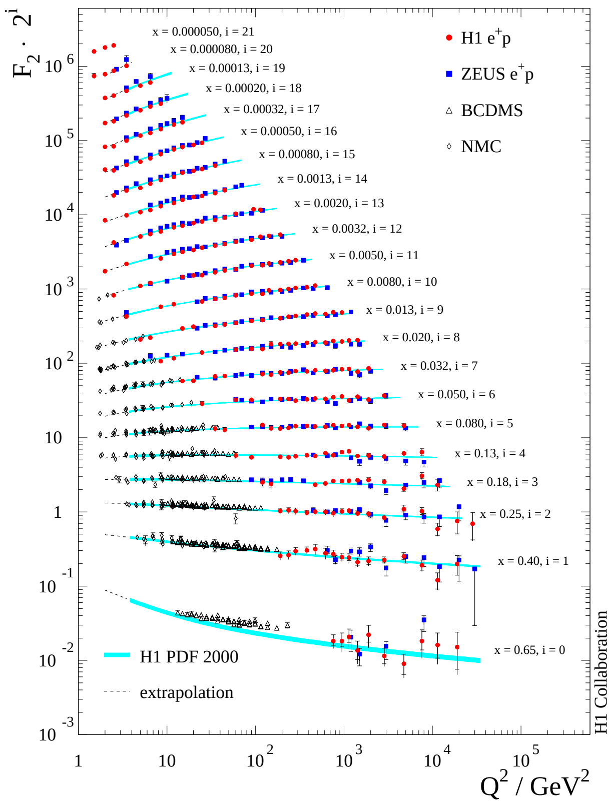


Figure 1.2: The structure function $F_2$ as a function of $Q^2$ for fixed values of $x$. The HERA results are shown together with fixed target results and NLO QCD fit.

structure functions $F_1$ and $F_2$ can be related to the parton density functions $f_i$ of the proton via

$$F_1(x) = \frac{1}{2} \sum_i e_i^2 f_i(x), \tag{1.15}$$

$$F_2(x) = x \sum_i e_i^2 f_i(x), \tag{1.16}$$

where the sums are over the parton flavour $i$ weighted by the corresponding parton charge squared $e_i^2$. The parton density functions are interpreted in the QPM as the probability to find a parton of type $i$ with the momentum fraction $x$ in the proton.

Experimentally it was found that only half of the proton momentum is carried by charged quarks [9]. The other half is carried by neutral partons which are identified with gluons, the mediators of the strong interactions.

### 1.2.2 Quantum Chromodynamics

Quantum Chromodynamics (QCD) is the quantum field theory developed in the 1970's to describe the strong interactions between quarks. It assumes that the proton is built up from quarks which are spin 1/2 fermions. They are bounded together by gluons which are the spin 1 gauge bosons mediating the strong forces. QCD is a non-abelian gauge theory based on the SU(3) symmetry group. Quarks carry one of three possible colour charges (red, green or blue). Gluons also carry colour charge and thus couple to each other.

In contrast to QED, the QCD coupling constant $\alpha_s$ increases at large distances (low $Q^2$) and decreases at small distances (large $Q^2$). This is known as *asymptotic freedom*. $\alpha_s$ can be approximated as

$$\alpha_s(Q^2) = \frac{12\pi}{(33 - 2n_f)ln(Q^2/\Lambda^2_{QCD}} \tag{1.17}$$

where $n_f$ is the number of active quark flavours for which $m_q^2 < Q^2$. The $\Lambda^2_{QCD}$ quantity is the QCD scale parameter which has to be determined by experiment. It determines the energy at which $\alpha_s$ decreases logarithmically and where $\Lambda^2_{QCD} \ll Q^2$ perturbative QCD (pQCD) can be applied.

The factorisation theorem states that short range effects in the scattering amplitude, calculable in pQCD, can be separated from the non-perturbative long range effects which are expressed by the parton distribution functions (PDF). The factorisation theorem was proven for hard scattering [10]. It defines the inclusive structure function as

$$F_2(x, Q^2) = \sum_{i=q,\bar{q},g} \int_x^1 dx' C_i \left( \frac{x}{x'}, \alpha_s(\mu_F^2), \frac{Q^2}{\mu_F^2} \right) f_i(x', \mu_F^2), \tag{1.18}$$

where $C_i$ denotes the coeffcient functions responsible for short range interactions and $f_i$ are PDF which have to be determined experimentally. They are specific to the type of hadron. Quantity $\mu_F^2$ is the factorisation scale which determines the separation line between what is considered as the long range inner dynamics of the proton ($f_i$) and the dynamics of the hard lepton-parton interaction ($C_i$).

### 1.2.3 Radiative *ep* scattering

Higer order QED effects, such as emission of real photons and loop corrections, contribute to the *ep* cross section. Among these processes, only the real photon emission can be experimentally detected. The lowest order Feynman diagrams of the emission of a real photon from the lepton are depicted

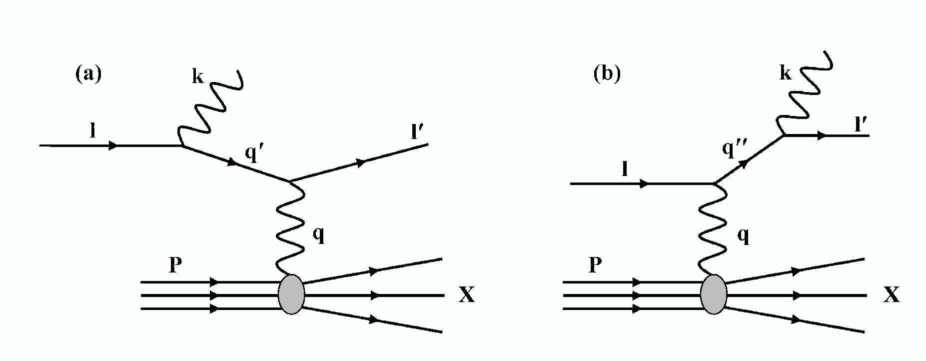


Figure 1.3: Lowest order Feynman diagrams for the emission of a real photon from the electron line.

in fig. 1.3 and the corresponding amplitude contains in the denominator, respectively, the following propagator terms

$$(q'^2 - m_e^2)q^2, \tag{1.19}$$

$$(q''^2 - m_e^2)q^2, \tag{1.20}$$

where $q'$, $q''$ and $q$ are the four-momenta of the corresponding leptons. The dominant contributions appear when these terms tend to zero and according with this the following classification [11] is given

- $q'^2 \simeq 0$ (or $q''^2 \simeq 0$) and $q^2 \simeq 0$. This configuration corresponds to the *bremsstrahlung processes*. The electron and the photon scatter with very small polar angles. This process has a high cross section and it is used to measure the luminosity in the ZEUS experiment (see Sec. 2.2.8).

- $q^2$ is finite and either $q'^2 \simeq 0$ or $q''^2 \simeq 0$. In this configuration the photons are emitted either with the initial or final electron. The first case is called Initial State Radiation (ISR) and its cross section is dominated by the process in fig. 1.3a. this process can be interpreted as a DIS event with a reduced center of mass. The second possibility is referred to as Final State Radiation (FSR). These events usually can not be distinguished from a normal DIS event. The small angles at which the photon is emitted with respect of the electron direction makes the experimental separation between the two is not possible.

- $q^2 \simeq 0$ and either $q'^2$ or $q''^2$ are finite. This configuration corresponds to the case in which the electron and the photon are detected at large polar angles and their total transverse momentum is close to zero. This configuration is called QED Compton scattering since it involves the scattering of a quasi-real photon on an electron.

## 1.3 Diffraction

Diffractive interactions [12, 13] were first observed in hadron-hadron elastic scattering, $A + B \to A + B$. Later they were generalised to processes where one ($A + B \to X + B$ single dissociation) or both ($A + B \to X + N$ double dissociation) colliding hadrons were transformed to multi-particle final states without exchange of quantum numbers between the scattered hadrons. It implies that no colour charge is exchanged, thus there is no colour field operating between the two outgoing systems $X$ and $N$.

Diffractive events are recognised by the final-state hadron detected at large values of rapidity[2] and a gap in rapidity between the final states $A$ and $B$ was observed [14], where in the more general case the states $A$ and $B$ correspond to $X$ and $N$. The rapidity gap is the consequence of a small exchange of transverse momentum, so the final-state particles move with momenta close to those of the initial ones. It was also observed that the basic features of diffractive processes seem to be independent of the type of the incoming hadron.

So far there is a lack of one model describing correctly all aspects of the diffractive process. This type of reactions belongs mostly to the soft physics, mainly described by the phenomenological models only. Soft processes take place at low energies and are characterised by low transverse momenta, while at high energies hard interactions are observed. One of the soft models, widely used to compare its predictions with measurements in diffractive physics, is the Regge phenomenology [2].

In the Regge theory, the elastic hadron-hadron scattering is described by exchange of one or more Reggeons. The Reggeon is equivalent to a superposition of particles (mesons or baryons) with the same quantum numbers except for spin. For the particle spin plotted as a function of the mass squared, the particles corresponding to a specific Reggeon lie on a Regge trajectory which can be approximated by the straight line [15]. This theory succeeded in predictions for the elastic cross section, which was found to fall initially with increasing centre-of-mass energy, but then levels off and show a slight rise. The initial fall can be described by the Reggeon trajectory, while the rise can be fitted to a new Pomeron trajectory (IP) [16]. The growth of the cross section was first predicted by Pomeranchuk [17] and the trajectory was named after him. The IP has the quantum numbers of the vacuum and is generally thought as the mediator in the diffractive scattering.

[2]The rapidity of a particle with energy $E$ and longitudinal momentum $p_{||}$ is defined as $y = \frac{1}{2} \ln \frac{E+p_{||}}{E-p_{||}}$, which can be approximated by the pseudorapidity $\eta = -\ln \tan \frac{\theta}{2}$, in the limit where the particle mass is small and $\cos\theta = p_{||}/E$.

In the QCD based models for the IP exchange, diffractive process is described by a quark-antiquark or two-gluon exchange.

### 1.3.1 Diffraction in DIS

At HERA, diffractive events have been observed in photoproduction [18] as well as in electroproduction [14] DIS regimes. Photoproduction refers to processes where the lepton is scattered at a small angle, emitting a quasi-real photon with $Q^2 \approx 0$, which then interacts with the proton, while electroproduction denotes processes with a virtual-photon exchange with $Q^2 \gg 0$.

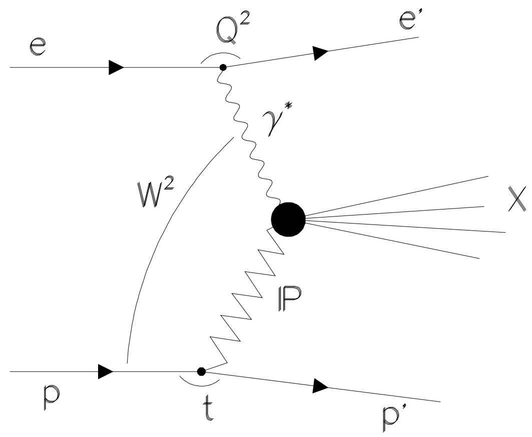


Figure 1.4: Diagram of a diffractive $ep$ process.

Diffractive processes in DIS at HERA are generally of the form

$$e(k) + p(P) \to e(k') + N(P_N) + X(P_X);$$

where $X$ denotes the final state originating from the dissociated photon and $N$ is the final state of the proton. The general diagram of a diffractive $ep$ process is shown in fig. 1.4.

For a complete description of diffractive events further kinematic variables, in addition to the usual DIS variables defined in Sec. 1.1, are introduced:

- the square of the four-momentum transfer at the proton vertex

$$t = (P - P_N)^2, \tag{1.21}$$

- mass of the hadronic system $X$ produced by the photon dissociation $M_X$,

- the fraction of the proton momentum carried by the IP

$$x_{IP} = \frac{(P - P')q}{P\cdot q} \approx \frac{M_X^2 + Q^2}{W^2 + Q^2}, \tag{1.22}$$

- the fraction of the struck quark momentum carried by the IP

$$\beta = \frac{Q^2}{2(P - P')\cdot q} = \frac{x}{x_{IP}} \approx \frac{Q^2}{M_X^2 + Q^2}. \tag{1.23}$$

The basic features of diffractive processes can be summarised as follows:

- The differential cross section, $d\sigma/dt$, displays a sharp exponential fall

$$\frac{d\sigma}{dt} \propto e^{-b|t|}, \tag{1.24}$$

  with the slope parameter, $b = R^2/4$, where $R$ is the transverse radius of the interaction. It typically increases slowly with energy $\sqrt{s}$ which is known as *shrinkage of the forward diffractive peak*. The $b$ slope for $\gamma^* p \to Vp$ is observed to fall with $Q^2$ for light vector mesons and it is constant for heavier ones.

- The diffractive cross section is characterised by a weak dependence on the energy $\sqrt{s}$ given by

$$\sigma^{tot} \propto s^{\epsilon}$$

  where $\epsilon = 0.08$ was found experimentally [19].

- For single dissociation $AB \to XB$, the small masses $M_X$ of the system $X$ are preferred and the cross section behaves like

$$\frac{d\sigma^{AB\to XB}}{dM_X^2} \propto \frac{1}{(M_X)^n}, \tag{1.25}$$

  where $n \approx 2$ [13].

- The $W$ dependence of the $\gamma * p \to Vp$ cross section is expected to have a form

$$\sigma \propto W^{\delta},$$

  where the exponent $\delta$ grows from 0.2 for soft interactions towards higher values for hard processes.

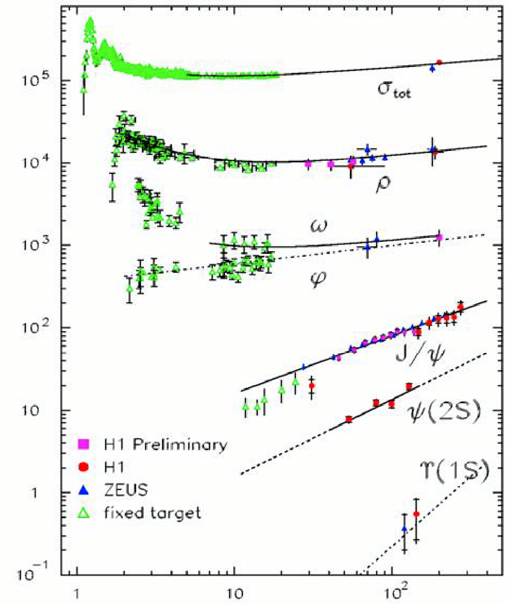


Figure 1.5: On the left, the $b$ slope dependence on $Q^2$ for the $\gamma^* p \to Vp$ process, where $V = \rho, \omega, \phi, J/\psi, \psi(2S)$. On the right the elastic vector-meson cross sections as a function of $W$ measured in photoproduction at HERA compared to the measurements at low energy and to the total cross section. The lines illustrate a comparison of various power-law energy dependence at high energy.

Figure 1.3.1 shows the vector-meson elastic cross sections $\gamma p \to Vp$ with $V = \rho, \phi, \omega, J/\psi, \Upsilon(1S)$ as functions of $W$ for the photoproduction regime. The $\sigma \propto W^t$ is imposed on the data. The rise of the cross section for the production of light vector mesons $(\rho, \omega, \phi)$ can be described in the framework of the Regge theory by the exchange of the IP trajectory known for soft diffractive interactions. In the case of $J/\psi$ and $\Upsilon$ photoproduction the rise of the cross section is steeper than predicted by the Regge formalism. For light vector mesons this steeper rise can be achieved at higher $Q^2$ values.

## 1.4 Generalised parton distributions

Generalised parton distributions (GPD) [20, 21, 22, 23, 24, 25, 26] parametrise the complex structure of the proton (or more generally nucleon) independently on the reaction which probes the target.

The GPD contain information on the correlations between quarks and on their momentum dependence. Moreover, they enable access to the quark spin and the quark orbital momentum of the proton spin unreachable elsewhere [20]. The traditional inclusive PDF extracted from DIS allow to access only parton densities.

If the leading order pQCD amplitude for the certain process in the forward direction ($t = 0$ and equal helicities of the initial and final proton) can be factorised in a hard scattering part exactly calculable in pQCD and a non-perturbative proton structure part, the structure of the proton can be parametrised in terms of four GPD (see fig. 1.6). They are traditionally denoted $H, \tilde{H}, E, \tilde{E}$ and depend on three variables $x$, $\xi$ and $t$, where $\xi$ is called *skewedness*. The quantity $x + \xi$ denotes the longitudinal momentum fraction carried by the initial quark struck by the virtual photon and similarly $x - \xi$ relates to the final quark going back to the proton. Therefore, $-2\xi$ is the longitudinal momentum difference between the final and initial quarks.

The standard PDF are defined on the cross-section level whereas the GPD are defined on the amplitude level, i.e. when calculating cross sections, the GPD enter calculations of the scattering amplitude which further is squared to obtain the cross-section expression.

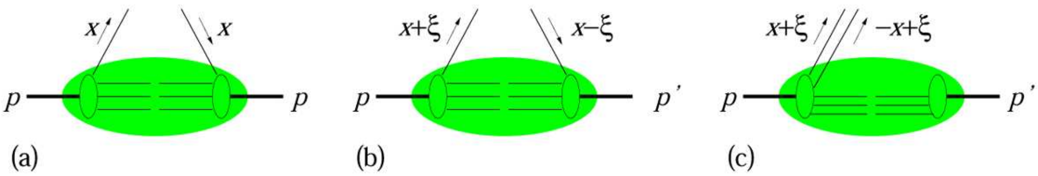


Figure 1.6: Diagrams representing the adronic matrix elements: *a*) for standard DIS and *b*) and *c*) for the generalised parton distributions. In contrast to parton densities in standard DIS the GPD's are defined by hadronic matrix elements of unequal hadronic wave functions. One distinguishes between the DGLAP *b*) and ERBL *c*) region.

The GPD for quarks of flavour q can be defined by Fourier transforms of the hadronic matrix

$$\int \frac{d\lambda}{2\pi} e^{i\lambda x} \langle p'|\bar{\psi}_q(-\lambda/2)\gamma^\mu \psi_q(\lambda/2)|p'\rangle = H_q \bar{u}(P')\gamma^\mu u(P) + E_q \bar{u}(P') \frac{i\sigma^{\mu\nu}\,\Delta_\nu}{2m_p} u(P) \tag{1.26}$$

and

$$\int \frac{d\lambda}{2\pi} e^{i\lambda x} \langle p' | \bar{\psi}_q(-\lambda/2)\gamma^\mu \gamma_5 \psi_q(\lambda/2) | p' \rangle = H_q \bar{u}(P')\gamma^\mu \gamma_5 u(P) + E_q \bar{u}(P') \frac{\Delta^\mu \gamma_5}{2m_p} u(P), \quad (1.27)$$

where $|p\rangle$ and represent the quantum numbers of the incoming and outgoing proton, respectively,including differences for the spin state, $\bar{\psi}_q(-\lambda/2)\gamma^\mu\psi_q(\lambda/2)$ and $\bar{\psi}_q(-\lambda/2)\gamma^\mu\gamma_5\psi_q(\lambda/2)$ are operators which select the quark with certain properties from the hadronic wave functions, $\bar{u}$ and $u$ represent the Dirac spinors of the proton and $\Delta^\mu = P'^\mu P^\mu$.

$H$ and $E$ are spin-independent and are also called the unpolarised GPD, whereas $\tilde{H}$ and $\tilde{E}$ are spin-dependent and are usually called the polarised GPD. Actually $H$ and $\tilde{H}$ are a generalisation of the PDF measured in DIS, which in the forward direction reduce to the quark distributions ($H$) and to the quark helicity distributions ($\tilde{H}$). Furthermore, there are formulae which relate the first moment of the GPD to the elastic proton form factors.

## 1.5 Deeply virtual Compton scattering

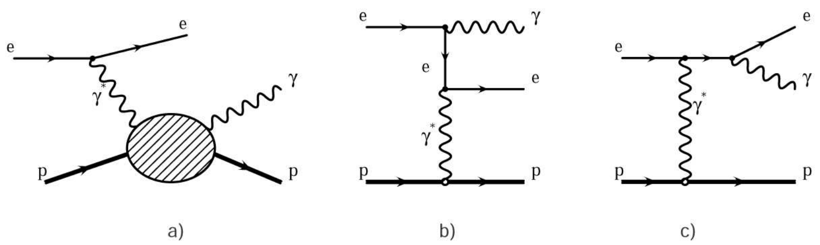


Figure 1.7: Diagram of the DVCS (a) and BH processes for a photon emitted from the initial (b) and final (c) lepton line.

The deeply virtual Compton scattering (DVCS) is a diffractive electroproduction of a real photon in DIS. For the $ep$ collisions this process can be written as

$$e(k) + p(P) \rightarrow e(k') + \gamma + p(P') \quad (1.28)$$

with diagram depicted in fig. 1.7a. In this process the proton can either remain intact (elastic case), be excited into a resonant state (quasi-elastic) or be broken up (inelastic).

The DVCS diagram is similar to that for diffractive processes (see fig. 1.4), where a hadronic system is a vector meson. From the theory point of view, DVCS has a very important feature compared to its hadronic counterpart, because of the photon in a final state, whose wave function is known. In the vector-meson case, assumptions about vector-meson wave functions are necessary, increasing the theoretical uncertainty. A further advantage of studying the DVCS process comes from the fact that the cross section goes as $1/Q^6$ compared to $1/Q^8$ in the vector-meson case [27]. The DVCS process appears to be the least suppressed in $Q^2$ of all known exclusive hard diffractive processes.

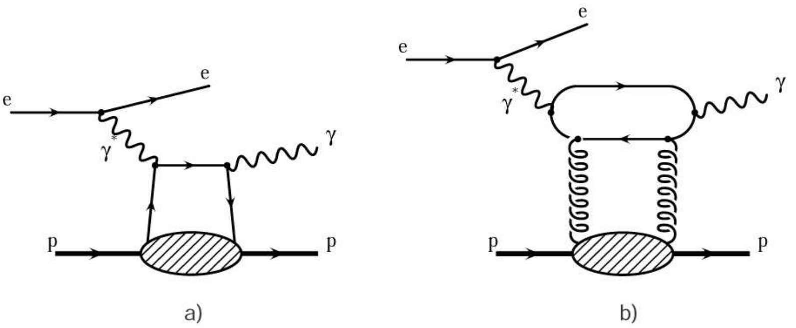


Figure 1.8: The QCD diagrams of the DVCS process in LO (a) and NLO (b) in QCD.

It has been shown [20, 28, 22, 23] that for high $Q^2$ the DVCS amplitude factorises to a hard scattering coefficient, which is calculable in pQCD, and a soft part which is involved in the GPD. The leading (LO) and next-to-leading (NLO) order diagrams of the DVCS process in QCD are shown in fig. 1.8a and 1.8b, respectively. In the LO process, $\gamma^*$ scatters off the quark originating from the proton, while in the NLO diagram $\gamma^*$ interacts via a quark loop with two gluons from the proton. In both cases the real photon is emitted from the quark loop.

The LO diagram also helps to understand the concept of GPD. In order to bring the outgoing photon onto its mass shell, the fraction of the proton momentum carried by the initial and final quark can not be the same. By studying DVCS, one investigates what happens when one removes a quark from the proton of one given momentum, and replaces it with a quark of another momentum. Thus one probes two-particle correlations in the proton.

The DVCS final state is identical to those of the Bethe-Heitler (BH) process (see fig. 1.7b and 1.7c), so the two processes interfere.

The final-state amplitude $\mathcal{A}$ is the sum of amplitudes for DVCS ($\mathcal{A}_{DVCS}$)

and BH ($\mathcal{A}_{BH}$), so

$$|\mathcal{A}|^2 = |\mathcal{A}_{DVCS}|^2 + |\mathcal{A}_{bh}|^2 + \mathcal{I}, \tag{1.29}$$

with the interference term

$$\mathcal{I} = \mathcal{A}_{DVCS}\mathcal{A}^*_{BH} + \mathcal{A}^*_{DVCS}\mathcal{A}_{BH}, \tag{1.30}$$

where the latter can also be written as

$$\mathcal{I} = 2(\mathfrak{Re}\mathcal{A}_{DVCS}\mathfrak{Re}\mathcal{A}_{BH} + \mathfrak{Im}\mathcal{A}_{DVCS}\mathfrak{Im}\mathcal{A}_{BH}). \tag{1.31}$$

If one defines an azimuthal angle $\phi$ as the angle between the lepton and hadron scattering planes in the centre-of-mass of the virtual photon-proton system, the azimuthal angular dependences of the terms in (1.29) and in (1.30) arise from the contraction of the leptonic and hadronic tensors [29]. The DVCS amplitude for a given helicity $\lambda$ of the intermediate photon $\gamma*$ depends on $\phi$ as

$$\mathcal{A}_{DVCS} \propto \exp i\lambda\phi, \tag{1.32}$$

while the BH amplitude has generally a complicated $\phi$ dependence, which at the leading order of $1/Q^2$ simplifies to

$$\mathcal{A}_{DVCS} \propto \exp i\lambda\phi + \mathscr{O}\left(\frac{1}{Q^2}\right) \tag{1.33}$$

for a scattered photon of helicity $\lambda'$.

It was shown [30] that these different spin dependences of $A_{DVCS}$ and $A_{BH}$ lead to a non-vanishing $\phi$ dependence of $I$, which in LO for unpolarised ep scattering yields a contribution to the cross section proportional to $\cos\phi$. This has a consequence in non-zero azimuthal-angle asymmetry [5, 9, 41] and beam-charge asymmetry [29], which can be investigated looking for a proton and electron or positron in the same and opposite hemispheres of a detector. Both the asymmetries are defined in a way to be directly related to the interference term. Thus, measuring them, one gets access to $\mathfrak{Re}\mathcal{A}_{DVCS}$. Moreover, for polarised *ep* scattering, different $\phi$ dependence appears for different beam polarisations, so the beam-spin asymmetry [29], which is proportional to $\mathfrak{Im}\mathcal{A}_{DVCS}$, can be investigated. The measurements of different contributions to the cross section yield a possibility to extract the GPD.

In the kinematic region investigated here, the azimuthal-angle asymmetry, thus also the interference term, is predicted to be fairly sizeable [32, 26] already for small $t$. Moreover, this asymmetry strongly depends on the energy.

Nevertheless, in this analysis the interference term is assumed to be zero due to integration over all $\phi$ angles. Therefore, the BH contribution to the cross section for the process (1.28) can be subtracted and the DVCS cross section can be measured.

The apparent simplicity of the DVCS process makes it a new and powerful tool to study the following aspects of QCD in the field of diffraction:

- the $\gamma * p \to \gamma p$ cross section can be measured,
- the interference of DVCS with BH allows the measurement of the real part of the QCD amplitude,
- the DVCS process can provide an indirect measurement of GPD,
- the DVCS cross section is proportional to the square of the inclusive proton structure function $F_2$, and therefore provides additional information on $F_2$ at low $x$.

### 1.5.1 GPD-based models

The first calculation of the DVCS cross section for the HERA kinematic region was given by Frankfurt, Freund and Strikman [33] (FFS model). In this model, the DVCS ep and $\gamma^* p$ cross sections and the interference term are related to the inclusive structure function $F_2$ as

$$\frac{d^3\sigma^{ep}_{DVCS}}{dxdQ^2dt} = \frac{\pi^2\alpha^3}{2xR^2Q^6}[1+(1-y)^2]e^{-b|t|}F_2^2(x,Q^2)(1+\rho^2), \tag{1.34}$$

$$\sigma^{\gamma^* p}_{DVCS}(W,Q^2) = \frac{\pi^3\alpha^2}{2xR^2Q^4}F_2^2(x,Q^2)(1+\rho^2), \tag{1.35}$$

$$\frac{d^4\sigma^{ep}_{INT}}{dxdQ^2dtd\phi} = \frac{\pm\rho\alpha^3 y[1+(1-y)^2]}{2RxQ^5\sqrt{|t|(1-y)}}e^{-b|t|/2}. \tag{1.36}$$

$$\cdot F_2(x,Q^2)\frac{G_E(t)+\frac{|t|}{4m_p^2}G_M(t)}{1+\frac{|t|}{4m_p^2}}\cos\phi, \tag{1.37}$$

where $x \simeq Q^2/(Q^2+W^2)$ is the Bjorken scaling variable, $\phi$ is the angle between the lepton and proton scattering planes calculated in the virtual photon-proton centre-of-mass system, $b$ is the exponential slope of the $t$ dependence, $y$ is the inelasticity and $G_E(t)$ and $G_M(t)$ are the electric and magnetic proton form factors, respectively. The "+"sign in the interference term corresponds to an electron and the "-"sign corresponds to the positron. The ratio $\mathfrak{Re}\mathcal{A}_{DIS}(\gamma^* p \to \gamma p)|_{t=0}/\mathfrak{Im}\mathcal{A}_{DVCS}(\gamma^* p \to \gamma p)|_{t=0}$ accounts for the non-forward character of the DVCS process and is directly related to a ratio of the GPD to PDF [34] and $\rho = \mathfrak{Re}\mathcal{A}_{DVCS}(\gamma^* p \to \gamma p)|_{t=0}/\mathfrak{Im}\mathcal{A}_{DVCS}(\gamma^* p \to \gamma p)|_{t=0}$. The value of $R$, calculated in the leading order QCD evolution of the GPD, is about 0.55, with a little dependence on $x$ or $Q^2$ [33]. The value of $b$ is expected to depend on both $W$ and $Q^2$. At high $Q^2$ and very small $x$, $b$ is expected to increase with $W$ [33].

In a more formal approach [28], it has been proven that in the limit $Q^2 \to \infty$, the DVCS amplitude factorises into a hard scattering coeffcient, calculable in pQCD and a soft part which can be included to the GPD. The kernels of the evolution equations for the GPD are known to next-to-leading order [35] and thus the GPD can be evaluated at all $Q^2$, given an input at some starting scale $Q$. At present, measurements of the DVCS cross section are essential in modelling the input GPD [34, 35].

### 1.5.2 Colour-dipole models

The DVCS cross section can also be calculated within the colour-dipole models (CDM) [36, 37], which have been successful in describing both the inclusive and the diffractive DIS cross sections at high energy [38, 31].

In the proton rest frame, the DVCS process can be seen as a succession in time of three factorisable subprocesses. The incoming virtual photon fluctuates into a quark-antiquark pair (colour dipole) before the interaction with the proton, then this colour dipole interacts with the proton target and finally the quark pair annihilates to a real photon in time much longer than the interaction time with the target.

In this approach the amplitude of the DVCS process can be written as

$$\mathcal{A}_{DVCS} = \int_{R,z} \psi^{in}_{\gamma^*} \sigma_d \psi^{out}_{\gamma^*}, \tag{1.38}$$

where $\psi^{in}$ and $\psi^{out}$ are the incoming virtual photon and the outgoing real photon wave functions, respectively, which are well known from QED. The cross section $\sigma_d$ describes interaction of the dipole with the proton and is substantially affected by a non-perturbative content. The integral goes over all transverse dipole sizes $R$ and all longitudinal momentum fractions $z$ of the quark in the dipole. $\sigma_d$ is usually assumed to be flavour- and z-independent. The parameters of a model are obtained from an adjustment to data.

A lot of realisations of the dipole approach to DVCS exist, which differ in the formulation of the dipole cross section. In particular, the model by Donnachie and Dosch [31] is based on the concept of soft and hard Pomeron exchange. In this approach small dipoles interact predominantly by the exchange of the hard IP component while large dipoles interact via the soft IP component. The model by Forshaw, Kerley and Shaw [39, 40] uses the Regge phenomenology. It assumes that $\sigma_d$ depends only on the properties of the dipole-proton system described by $W$ and $R$, and does not depend on $Q^2$. The model by McDermott, Frankfurt, Guzey and Strikman [41, 40] incorporates the QCD colour transparency phenomena and assumes that $\sigma_d$ depends on $W$,$R$ and $Q^2$. The recent approach by Favart and Machado [42, 43] implements the dipole cross section from the saturation model [28, 44], which interpolates successfully between soft and hard regimes.

## 1.6 Previous DVCS measurements at HERA

The first measurement of the DVCS cross section was performed at HERA, by the ZUES [45] and H1 [46, 47] experiments, as a function of $Q^2$ and $W$, as shown in fig. 1.9.

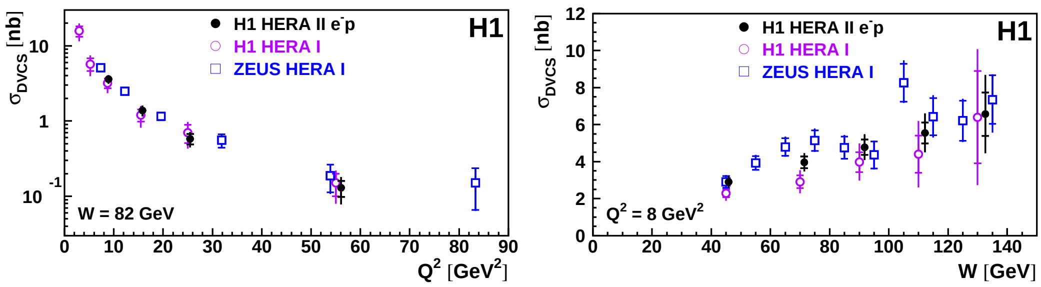


Figure 1.9: H1 and ZEUS measurements of the DVCS cross section as a function of $Q^2$ and $W$.

The cross section shows a steep rice in $W$, tipical of hard processes. The results of a fit $\sigma(W) \sim W^\delta$ were $\delta = 0.75 \pm 0.15\ (stat.)^{+0.08}_{-0.06}\ (sys.)$ for the ZEUS data and $\delta = 0.77 \pm 0.23\ (stat.) \pm 0.19\ (sys.)$ for the H1 measurement,which are compatible each other and with the value determined for the electroproduction of $J/\psi$ mesons [48].

The main uncertainty in the theoretical models comes from the slope value, $b$, for the $t$ dependence in the cross section, measured for the first time by the H1 collaboration [47] since the assumption that $t$ can be approximated by the negative square of the transverse momentum of the outgoing proton: $t \simeq |\vec{P}_{T_P}|$. Figure 1.10 shows the H1 measurement od the differential cross section as a function of $|t|$ quoted for different values of $< Q^2 >$ and $< W >$, whereas in fig. 1.11 it is shown the extracted $b$ slope value as a function of $Q^2$.

An important tool are also the asymmetries measurements [29, 35, 49],

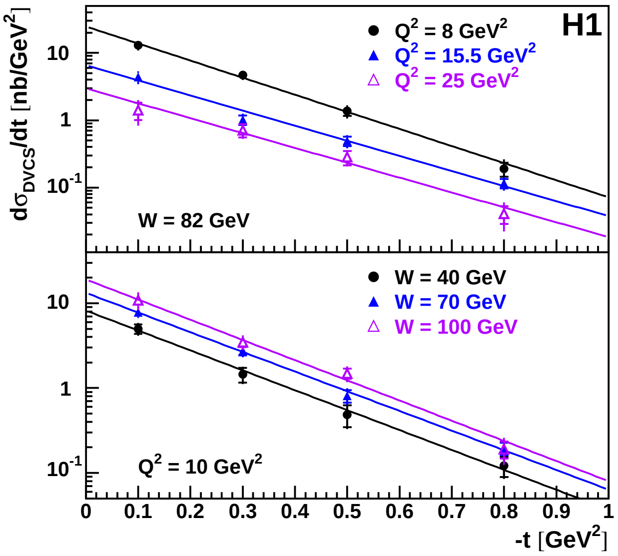


Figure 1.10: H1 measurements of the DVCS differential cross section as a function of $|t|$ for different values of the average $< Q^2 >$ and $< W >$.

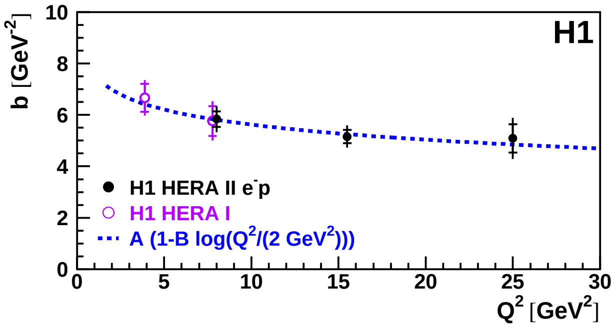


Figure 1.11: H1 measurements of the $b$ slope of the $t$ dependence, for the DVCS cross section, as a function of $Q^2$.

because they exploite the information contained in the interference term between DVCS and BH processes, providing a direct access to the GPD. DVCS asymmetries were measured by HERMES [50] collaboration at HERA and CLAS [51] collaboration at Jefferson Laboratory. Figure 1.12 (left) shows the HERMES measurement of the beam-spin asymmetry, $A_C$, as a function of the azimuthal angle $\phi$. Figure 1.13 (right) shows the HERMES measurement of the beam-charge asymmetry, $A_C$, as a function of $t$. Experimental results are compared with GPD models using either a factorized $t$ dependence including (dashed-dotted line) or not including (dotted line) the D-term contribution [22, 52], or a $t$ dependence introducing in the framework of the Regge theory with (dashed line) or without (solid line) the D-term contribution. Data seem to be better descripted by a Regge model.

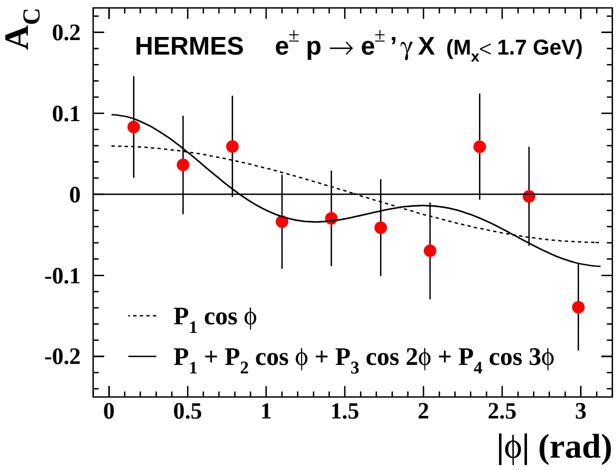


Figure 1.12: HERMES measurement for the hard electroproduction of photons off protons as a function of the azimuthal angle $\phi$, for the exclusive sample ($-1.5\ GeV < M_X < 1.7\ GeV$) before background correction. Statistical uncertainties are shown. The solid curve shows the result of a four-parameter fit: $(-0.011 \pm 0.019) + (0.060 \pm 0.027) \cos\phi + (0.016 \pm 0.026) \cos 2\phi + (0.034 \pm 0.027) \cos 3\phi$. The dashed line shows the pure $\cos\phi$ dependence.

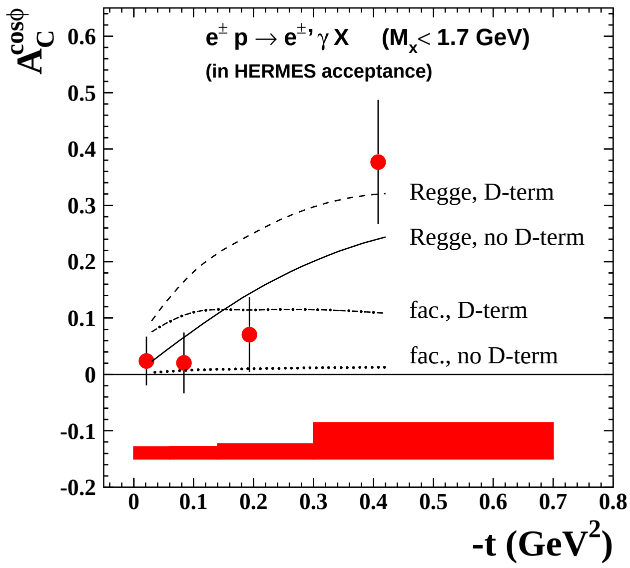


Figure 1.13: HERMES measurement of the beam charge asymmetry, $A_C$, as a function of $t$.

# Chapter 2

# The ZEUS detector

In this chapter an overview of the HERA collider and the ZEUS experiment is presented. The components of the ZEUS detector significant for this analysis are then briefly described.

## 2.1 The HERA collider

The HERA (Hadron Elektron Ring Anlage) [53], the first lepton-proton storage ring in the world, is located at the Deutsches Elektronen Synchrotron (DESY) laboratory in Hamburg in Germany (see fig. 2.1). The proposal for the ep collider was approved in April 1984. The first ep collisions were achieved in October 1991, and the ZEUS experiment took first physics runs in spring 1992. Since then physics data have been continuously collected at HERA till the end of operations in July 2007. HERA was designed to collide electrons or positrons, accelerated up to the energy of 30 $GeV$ but in 1999-2000 running period, used for this work, operated at 27.5 $GeV$, with protons with energies 920 $GeV$, yielding a centre-of-mass energy an order of magnitude higher than fixed target experiments($\sqrt{s} = 318\ GeV$).

The HERA tunnel is 6.3 $km$ long and it is placed 15 - 25 $m$ under ground level. It consists of four straight segments, each 360 $m$ long, joined by four arcs with a radius of 779 $m$. Leptons and protons are accelerated in two different pipes, equipped with conventional and superconducting magnets, respectively. The two beams consist of bunches of particles circulating in the rings in the opposite directions. Four experiments are located in the experimental halls at HERA. In the two of them, H1 (north hall) and ZEUS (south hall), the beams are collided at zero crossing angle. Two fixed-target experiments, HERMES (east hall) and HERA-B (west hall), make only use of the lepton and proton beams, respectively. H1 and ZEUS are devoted to mea-


Figure 2.1: Aerial view of DESY and the surrounding area in Hamburg. The location of the accelerators PETRA and HERA are indicated by dashed lines.

surements of the *ep* interactions. HERMES studies the spin structure of the nucleon by scattering longitudinally polarised leptons off polarised gas targets such as hydrogen, deuterium or helium, while the HERA-B experiment is devoted to explore $CP$-violation.

Fig. 2.2 shows a schematic layout of the HERA accelerator complex. The proton accelerator chain starts with a 50 $MeV$ LINAC. Before The proton accelerator injection into the DESY III synchrotron ring, electrons are stripped of the $H^-$-ions, yelding protons. After subsequent acceleration to 7.5 $GeV$ and 40 $GeV$ in DESY III and PETRA II, respectively, protons are injected into the HERA storage ring, where they are accelerated up to their final energy of 920 $GeV$. The procedure is repeated until HERA is filled with 210 proton bunches. The proton-beam life time is of the order of several days. The lepton pre-acceleration chain starts in LINAC II, where the lepton beam is accelerated up to 450 $MeV$. The lepton intensity accumulator is then filled with a single bunch of leptons of about 60 $mA$. This bunch is transferred to DESY II achieving energies of 7.5 $GeV$ and further into PETRA II until 70 bunches are accumulated, reaching energy of 14 $GeV$. They are transferred into the HERA lepton pipe until 210 bunches are filled and further accelerated to their final energies of 27.5 $GeV$.

The positron-beam life time for its final energy is about eight hours. In case of electrons, the life time for currents of about 20 $mA$ is reduced to about

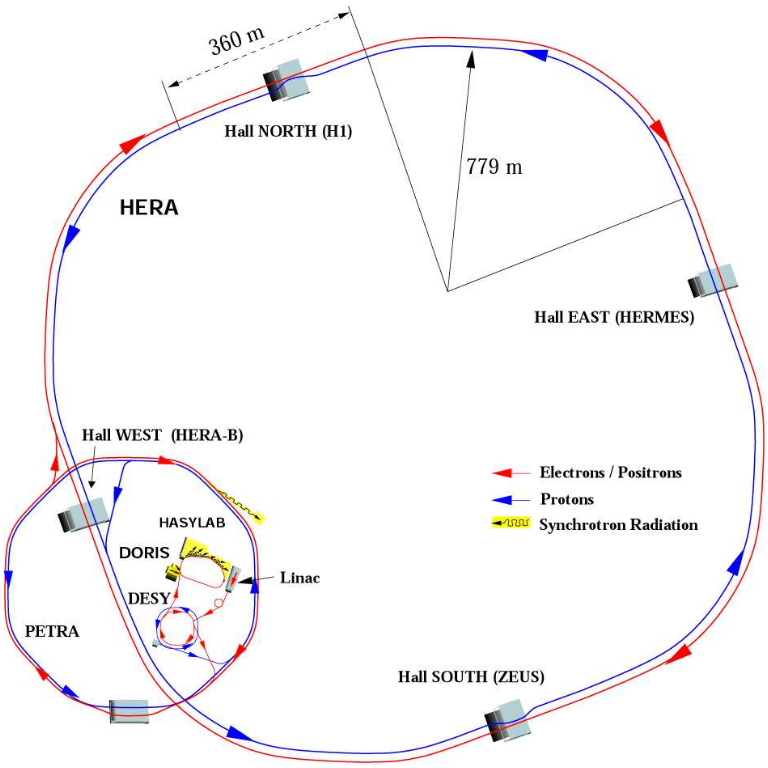


Figure 2.2: The HERA accelerator complex. Four experiments are located in the halls South (ZEUS), West (HERA-B), North (H1) and East (HERMES).

four hours. Life-time problem is attributed to capturing by positively charged dust, which originates from ion getter pumps of the HERA vacuum system. Leptons and protons are grouped in bunches of about $10^{10}$ particles each. In total 210 bunches of each leptons and protons spaced by 96 ns can be filled into HERA. The main bunches are followed by so called *satellite bunches* which are distanced by about 8 ns and 4.5 *ns* for the lepton and proton beams, respectively, with respect to primary bunch crossing time. During normal running, some of the 210 bunches are left empty (so called *pilot bunches*) in order to study the background conditions. Non-colliding bunches (when either the lepton or proton bunch is empty) enable the measurement of beam-gas related background, while empty pilot bunches (when neither of the two is filled) allow the study of cosmic-ray background rates.

Between the years 1992 and 2000 several changes at HERA have been performed, i.e. increase of the proton-beam energy and change of the lepton charge. In the first case the centre-of mass energy has been increased yielding a rise of the kinematic region. In the second case, one can profit from the different physics results only present in $e^-p$ or $e^+p$ collisions, yielding a possibility of comparing the two data sets. In 1993 the electron energy was increased from 26.7 $GeV$ to 27.5 $GeV$.

In 1994 due to the shorter life time of the electron beam, electrons were substituted by positrons. In the 1997-1998 winter shutdown the proton energy was increased from 820 $GeV$ to 920 $GeV$ with the consequent change of the centre-of-mass energy from $\sqrt{s} = 300\ GeV$ to $\sqrt{s} = 318\ GeV$. In the same period new ion getter pumps were installed, what gave a possibility to run with electrons again.

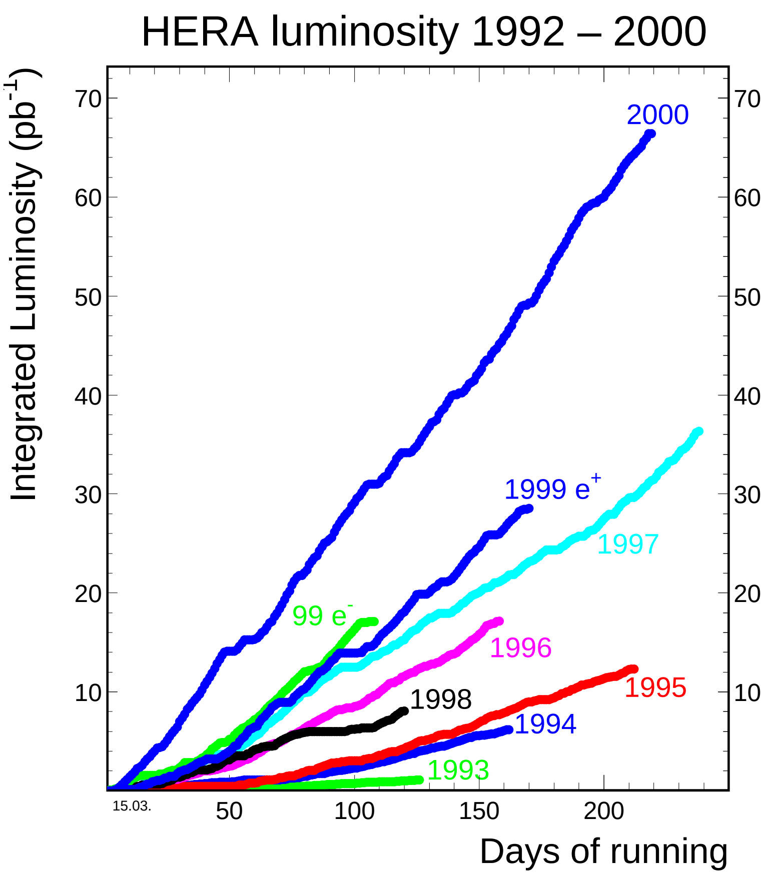


Figure 2.3: HERA delivered luminosity vs day of running for the 1992-2000 running periods.

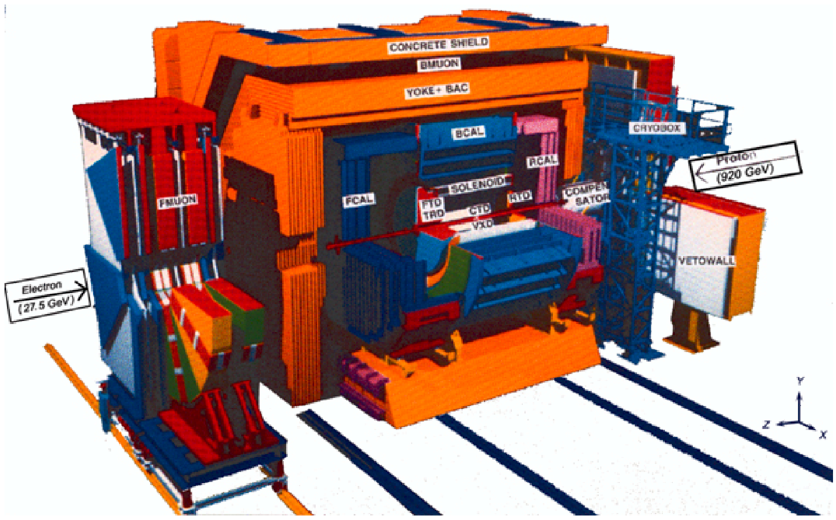


Figure 2.4: The Zeus Detector

## 2.2 The ZEUS detector

Figure 2.3 shows the luminosity delivered by HERA during the 1992-2000 running periods versus days of running.

ZEUS is a nearly hermetic multipurpose detector designed to explore photoproduction and deep inelastic NC and CC processes which occur in the *ep* scattering. The design takes into account the significant difference in the energies of the lepton and proton beams which results in a boost of the centre-of-mass energy in the proton direction. ZEUS was built in 1992 and ended its data taking activities in July 2007. It was operated by a collaboration of more than 500 physicists from 51 institutes in 12 different countries.

The ZEUS coordinate system is a right-handed Cartesian system, with the Z axis pointing in the proton-beam direction, referred to as the *forward direction*, the $Y$ axis pointing upwards and the $X$ axis pointing left towards the centre of HERA. The coordinate origin ($X = Y = Z = 0$) is at the nominal interaction point (IP).

Figures 2.5 and 2.6 depict cross sections of the ZEUS detector along and perpendicularly to the beam direction, respectively. A brief overview of the main components is given below followed by the more detailed description of the essential parts involved in this analysis. A more precise description of the components can be found in [54].

In the centre of ZEUS, the Central Tracking Detector (CTD) [55] surrounds the IP. In the forward and rear directions additional tracking information is provided by the Forward Tracking Detector (FTD), the Transition

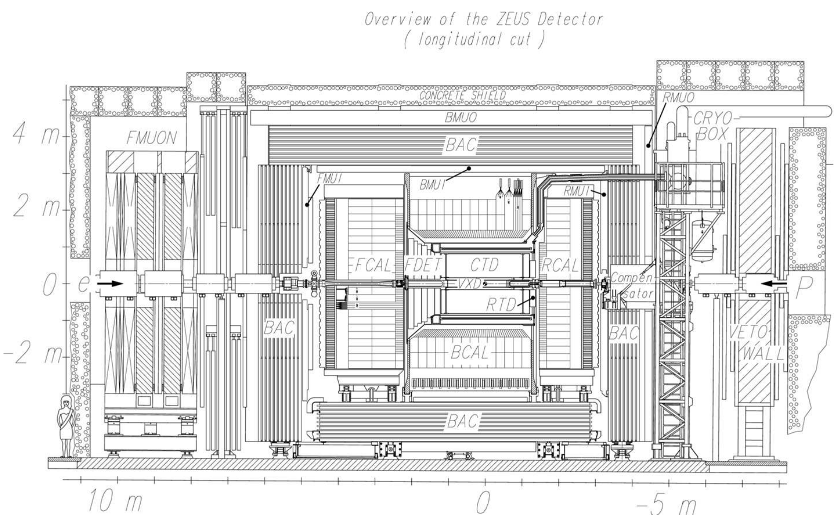


Figure 2.5: Longitudinal cut of the ZEUS detector.

Radiation Detectors (TRD) and the Rear Tracking Detector (RTD). The FTD and TRD together are referred to as the Forward Detector (FDET). Also, in the backward direction, the Small-angle Rear Tracking Detector (SRTD) [56] is mounted, which is a scintillator hodoscope and belongs to the tracking system. The whole tracking system is surrounded by a superconducting solenoid magnet, which provides a 1.43 $T$ magnetic field. This part of ZEUS is called the *inner detector*. The inner detector is surrounded by the uranium-scintillator calorimeter (CAL) [57], which is the main part of the ZEUS detector. It consists of three parts: the forward (FCAL), barrel (BCAL) and rear (RCAL) sections. In 1998 the Forward Plug Calorimeter (FPC) [58] was added into the beam-pipe hole of the FCAL, extending the polar-angle coverage (by one unit in pseudorapidity) in the forward direction. The presampler detectors [59] are attached to front face of all the calorimeter sections (FPRES/BPRES/RPRES). Each consists of a 5 $mm$ thick scintillator layer and is used to estimate the amount of energy loss in the inactive material in front of the CAL. In the RCAL and FCAL the Hadron-Electron Separator (HES) [60] consisting of a plane of 3 x 3 $cm^2$ silicon diodes is installed after three radiation lengths. The CAL is surrounded by an iron yoke which provides a return path for the magnetic field and serves as an absorber for the Backing Calorimeter (BAC) [61, 62],which measures energy leakage from the main calorimeter. Limited streamer tube chambers are located inside (FMUI/BMUI/RMUI) and outside (FMUO/BMUO/RMUO) of the yoke. Both muon chambers, inner and outer, and the yoke, which magnetic field is enhanced by additional copper coils to 1.6 $T$, provide a system

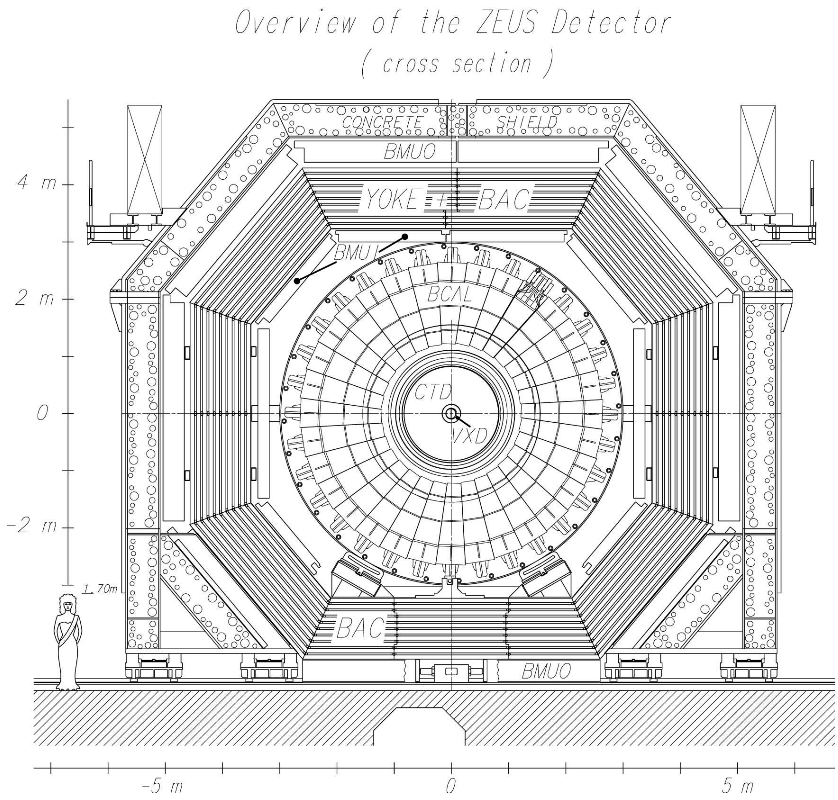


Figure 2.6: Cross section of the ZEUS detector.

for muon detection. In the backward direction, behind the RMUO, a veto wall detector is used to reject beam-related background. This set of subcomponents, together with the inner detector, is called the *central detector*.

Outside the central detector, in the forward direction, a lead-scintillator counter at $Z = 5.1\,m$, the Proton Remnant Tagger (PRT) [63], allows to obtain information on the hadronic final state. The Leading Proton Spectrometer (LPS) [64] was installed very close to the beam pipe untill 2000 year data taking at distances $Z = 24 - 90\,m$ from the IP. It consists of six silicon strip stations which detect protons scattered at small angles (transverse momentum $< 1$ $GeV$). The Forward Neutron Calorimeter (FNC) [65] is installed at $Z = 105.6\,m$ to detect very forward neutrons. It is a lead-scintillator sandwich calorimeter. In order to detect leptons scattered at very low angles, the Beam Pipe Calorimeter (BPC) [66] and the Beam Pipe Tracker (BPT) have been installed on two sides of the beam pipe in the rear direction. They measure the energy and position of leptons in the angular region $3.10 < \theta < 3.12\,rad$. Down the beam pipe, in the rear direction, two small lead-scintillator calorimeters (LUMIe, LUMI) [67], installed at $Z = -34\,m$

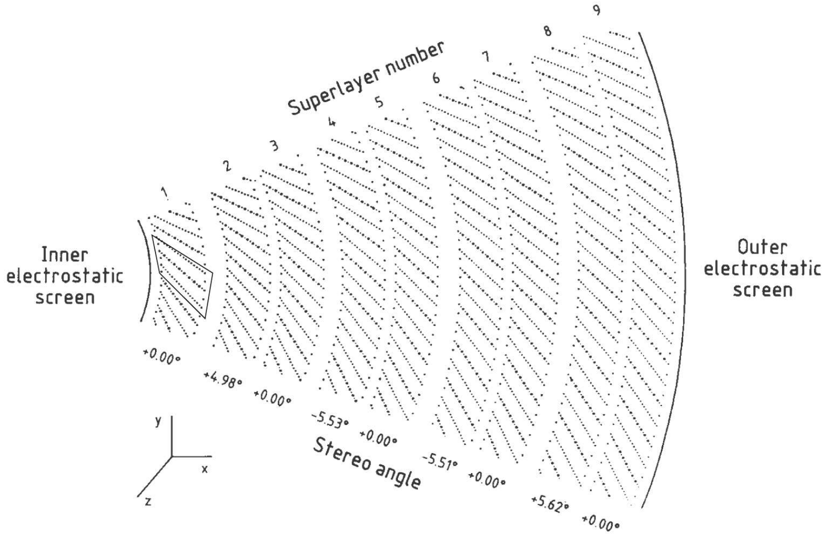


Figure 2.7: $X - Y$ cross section through one octant of the CTD. The large dots indicate the sense wires.

and $Z = -107\ m$, measure an outgoing lepton and photon, respectively, for determination of the luminosity and for tagging of low-$Q^2$ events with $0.2 < y < 0.6$ as well as radiative events. Moreover, the additional taggers have been installed at $Z = -8m$ and $Z = -44m$ to identify photoproduction events by detecting the scattered leptons.

### 2.2.1 The Central Tracking Detector (CTD)

The Central Tracking Detector (CTD) [55] is a cylindrical wire drift chamber. It is placed inside a superconducting solenoid, which produces a 1.43 $T$ magnetic field in the positive $Z$ direction. The CTD measures a momentum of charged particles and estimates the energy loss $dE/dx$ used for particle identification. The chamber has an overall length of 241 cm and an outer radius of 85 $cm$, covering the polar-angle region $15^\circ < \theta < 164^\circ$ equivalent to pseudorapidity range $2.02 > \eta > -1.96$. The CTD consists of 72 radial layers of sense wires, which are arranged into nine superlayers. A group of eight wires in the $r - \phi$ plane of each superlayer defines a cell. Altogether, the CTD contains 576 cells. One octant of the CTD is shown in fig. 2.7. The special setup of the wires allows very precise measurements of the X and Y coordinates. In order to measure the $Z$ coordinate the odd superlayers, which are axial layers, have wires parallel to the beam axis; while the even layers, which are stereo layers, are inclined about $\pm 5^\circ$ with respect to the beam axis.

The $Z$-position resolution of single tracks obtained from the stereo layers is 1.0 - 1.4 $mm$, yielding an improved vertex resolution of about 2 $mm$. The three inner axial layers incorporate a $Z$-by-timing system. This system allows the reconstruction of the $Z$ position by means of the time difference measured on both sides of the wire. Due to the poor resolution of this method, of about 4 $cm$, it is only used for trigger purposes. In the $r - \phi$ plane, the position resolution of CTD is $120 - 130\ \mu m$ for a single track and about 1 $mm$ for the event vertex. The CTD transverse-momentum resolution for full lenght tracks is $\sigma(p_T)/p_T = 0.0058 p_T \oplus 0.0065 \oplus 0.0014/p_T$ [68], with $p_T$ in $GeV$ and $\oplus$ denoting the addition in quadrature. The first term represents the intrinsic resolution of the CTD, while the second and third terms account for multiple scattering of charged particles inside and in front of the CTD, respectively.

In this analysis the CTD was used for reconstruction of an event vertex and the measurement of a track associated to the particle, i.e. its position reconstructed with the polar coordinates determined by the track. It was also used for measuring the momentum of the particle associated with the track, its charge, as well as the energy loss $dE/dx$ used for particle identification.

### 2.2.2 The Uranium Calorimeter (UCAL)

The Uranium Calorimeter (UCAL) [57] is the main ZEUS calorimeter. It is the most essential detector for reconstructing of the $ep$-scattering final state and plays a crucial rule in the analysis. The CAL is a sampling calorimeter consisting of alternating layers of 3.3 $mm$, that is about 1 $X_0$ ($X_0$ is the radiation length), of depleted uranium ($238U$) as an absorber and of 2.6 $mm$ of the organic scintillator as an active material serving for sampling the energy deposits.

The background coming from natural radioactivity of uranium is used for calibration of each UCAL channel, what is performed once a day. The thicknesses of both materials have been optimised to achieve a compensating calorimeter, which has the same response to electromagnetic and hadronic particles of equal energy. The energy resolution measured under test-beam conditions for leptons is

$$\sigma(E)/E = 18\%/\sqrt{E(GeV)} \oplus 1\%, \tag{2.1}$$

and for hadrons

$$\sigma(E)/E = 35\%/\sqrt{E(GeV)} \oplus 2\%. \tag{2.2}$$

The UCAL consists of three parts: forward (FCAL), with an polar-angle coverage of $2.5 < \theta < 39.9$ ($3.8 > \eta > 1.0$), barrel (BCAL) with $36.7 < \theta <$

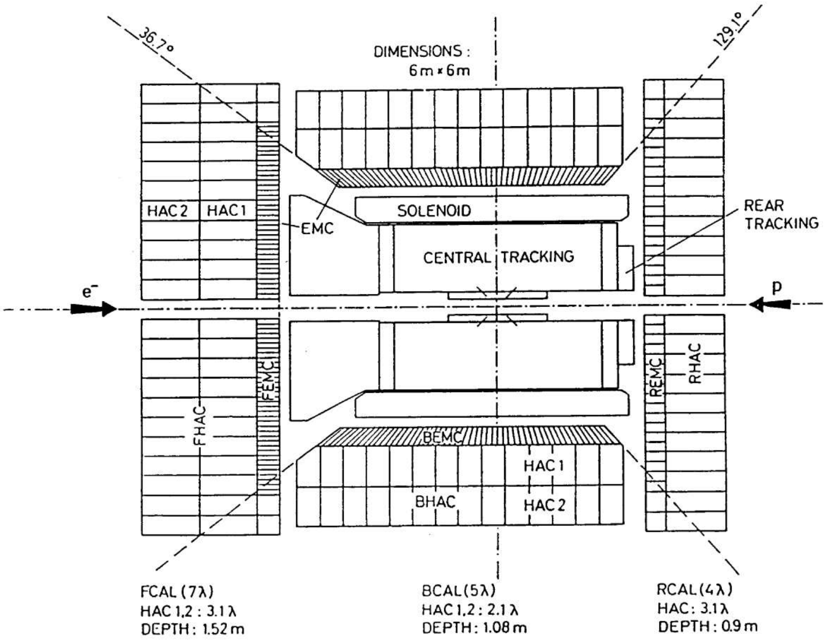


Figure 2.8: Schematic view of the ZEUS calorimeter. The three parts of the CAL are shown (FCAL/BCAL/RCAL) and their subdivision into EMC and HAC sections.$\lambda$ is theinteraction length.

129.1 ($1.1 > \eta > -0.7$) and rear (RCAL) witch covers the range $128.1 < \theta <$ 176.5 ($-0.7 > \eta > -3.5$), as shown in fig. 2.8.

The overall solid angle coverage of the UCAL is 99.8% in the forward direction and 99.5% in the backward direction. Each part of the UCAL is subdivided into electromagnetic (EMC) and hadronic (HAC) sections. The RCAL consists of one HAC part, while the BCAL and FCAL contain two HAC modules.

The UCAL also provides information on the position of incident particles. The position resolution depends on the detector granularity. The EMC and HAC sections constitute cells arranged into towers. Each tower is segmented longitudinally into one inner EMC and two (or one in the RCAL) outer hadronic sections (HAC1 and HAC2). Towers are grouped in modules. The size of cells varies depending on their position and destination in the UCAL. EMC cells have the typical size of 5 x 20 $cm^2$ in the FCAL and BCAL, and 5 x 10 $cm^2$ in the RCAL, while HAC cells have typically 20 x 20 $cm^2$ size.

Signals from each cell are read out on two opposite sides by a pair of photomultipliers (PMTs) coupled to the scintillator via wavelength shifters and optical fibres. The energy measurement is independent on the position of the particle within the cell since the signals from both PMTs are summed up. A comparison of the two signals provides information on the horizontal impact position of a particle.

Moreover, the CAL can give information on the time of incidence. The timing resolution of the CAL cells is better than 1 $ns$ for energy deposits greater than 4.5 $GeV$. It is mainly used by the trigger system to reduce background due to beam-gas events.

The CAL is an important component used in this analysis. It was used to detect the scattered lepton and the photon, to measure their energy and position outside the region in which the CTD could not be used. It played an important role in the reconstruction of the kinematic variables for low-$Q^2$ events.

### 2.2.3 The Small-angle Rear Tracking Detector (SRTD)

The Small-angle Rear Tracking Detector (SRTD) [56] is attached to the front face of the RCAL at $Z = -118\,cm$ (see fig. 2.9). It was installed to improve the measurement of the energy and angle of the scattered electron for low-$Q^2$ events.

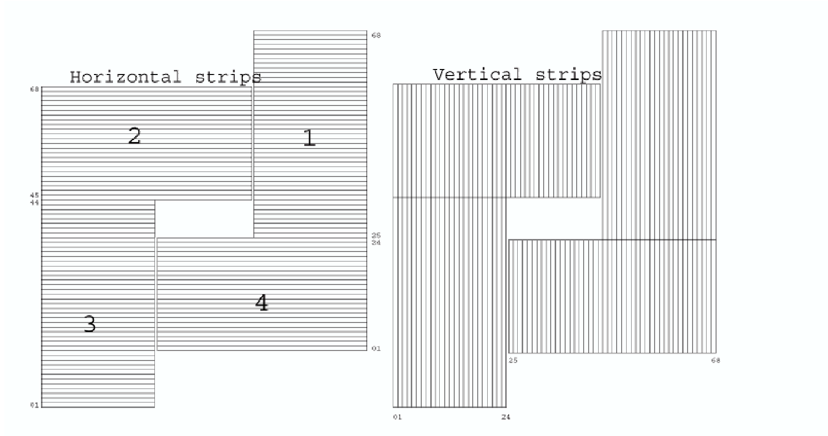


Figure 2.9: Orientation and numbering scheme of the strips of the two SRTD planes. The strip size is 0.98 x 24(44) $cm^2$. The asymmetric shape is due to the movement of the RCAL modules in 1995 in order to reduce the beam-hole size.

The SRTD consists of a horizontal and a vertical layer of 1 $cm$ wide and 0.5 $cm$ thick scintillator strips. Position and pulse height information is provided via optical fiber and PMTs. It covers a region 68 x 68 $cm^2$ in a transverse-position resolution of 3 $mm$.

Leptons, which lose energy through showering in the inactive material in front of the CAL, deposit more energy in the SRTD than non-showering leptons. Thus, the measured energy deposit in the SRTD can be used to correct for this energy loss. Moreover, the SRTD time resolution is better than 2 *ns* for a minimum-ionising particle (mip) and it is used to reject background events at the trigger level.

In this analysis, the SRTD was used to measure the position of photons and leptons scattered at small angles relative to the lepton-beam direction. Moreover, signals from this detector allowed for energy corrections due to particle showering in the inactive material in front of the CAL.

### 2.2.4 The Hadron-Electron Separator (HES)

The Hadron-Electron Separator (HES) [60] is placed in the RCAL (RHES) and FCAL (FHES). It consists of 3 x 3 $cm^2$ silicon diodes placed at a longitudinal depth of three radiation lengths, which corresponds to the approximate position of the maximum of the electromagnetic shower in the CAL. The separation between leptons and hadrons is based on the fact that the hadronic interaction length is 20 times larger than the electromagnetic radiation length. Therefore, hadrons produce smaller HES signals.

In this analysis, the fine segmentation of the RHES was used to improve the position resolution for both scattered leptons and photons.

### 2.2.5 The presampler

Presampler detectors (FPRES/RPRES) [59] are mounted in front of the FCAL and RCAL1. They consist of a layer of scintillator tiles: wavelength-shifting fibres, embedded in the scintillator, guide the scintillation light to PMTs. Particles, which shower in the inactive material in front of the presampler, lead to an increased particle multiplicity which is measured by the presampler. The combined information from the presampler and the CAL allows an event-by-event measurement of the energy loss in front of the CAL and, thus, allows to recover the calibration and energy resolution of the ZEUS calorimeter.

The segmentation of the presampler matches that of the HAC sections of the CAL, 20 x 20 $cm^2$. The segmentation of the EMC sections is shown, which is liner in the region not shielded from the nominal IP by the BCAL. The 20 x 20 $cm^2$ towers covered by the presampler tiles are shaded.

### 2.2.6 The Forward Plug Calorimeter (FPC)

The Forward Plug Calorimeter (FPC) [58] is a lead-scintillator sandwich calorimeter with readout via wavelength-shifter fibres. It was installed in 1998 in the 20 x 20 $cm^2$ beam hole of the FCAL and has a small hole of radius 3.15 cm in the centre to accommodate the beam pipe.

It extends the pseudorapidity coverage of the FCAL from $\eta < 4.0$ *to* $\eta < 5.0$. The FPC is devoted to detect particles coming from the dissociation of the proton in ep collisions.

The active part of the FPC has outer dimensions of 192 x 192 x 1080 $mm^3$. It is built up of 15 $mm$ thick lead plates alternated with scintillator layers of 2.6 $mm$ thick. The FPC is longitudinally subdivided into electromagnetic (EMC) and hadronic (HAC) sections which are read out separately.

The EMC section consists of 10 layers of lead and scintillator while the HAC part consists of 50 layers. The scintillator layers consist of tiles and form cells. The cell cross sections are 24 x 24 $mm^2$ in the EMC and 48 x 48 $mm^2$ in the HAC sections. There are 60 cells of the EMC and 16 of HAC part. Results obtained with a lead-scintillator calorimeter of similar composition show that the FPC is expected to be compensating ($e = h = 1$) [69]. The energy resolution for electrons was found to be $\sigma_E/E = 34\%/\sqrt{E} \oplus 7\%$ and for pions the energy resolution of combined signals from the FPC and the surrounding FCAL was determined to be $\sigma_E/E = 53\%/\sqrt{E} \oplus 11\% \oplus 3\% lnE$ [70]. The last term in the expression of the energy resolution for hadrons is due to the longitudinal leakage of energy.

The FPC in this analysis was used to remove low-mass proton-dissociative events.

### 2.2.7 The Leading Proton Spectrometer (LPS)

The Leading Proton Spectrometer (LPS) [71] (outlined in fig. 2.10) is performed to measure protons scattered at small angles ($\theta \leq 1\ mrad$)in the forward direction without a signal in the main detector. Using the HERA proton beam line magnetic dipoles and quadrupoles, the LPS detector allows an high precision measurement of the scattered proton momentum.

As shown in fig. 2.11, the LPS consists of 6 silicon microstrip stations S1 S6 positioned along the outgoing protons beam direction, at the distances of $z = 23.8\ m$, $z = 40.3\ m$, $z = 44.5\ m$, $z = 63.0\ m$, $z = 81.2\ m$, $z = 90\ m$, respectively.

The spectometer uses the well know technique of *Roman Pots* to bring the detectors close to the proton beam during the data taking periods. S4 S6 stations appoach from above and below the beam pipe whereas S1 S3

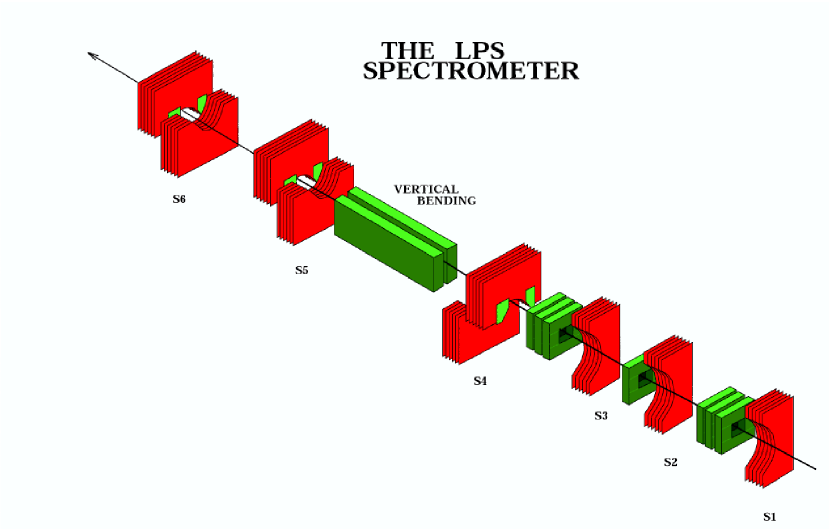


Figure 2.10: Schematic 3-dimensional view of the LPS spectrometer. The green elements are the proton beam line magnets, in red the 6 LPS stations are depicted.

station pots have horizontal movements. Each pot contains 6 layers of silicon microstips detectors and pairs of strips planes have three different orientations as a respect of vertical axis: $\pm 45°$ and $0°$. The silicon microstrips have a gauge of 115 $\mu m$ ($0°$ planes) or $115/\sqrt{2}\,\mu m$ ($\pm\,45°$ planes).

The stations shape is rectangular with an elliptic cut, along the side close to the beam pipe, which follows the $10\sigma$ beam profile in the zone where the station is placed so the detectors dimensions change station by station. The distance between two neighbor planes is around 7 $mm$ whereas the precision on which the planes are installed is of 30 $\mu m$. The resolution on the momentum measurement goes from 0.15% (for S4, S5, S6 stations and tracks carrying a momentum equal to the beam one) to around 2% (two stations in coincidence and lower track momentum). The $S4 \div S6$ stations include an additional microstrips plane used by the trigger sistem.

To reconstruct the scattered proton track the LPS uses information coming from those station it has crossed and in the case of more than a possible track is reconstructed the proton track is assumed to be that one with the best $\chi^2/ndof$ value.

The transport line for the proton beam, in the segment where the LPS is located, consists of four quadrupoles and nine dipoles (see fig. 2.11) which respectively focus the proton beam and determine the curvature of their trajectories.

Using its curvature in the magnetic field of the beam line is possible

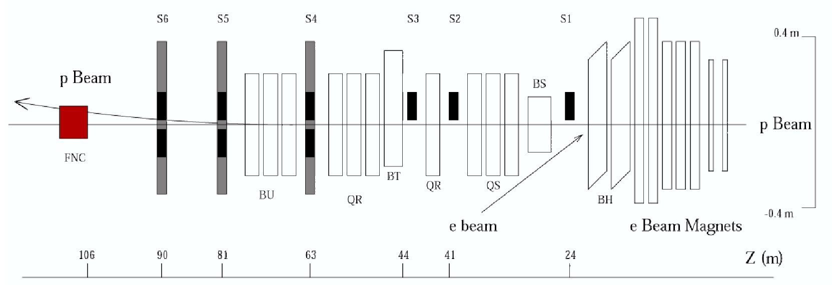


Figure 2.11: Layout of the LPS detector along the HERA tunnel. The represented magnets are horizontal curl dipoles (BH, BS e BT), vertical curl dipoles (BU) and quadrupoles(QS e QR).

to measure the momentum of the track. For the vertical bending dipoles, like those between S4 and S5 stations, the curvature ray $\rho$ of the tracks is correlated to their momentum by the relation

$$\frac{e}{p}B_X = -\frac{1}{\rho}. \tag{2.3}$$

In this case the particle moves on a circular trajectory on the plane $x = 0$.

The scattered proton track reconstruction process allows the calculation of the transverse momentum and it is based on the well known transport matrixes described in optics. From a track with a momentum $p$ and ZEUS vertex coordinates $(x_0, y_0)$ it is possible to calculate the $(x_a, y_a)$ coordinates of the struck point on the pot located at $z = z_a$ after the track passed trough a number of magnets

$$\begin{pmatrix} x_a \\ x'_a \end{pmatrix} = M \begin{pmatrix} x_0 \\ x'_0 \end{pmatrix} + \begin{pmatrix} d \\ \bar{d}' \end{pmatrix}, \tag{2.4}$$

where $M$ is the *transport matrix* which describes the effects of the magnetic dipoles and quadrupoles and is a function of $x_L$ while $d$ is a vector taking into account the curvature effects due to dipoles and quadrupoles. An analog relation is for $y$ coordinate.

Extracted $x_L = \frac{|\vec{p}|}{p_{beam}}$ the calculation of the momentum follows. The LPS detector measures the proton momentum with a resolution: $\frac{\Delta p_z}{p_z} = 0.4\%$.

### The LPS stations mechanics

The LPS stations are brought near the beam pipe during the data taking periods only when the beams are stable and the damage risk because of an high dose of radiations absorbed by the silicon microstips is low. The

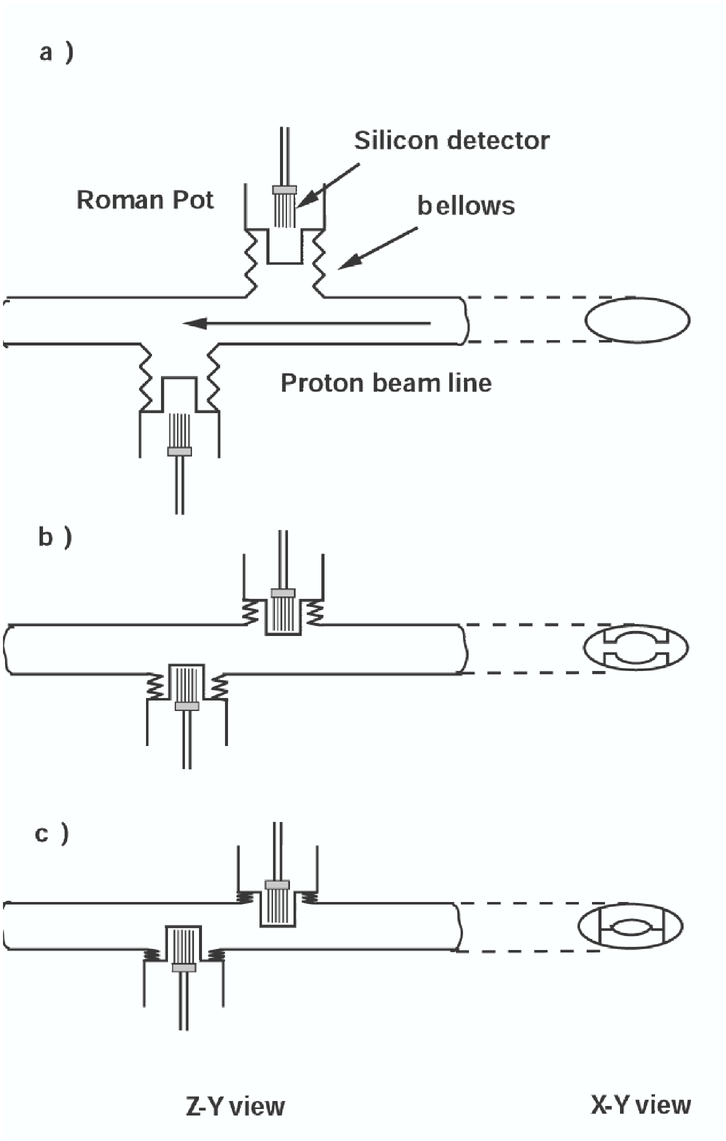


Figure 2.12: Positioning of the trackers in the stations $S4 \div S6$ within the vacuum tube. (a) the tracers are in the position of security. (b) the detectors are inserted into the pots and move to the beam. (c) the detectors are in the final position of data taking.

Roman Pots technique allows to push the detectors near to the proton beam maintaining the electronics of the stations in air without compromise the beam pipe vacuum.

The Roman Pots are 3 $mm$ thick inox steel cylinders in which there is a 380 $\mu m$ large windows corresponding to the detectors position. The pots are connected with the beam pipe by steel bellows which enable their movements. Inside the pots, detectors operate at the atmospheric pressure using a nitrogen flux to stabilise the air humidity.

Movements are controlled by step motors, with the exception of the stations S5 and S6 which use pots moved by DC motors. To compensate for the attraction of vacuum (up to 8 $kN$), the first four stations use a pair of steel springs fitted so as to obtain a constant tension, while for the stations S5 and S6 it is used a pneumatic nitrogen system.

The six planes of silicon detectors, containing the read-out electronics, are installed on a mechanically corrected support (*hand*), which allows the mounting of precision of each plan by means of calibrated thorns. The hand is in turn attached, by insulating support, to the mechanical *arm*, anchored to the sleigh of movement that allows rapprochement of the package of microstrips to the beam. The arm can move in the three directions, by micrometric screws, which allow a precise alignment of the detectors to the shaped base of the pots. The package of detectors is finally shielded with a Faraday's cage that also protects against dust and light in the tunnel.

The displacement of the stations in the vicinity of the beam is in three stages, see the fig. 2.12.

### The LPS front-end electronics

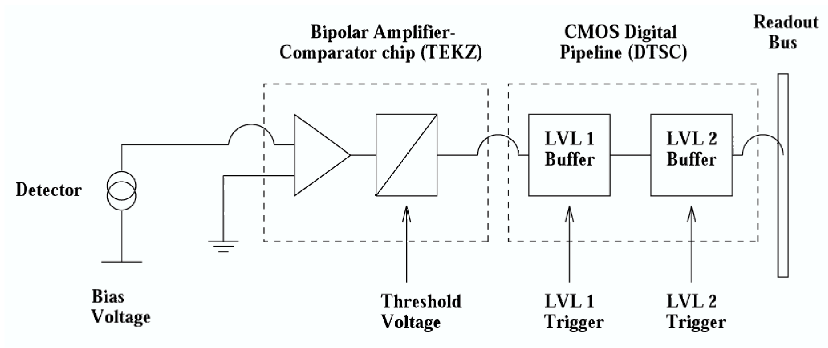


Figure 2.13: Scheme of the LPS binary reading system.

The LPS front-end electronics (a simplified scheme is shown in fig. 2.13), is designed according to very restrictive requests dictated by the HERA accelerator and by the read-out system of the signals and of the ZEUS trigger:

- resistance to radiation. The analog chip, since it is directly microwelded to the detector, works very close to the proton beam, and must be able to withstand to very high radiation doses;
- possibility of functioning at high frequencies. The Temporal distance between two colliding bunch is 96 $ns$, therefore, the Hera clock has a frequency of 10 $MHz$;
- high Density of read-out channels (each chip has 64 channels), due to the small step between the silicon strips ($115/\sqrt{2} \approx 80\,m$ for 45 plans);
- low consumption, to minimize the heat transfer to the detector and the consequent increase in detector temperature;
- low Noise of the analogue part;
- tolerance to the highest values of the current input. In fact electronics is directly coupled to the microstrips and the leakage current (up to some $\mu A$) increases with increasing radiation absorbed by detectors.

For the front-end electronics were selected two types of chip: an analog chips, for kits-discrimination of the signal (TEKZ [73]), followed by a digital one (CMOS digital time slice chip, DTSC [74]), microwelded directly to the first, for the sequencing of the signals of the individual strip and for the storage of data (*pipeline*) waiting for the signal coming from the first level trigger.

The TEKZ, built by Tektronix, consumes 2 $mW$ for Channel and the resistance to radiation is ensured through the use of small emitters *npn* (1.2 x 8 $\mu m$). Initially there is a low input impedance preamplifier, followed by a comparator with programmable threshold (the minimum is 1 $fC$, corresponding to a 0.25 *mip* particle), that converts into digital the output signal, and is separate from the preamplifier by a capacity of 10 $pF$ (High Pass filter for frequencies of more than 100 $kHz$).

The DTSC is treated in a specific way to have a strong resistance to radiation. It has 64 input channels and a serial port, and is controlled by four addressing lines and four data lines. A function of DTSC is also to store (in pipeline) events for a sufficient time at the arrival of the signal of the first (after 5 $\mu s$) and of the second level trigger. The data are stored in memory for 64 bunch crossing and the advancement of the data in the pipeline is governed by a clock signal in phase with the frequency of beams (10 $MHz$).

If the signal of the ZEUS first level trigger is present when the data occupy the $64^{th}$ slice are read, otherwise overwritten. If there comes a valid signal from the first level trigger, data are sent to the read-out electronics, where are then stored in a circular buffer pending the signal from the second level trigger, or can be sent to the second level memory already within the DTSC.

The TEKZ and DTSC detectors are mounted on a six levels plywood circuit, done in copper-INVAR, and having the same thermal properties of silicon. On the support are mounted small tubes of 1 $mm^2$ of diameter, used for the carriage of chips cooling water. Thermocouples on each of the plans allow to keep the temperature under control. It is observed that the cooling water system allows to reduce the temperature from values up to 45 ℃ to the values of approximately 24 ℃.

### The LPS read-out electronics

The read-out operations are guided by a 68030 processor using an $OS9$ operating system. The input signals, coming from the front-end electronics, are interfaced with the ZEUS acquisition system through dedicated VME crates:

1. read-out controller (Roc) [72], need to interface the Global First Level Trigger (GFLT), from which the HERA clock signal is coming, and end the LPS front-end electronics. It contains the memory images of first and second level contained in DTSC. The information, available on the bus VME output by the ROC, may be used for the control of any desynchronization of the system during the transfer of data. All of these signals are appropriately delayed within the ROC, to obtain a correct synchronization with the cycle of operation of the machine and with the passage of the tracks in the detector.

2. Read-Out MUltipleXer (ROMUX), one for each LPS pots. It is a modul located about 8 $m$ from the pot, in blocks of cement buried below the tunnel floor, in order to be shielded from radiation, being made with commercial components. The ROMUX was designed to reduce the length of the cables that connect electronics of front-end of each pots to the reading room at the distance of $\sim 100\,m$. It receives the signals and then sends them back to the SRC modules.

3. Serial Read-out Controller (SRC) [72], one for each pot. Its main task is to transfer data from the LPS front-end electronics to the ZEUS EVent Builder (EVB), using the VME bus. They also stocks data from DTSC while awaiting the GSLT decision.

### 2.2.8 The Luminosity Monitor

The event rate $R$ in a collider is proportional to the interaction cross section $\sigma$ and the factor of proportionality is called the luminosity $L$

$$R = L \cdot \sigma. \tag{2.5}$$

The value of the luminosity depends on the parameters of the beam of the collider and can be determined either from those or directly from the definition. The measurement of the time-integrated luminosity is essential in any extraction of cross sections in high energy physics experiments. In the ZEUS experiment, the luminosity is determined from Eq.2.5 measuring the rate of bremsstrahlung events produced by the Bethe-Heitler process $ep \to e\gamma p$ [75, 76]. The cross section for this particular process is precisely known from QED with an accuracy of 0.5%.

Moreover, it has a clean experimental signature, namely the coincidence of a photon and a lepton at small angles with respect to the lepton beam, with energies which add up to the initial-lepton energy. Although originally a coincidence measurement of the scattered lepton and the photon was planned, the rate of the photons alone was found to provide a precise measurement of the luminosity [77]. Since the bremsstrahlung photon and lepton emerge at very small angles, both particles propagate inside the proton beam pipe. At about 80 $m$ from the IP photons can leave the pipe because it is bent upwards. The exit window for the photons is installed at $Z = -92.5\,m$, while the position for the photon detector is at $Z = -107\,m$, as shown in fig. 2.14.

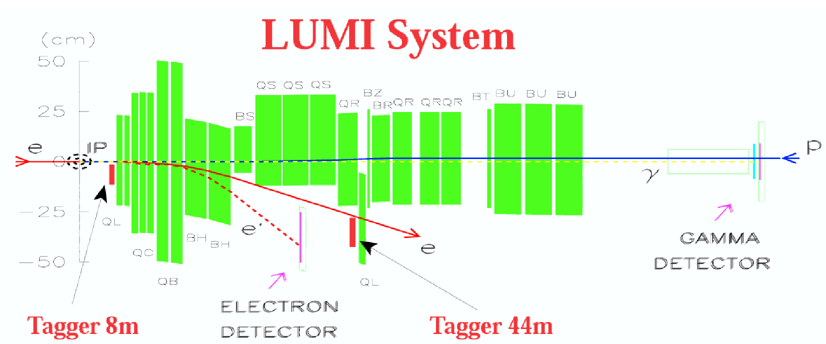


Figure 2.14: General layout of the ZEUS luminosity monitor.

The ZEUS luminosity is measured detecting energy of bremsstrahlung photons. The photons cross a copper-beryllium window with $0.095X_0$ thickness, then a 12.7 $m$ long vacuum pipe, which ends at an absorber that shields against the large flux of direct synchrotron radiation. It is made out of a $3.5X_0$ carbon block. The photons are registered by a lead-scintillator sampling calorimeter (LUMI$\gamma$) which also measures the shower position. The transverse dimensions of the LUMI$\gamma$ calorimeter are 18 x 18 $cm^2$ and its depth is $22X_0$. The energy resolution of the LUMI$\gamma$ detector was found to be $18\%/\sqrt{E(GeV)}$ in test beam measurements, but under the ZEUS experimental conditions it has degraded to only $23\%/\sqrt{E(GeV)}$. The measurement of the photon rate is corrected for a background coming from bremsstrahlung of leptons with residual gas. This is carried out by means of empty proton bunches as a reference. A detailed description of the luminosity monitor system (LUMI) can be found elsewhere [67].

### 2.2.9 The ZEUS trigger and data acquisition system

The high bunch-crossing frequency and large background rate pose difficulties for the readout and triggering. The ZEUS trigger system has three levels. Its task is to select interesting *ep* physics events among many background events. The total event rate at HERA is dominated by interactions of the proton beam with residual gas in the beam pipe. This background is of the order of 10 - 100 $kHz$, whereas the rate of *ep* physics events, after excluding a very low-$Q^2$ region, is only of the order of a few $Hz$. A schematic diagram of the ZEUS trigger and data acquisition chain is shown in fig.2.15. The first level trigger (FLT) has to reach a decision in 3 $\mu s$ and reduce the rate to less than 1 $kHz$. The FLT is a hardware trigger. It uses information from many detectors and requires a global decision based on trigger information derived from the separate detectors. The signal collection and transfer to the decision making system depends on the detector device. The data from every bunch crossing are stored in pipelines which are 46 bunch-crossing deep and allow for a 4.4 $\mu s$ latency per event.

Central for the ZEUS data acquisition system is the pipelining of the ZEUS calorimeter. If the trigger decision is positive the data must be recovered from the pipeline, because the data are overwritten as the pipeline is continuously recording new data. The trigger information from the components of the ZEUS detector are sent to the global first level trigger (GFLT) between 1.0 and 2.5 $\mu s$ after the crossing occurred. The GFLT is issued exactly after 46 bunch crossings. If the GFLT decides to keep the event the data are passed on to the next trigger level.

The second level trigger (SLT) is software-based and it is designed to reduce the trigger rate below 100 Hz. Typically, the SLT decision takes 30 $\mu s$ introducing about 2% dead time. At this level a transputer network calculates objects like track momenta, the event vertex or calorimeter clusters which

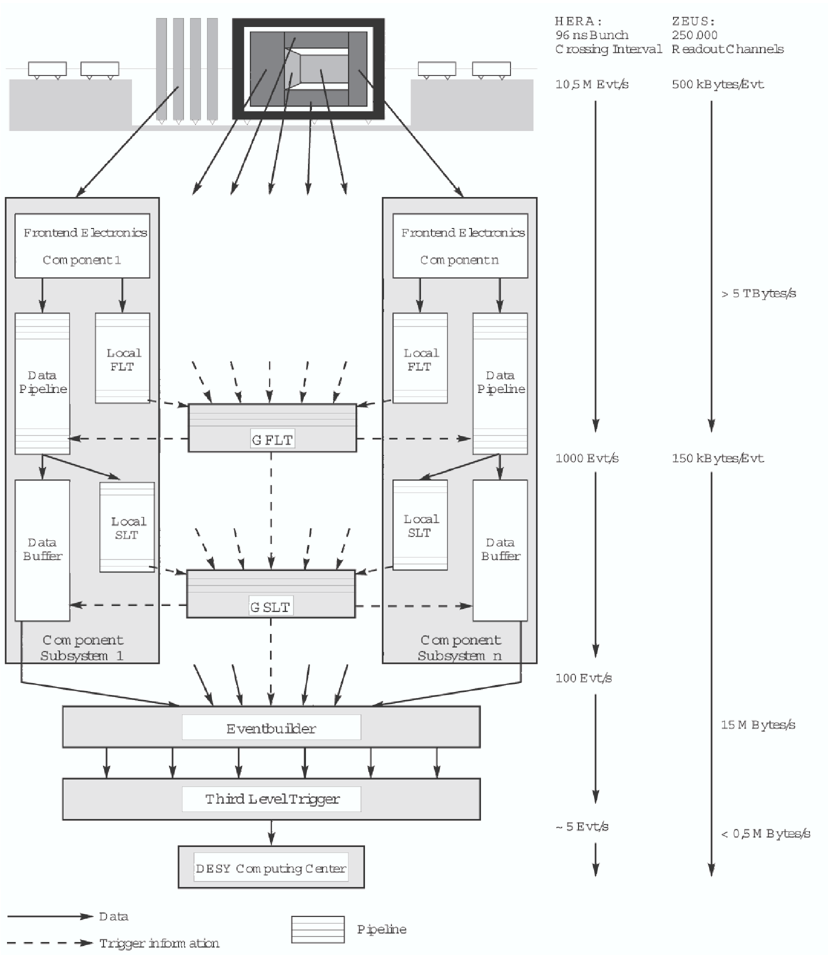


Figure 2.15: The ZEUS trigger and data acquisition system.

allow a more restrictive trigger decision. As in the case of the FLT, each component has its own local SLT process, passing information to the global second level trigger (GSLT) which then takes the decision to accept or reject the event. If the GSLT decision is positive, all components send the data to the Event Builder, which combines the information for the event, writes it into the final data format (ADAMO) and makes it accessible to the next trigger level.

The third trigger level (TLT) performs part of the offline analysis on a farm of Silicon Graphics (SGI) CPUs. At this level, detailed tracking as well as jet and electron finding are performed. The TLT accepts events at a rate below 10 $Hz$. The events have a typical data size of about 100 $kB$ in the ADAMO format. They are written to disks at the DESY computing centre via a fibre-link (FLINK) connection. Here they are available for offline reconstruction and analysis.

# Chapter 3

# Monte Carlo simulation

An accurate simulation of physics processes and detector response is crucial in every data analysis. Using a Monte Carlo simulation is possible to evaluate the resolution of physics variables, the acceptance of the detector and the trigger efficiency. An accurate MC simulation is also important in physics analyses to design selection criteria and possible background sources and their rimotion. Moreover, the MC program is indispensable to test physics models by comparing distributions, generated according to the model to be tested, with real data. An other task of MC simulations is also to check systematic uncertainties in a measurement by adjusting the input distributions to the detector simulation.

In this chapter, the steps of the MC simulation in the ZEUS experiment are presented. Several MC generators used for the cross-section calculation and background studies in this analysis are described.

## 3.1 The ZEUS detector simulation

The simulation of physics events in ZEUS is performed in two steps. In the first step, the *ep* scattering process is simulated by means of a MC generator. It provides the four-momenta of all the particles involved in the interaction: incoming, intermediate and final-state particles, as well as their types and the production vertices. In the second step, a simulation of the detector response to the outgoing particles and trigger are simulated. MOZART [78] (MOnte carlo for Zeus Analysis, Reconstruction and Trigger) is a program which performs the full simulation of the ZEUS detector. It is based on the GEANT3 [79] package, which takes into account the geometry and materials of all detector components, as well as the magnetic field in the CTD. It incorporates the present understanding of the detector accumulated from test-beam results and current physics analyses. The three level trigger decision, which is based on the detector signals, is simulated with the ZGANA [80] package (Zeus Geant ANAlysis). The simulated detector responses of all its components are stored in the same ADAMO tables as the physics data and thus they can be processed by means of the same event reconstruction program ZEPHYR and offline analysis code.

## 3.2 Monte Carlo generators

In order to extract the DVCS cross section from the collected event sample, several MC programs were used. The GenDVCS program was used to generate MC samples for the DVCS process in order to extract the DVCS signal, to study the resolution of measured quantities and to calculate cross sections. Moreover, in order to distinguish between the DVCS signal and background processes, which can have the same signature in the detector, the GRAPE-Compton, the GRAPE-Dilepton and the ZEUSVM programs were also used.

### 3.2.1 GenDVCS

The MC generator dedicated to the DVCS events simulation is GenDVCS [81]. It is based on the FFS model (see Sec. 1.4) and reproduces the elastic DVCS process only. The basic steps of the generation procedure are:

- the four-momenta of the scattered electron and of the photon are generated according to the FFS $\gamma^* p \to \gamma p$ cross section of the form (1.37).

  The parameterisation ALLM97 [82] of the $F_2$ structure function of the proton was used as input. In this empirical fit to the $\gamma^* p$ total cross-section data, the $Q^2$ dependence of $\rho$ was parametrised as $\rho = \frac{\pi}{2}(0.176 + 0.033 \ln Q^2)$ [81].

- The four-momentum of the scattered proton is generated according to the exponential function

$$\frac{d\sigma^{ep}_{DVCS}}{dt} \propto \exp(-b|t|).$$

  In GenDVCS $b$ was assumed to be constant and was set to $4.5 GeV^{-2}$ over the whole phase space [33]. While this dependence is important for the normalisation of the calculated DVCS cross section, it does not affect the acceptance corrections.

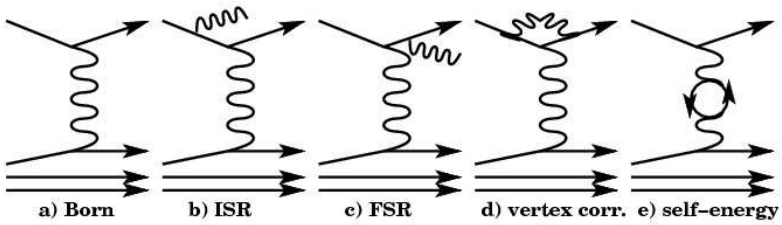


Figure 3.1: Diagram showing the LO QED corrections to the Born level: born level (a); a photon emitted from the initial (b) and final (c) lepton line and the vertex (d) and self-energy (e) corrections.

- the generated distribution of the azimuthal angle between the electron and proton scattering planes in the $\gamma^* p$ centre-of-mass system is flat.

Higher order contributions to the Born level cross section of Eq. 1.37 have to be taken into account as they can result in corrections to the observed variables. These corrections originate from the emission of additional real or virtual photon from the electron line. The QED corrections to the Born level process are shown in fig. 3.1. In the propagator correction also called the self-energy or vacuum polarisation correction (fig. 3.1e), all charged fermions with $m^2 \leq Q^2$ have to be considered. Radiative corrections coming from the proton line are much smaller than the leptonic ones and were neglected.

These QED contributions can not only change the observed cross section but also introduce new types of events, since additional photons can emerge. The radiated photons affect the relation between the kinematics of the $\gamma^* p$ interaction and the measured quantities such as the electron angle and its energy. The size of the effect on the $Q^2$, $W$ and $x$ reconstruction depends on the reconstruction method. Thus, it is important that these contributions are accounted for in the MC generator. For proper treatment of radiative effects, the GenDVCS generator was interfaced to the HERACLES [83] generator, which includes corrections for initial- and final-state photon emission from the electron line, as well as vertex and propagator corrections.

### 3.2.2 GRAPE-Compton

The elastic and inelastic BH processes, $ep \to e\gamma p$ and $ep \to e\gamma X$, were simulated using the GRAPE-Compton [84] generator.

For the elastic cross-section calculation, the electric and magnetic proton form factors $G_E$ and $G_M$, respectively, are used in GRAPE-Compton. $G_E$ is calculated according to the formula of the dipole fit

$$G_E = (1 + \frac{|t|}{0.71GeV^2})^{-2}, \tag{3.1}$$

and $G_M$ is calculated from the relation

$$G_M = \mu_p G_E, \tag{3.2}$$

where $\mu_p$ is the Bohr magneton.

The electromagnetic proton structure functions are parametrised following [85] for $M_X < 2\ GeV$ (the proton resonance region) and using ALLM97 for $M_X > 2\ GeV$. These two parameterisations are based on fits to the experimental data of the total $\gamma p$ cross sections.

The GRAPE calculation of the proton vertex covers the whole kinematic region divided into three categories of elastic ($M_X = m_p$), quasi-elastic ($|t| < 1\ GeV^2$ or $m_p + m_{\pi^0} < M_X < 5\ GeV$) and DIS ($|t| > 1\ GeV^2$ and $M_X > 5\ GeV$) processes. Moreover, the ISR and FSR corrections could be included. When the ISR process is turned on, the correction for the photon self energy (the vacuum polarisation) is included according to the parameterisation in [86] by modifying the photon propagator. The FSR corrections are performed by PYTHIA [87] using the parton-shower method. The hadronic final state is generated using the MC event generator SOPHIA [88].

### 3.2.3 GRAPE-Dilepton

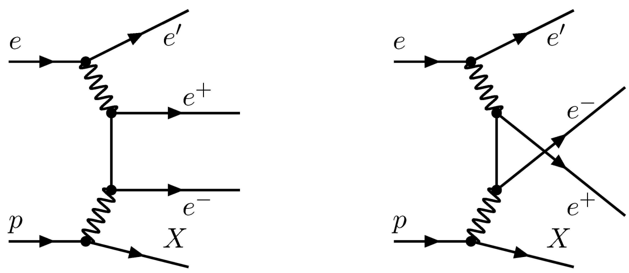


Figure 3.2: Diagrams for dilepton production processes. $X$ denotes either the intact proton or its dissociative state

In the study of the DVCS process a precise estimation of the dilepton-production background, $ep \to e'e^+e^-X$ (see fig. 3.2), is important since it forms a background contributing to the BH sample discussed in Sec. 5.3.1. This process was studied by means of the GRAPE-Dilepton [84] generator. In this program a calculation of the cross section is based on Feynman diagrams with virtual $\gamma\gamma$, $\gamma Z^0$, $Z^0Z^0$ collisions and a photon conversion into a lepton pair. For the purposes of this analysis only the process of the photon-photon collision, corresponding to the diagrams of fig. 3.2 was taken into account. This $\gamma^*\gamma^*$ process was found to be dominant in most of the phase space.

The cross-section calculation in GRAPE-Dilepton follows the details for GRAPE-Compton described in Sec. 3.2.2.

### 3.2.4 ZEUSVM

The ZEUSVM [89] program is the generator used to simulate the elastic vector-meson production process $ep \to eVp$. ZEUSVM generates kinematic distributions according to basic phenomenological functional relations with a minimum number of free parameters. The $Q^2$ and $W$ distributions are generated according to the parameterisation of the total $\gamma^* p \to Vp$ cross section

$$\sigma_{tot}^{\gamma^* p \to Vp}(Q^2, W) \propto \frac{W^\delta}{(M_V^2 + Q^2)^n}, \tag{3.3}$$

where $\delta$ and $n$ are parameters and $M_V$ is the vector-meson mass. The four-momentum of the outgoing proton is generated according to the exponential function

$$\frac{\sigma_{tot}^{ep \to e'Vp'}}{dt} \propto exp(-b|t|). \tag{3.4}$$

In the generation procedure the parameters $\delta$, $n$ and $b$ were taken from the fit of the resulting cross section of the diffractive production of vector mesons to data. The distributions of the helicity angles were generated flat. Then for proper acceptance corrections the helicity angle distributions were reweighted in a way to preserve s-channel helicity conservation. Moreover, the ZEUSVM program was interfaced to packages for QED radiative corrections based on HERACLES.

The ZEUSVM program was used to simulate the background contributing to the BH sample from diffractive $J/\psi$ electroproduction, see Sec. 5.3.1.

# Chapter 4

# Event reconstruction

The most significant information, needed for the proper calculation of cross sections in the present analysis comes from track and vertex informations provided by the CTD and from the reconstruction of the energy and position by the CAL, the SRTD, the HES and the presampler.

In this Chapter, the procedure for identification and reconstruction of particle energy and position is described and also the calculation methods for kinematic variables are introduced.

## 4.1 Track and vertex reconstruction

A precise determination of the vertex and the track momentum is important in order to get an unbiased measurement of kinematic variables.

The track reconstruction is based on the package VCTRACK [90]. This package reconstructs tracks and finds the primary and secondary vertices. The track reconstruction procedure runs trough two steps: during the pattern recognition measured hits are assigned to track candidates, then hits belonging to the same track candidate are fitted to obtain the trajectory of the track.

Reconstructed tracks that are compatible with the beamline are fitted until a vertex position is found. The fitted trajectories are extrapolated to the beam line and the result of extrapolation of all the tracks is averaged to obtain the primary vertex. Then tracks are refitted including the found vertex to determine their trajectories. Tracks that do not fit the primary vertex are used to found *secondary vertices*. In this analysis only primary tracks with a $\chi^2/ndof < 10$ are accepted.

An accuracy of $2\,mm$ is achieved for the reconstruction of the vertex coordinate $Z_{vtx}$ while the accuracy for the $X_{vtx}$ and ($Y_{vtx}$) vertex position

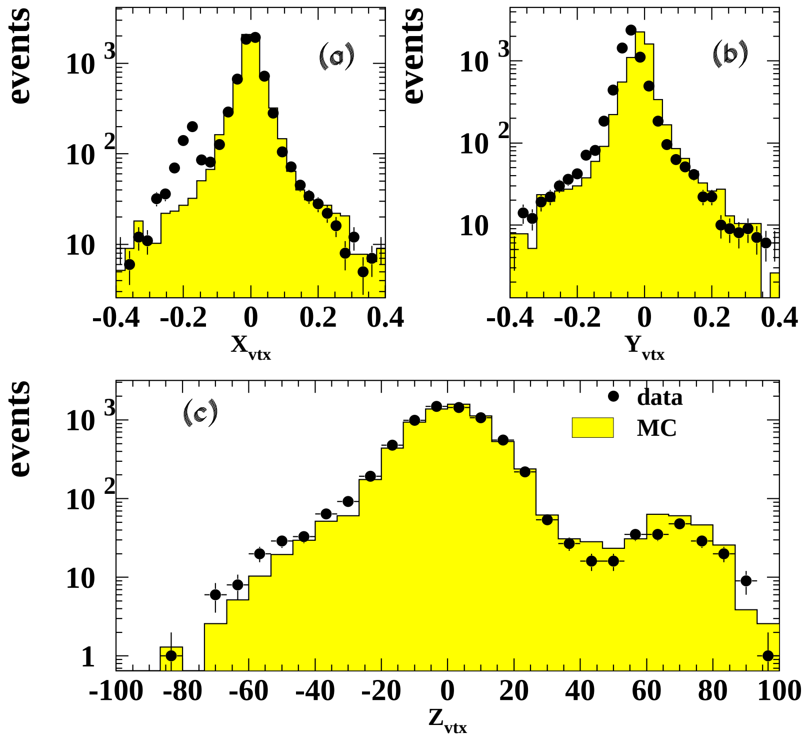


Figure 4.1: Distribution of vertex $X$, $Y$ and $Z$ coordinates for ZEUS 1999/2000 $e^+$ data (dots) compared with MC simulation (solid).

reconstructions is about 1 $mm$. The distributions of the $X_{vtx}$, $Y_{vtx}$ and $Z_{vtx}$ coordinates of the vertex are shown in fig. 4.1 and compared with the MC simulation.

The $X_{vtx}$ distribution shows a secondary peak at $Xvtx = -0.2\ mm$ not reproduced by MC. The nature of this peak was investigated in this work. In fig 4.2 it is plotted the $X_{vtx}$ variable as a function of the ZEUS run number. One can observe that runs with a systematically shifted $X_{vtx}$ value are in the run period $33300 - 33720$ which is part of the $99e^+$ data taking.

The $Y_{vtx}$ distribution presents an MC simulation little shifted with respect to the data distribution of about 0.5 $mm$ due to a sistematic $Y_{vtx}$ shift during the whole 2000 data taking period.

During those periods of data taking the nominal $X_{vtx}$ and $Y_{vtx}$ positions was choosen different from (0,0).

The $Z_{vtx}$ distribution has a central peak at $Z_{vtx} \approx 0\ cm$. The length of the proton bunch is bigger than the length of the electron one, so electrons

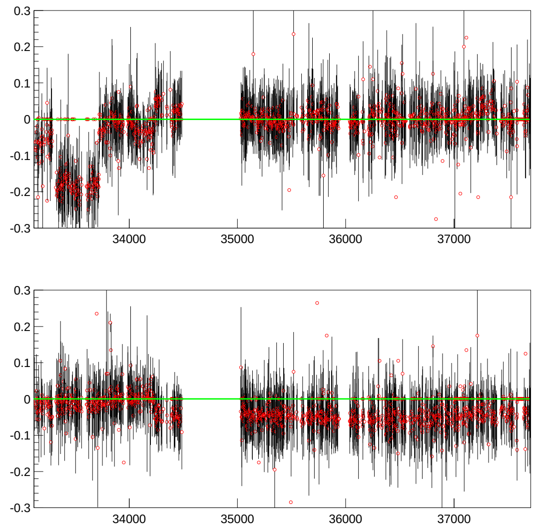


Figure 4.2: $X_{vtx}$ and $Y_{vtx}$ values (red circles) for each run contained in the $1999-2000e^+$ data taking period as a function of the ZEUS run number. The black bars associated to each circle represents the corresponding run width.

can collide with protons over an extended longitudinal $Z$ range. The spread of the central peak of the $Z_{vtx}$ coordinate reflects this fact. The bump visible at $Z_{vtx} = +70\,cm$ comes from events where electrons collide with protons in forward *satellite bunches*.

## 4.2 Calorimeter reconstruction

The reconstruction of signals coming from the CAL is performed by the CCRECON [91] package. The first step of the event reconstruction is the correct determination of the energy deposited in cells, next is the reconstruction of position, energy and direction of particle showers, the search for jets by clustering the cells and finally the identification of the reconstructed objects.

Deposits in the calorimeter originating from natural radioactivity of the uranium, bad operation of the PMTs and problems with read-out electronics are classified as noisy cells. They are rejected using different criteria

- **Standard noise suppression cut:** cells in electromagnetic part of the caloremeter with an energy $E_{cell}^{EMC} < 60\,MeV$ and in the hadronic section with $E_{cell}^{HAC} < 100\,MeV$ are rejected. If the cells are isolated the previous threshold are 80 $MeV$ and 140 $MeV$ respectively.

- **Imbalance cut:** $|E_{left} - E_{right}|/E_{cell} > 0.7$ where $E_{left}$ and $E_{right}$ are the signals coming from the two PMTs of the cell. This cut is only applied at cells with $E_{cell} < 1\,GeV$.

- **Noisy cell list:** this list contains cells identified as noisy after quality monitoring checks in different time periods of data taking.

After noise soppression the local clustering starts. In this geometrical clustering cells are grouped according to their physical adjacency. Output objects are called *condensates* and serve as the starting point for the reconstruction of single particle showers. Found condensates are tentatively identified using the different showering properties of various particles and the segmentation of the CAL.

### 4.2.1 Energy and position reconstruction using SRTD

For particles which hit the RCAL close to the beam hole the position measurement is improved using the SRTD (see Sec. 2.2.3). This detector allows to obtain the electron impact position with a resolution of $\sigma_{X,Y}^{SRTD} \sim 3.5\,mm$ [92] due to fine granularity of $1\,cm$ wide strips of this device.

The clustering procedure in the SRTD is based on the assumption that all strips with less than two empty strips between them belong to one cluster. Empty strips are defined as strips with deposits below the noise threshold. Following this assumption one has to notice that, due to dead channels in the SRTD, a $2cm$ wide gap can be created in the distribution of the reconstructed position with a rather severe impact on the clustering algorithm. To reduce this effect, the energy of strips from the dead channel list is taken as the average energy of the two neighbouring strips.

If at most one particle hits a SRTD quadrant, the reconstruction of the $X$ and $Y$ position is unique. If more than one particle hits a quadrant, the clustering algorithm yields several $X$ and $Y$ coordinates. Matching two or more SRTD hits gives long tails in the resolution. Therefore, to solve this problem, the SRTD cluster is considered only if it is within $4\,cm$ of either the CAL or the RHES cluster position.

The SRTD signals are calibrated on the signal of a minimum-ionising particle (mip) which is defined as the average response of the detector to a single particle traversing the SRTD perpendicularly. The reconstructed energy is the sum of deposits in all strips belonging to the cluster in both

SRTD planes. Thus, the energy deposit $E_{SRTD}$ corresponding to the hit is half of this energy.

The calculation of the shower position is performed in the same way for $X$ and $Y$ coordinates. First of all, the shower maximum has to be found. It is defined as the strip of $x$ coordinate for which an opportunely weighted 3-strips sum is maximal. A weighted sum is used instead of the simple energy of one strip since it is less sensitive to shower development and fluctuations of the number of photoelectrons in a PMT. Then the centre of gravity is calculated using only three central strips of the shower maximum. Further a correction to this position is applied to compensate for the bias of this algorithm towards the central strip [93].

The SRTD can also be used to correct the calorimeter energy deposits for the particle energy loss in the inactive material in the RCAL beam-pipe region. For electrons traversing through a large amount of dead material before reaching the SRTD, the energy deposits in the SRTD due to the developed showers are large.

### 4.2.2 Energy and position reconstruction using HES

The HES (see Sec. 2.2.4) can be used to reconstruct the position of a particle hitting the RCAL. Due to the small size of a diode of 3 x 3 $cm^2$ this can be done with the position resolution for electrons of $\sigma_{X,Y}^{HES} \sim 5\ mm$ [94], which for $X$ is almost a factor of two better than of the CAL, while for $Y$ it is only slightly better in the HES. There is a significant difference between hadron and electron deposits in the HES. Hadrons usually produce an energy deposit in one diode only, so the position resolution for them is rather poor. For electrons a much better position resolution can be achieved, as the HES is situated near the shower maximum, where more than one diode shows a signal.

### 4.2.3 Energy reconstruction using presampler

The dead material situated between the $ep$ interaction point and the front face of the CAL leads to a degradation of the energy measurement of particles.

Particles which initiate showers in the dead material in front of the RCAL lead to an increased particle multiplicity which is measured by the RPRES. The combined information from the RPRES and the RCAL allows an event-by-event measurement of the energy loss in front of the RCAL and thus allows to recover energy resolution of the ZEUS calorimeter [95].

In the clustering algorithm, the CAL position of the particle hit is projected onto the RPRES surface. The 20 x 20 $cm^2$ tile which is a result of this projection is called the central tile. The cluster is then built up and consists of the central tile with either 8 or 24 surrounding tiles. The total energy collected in the RPRES, $E_{RPRES}$, is the sum of energies of all tiles belonging to the cluster.

### 4.2.4 Corrections for energy and position

The energy loss due to showering in the dead material in front of the RCAL is estimated using the energy deposited in the SRTD and the RPRES. The idea of the energy correction method is that the energy loss is related to the number of interactions in that material, thus, to the multiplicity of the resulting shower particles. The energy measured in the RCAL was corrected using the relation proposed in [95]

$$E_{corr} = E_{CAL} + C \cdot x, \tag{4.1}$$

where $x = E_{RPRES}$ or $x = E_{SRTD}$. The coefficient $C$ is evaluated using the kinematic peak events for which the distribution of the electron energy is sharply peaked near the electron-beam energy (27.5 $GeV$).

The energy of charged particle reaching the BCAL was corrected for the interaction with dead meterial using the track measurement from the CTD [96]. When a charged particle hits the BCAL, two independent measurements of energy (the momentum of the track and the calorimeter energy) are available. The advantage is that when the momentum of the track is measured, the charged particle has not travelled through as much inactive material as when it reaches the BCAL, so the CTD measurement is closer to the true energy of the particle. In the BCAL the total momentum of the track was taken as the *true* energy of the charged particle. For photons hitting the BCAL the energy deposit from the BCAL is used.

After the above energy corrections were implemented, an event-by-event correction factor was applied to the measured particle energy in order to correct for the non-uniformities coming from the cracks between towers and cells in the CAL.

The measurement of the impact position obtained from the CAL was improved in this analysis using the position reconstructions in the CTD, the SRTD and the RHES whenever the particle trajectory was within the respective acceptance regions.

Fig. 4.3 shows the average correction factor $E_{corr}/E_{CAL}$ due to inactive material and nonuniformities as a function of the radius $r = \sqrt{X^2 + Y^2}$ for events in the RCAL.

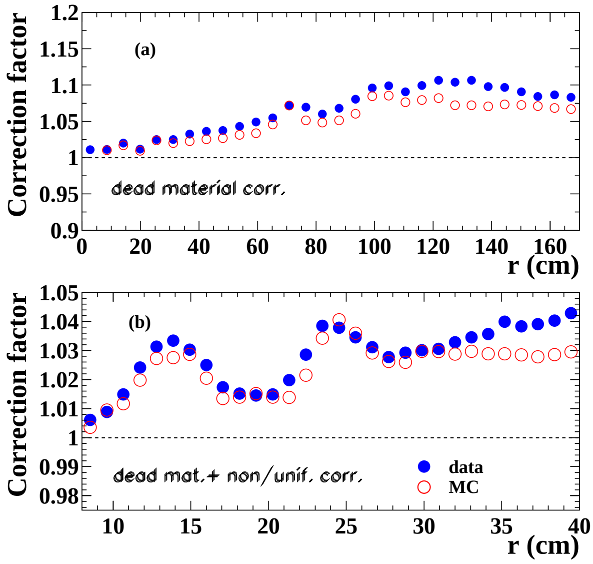


Figure 4.3: Correction factor for energy due to presence of (a) dead material and (b) dead matherial plus non-uniformities in the RCAL. The data points (solid circles) are compared with the Grape-Compton MC simulation (open circles).

## 4.3 Particle identification and reconstruction

The signature of a DVCS event in the CAL corresponds to the observation of the scattered electron and a real photon. An efficient identification and a correct reconstruction of both is, therefore, crucial. At low $t$ values, the momentum conservation forces the transverse momenta of the electron and of the photon to be balanced. Due to the back-to-back topology in the azimuthal angle, both particles are isolated and can easily be identified. The reconstruction of both particles is performed by an *electron finder* algorithm which analyzes the energy deposits in the electromagnetic and hadronic calorimeters and the origin of the electromagnetic clusters.

The energy deposits in the CAL are clustered into *islands*. The basic rule of forming an island is that a cell with the highest energy becomes the cluster seed and other neighbouring cells are associated with it. The connections are made to the highest energy neighbour or to the highest energy next to nearest neighbour. This procedure, is repeated for each cell and produces an unique assignment of a cell to an island.

The electron finder used in this analysis is SINISTRA [97, 98], a neural network which analyzes the islands in the whole calorimeter and returns the probability of each cluster to be an electron. Electrons and photons mainly leave all their energy in the electromagnetic section of the calorimeter, however there are other particles, such as $\pi^0$, leaving a similar signal in the CAL. The way to distinguish between electrons (photons) and pions is to look at difference in their shower profiles. This technique cannot be used to distinguish between electrons and photons because their shower profiles are very similar.

The neural network is trained with a MC sample of 4000 events [98] and after that a pattern of probability is produced. The result showed that electron clusters have a probability close to 1 while hadronic clusters have a probability close to 0.

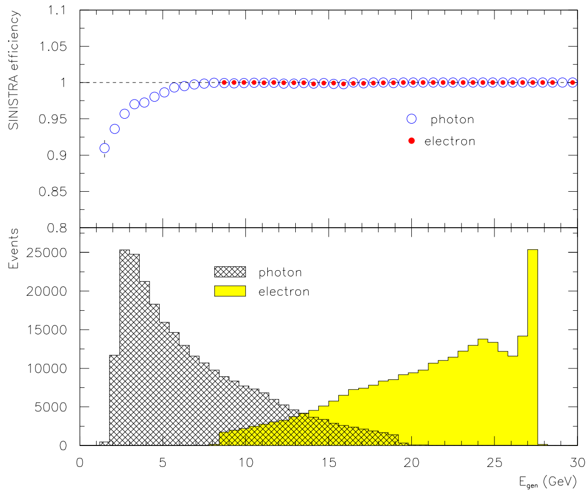


Figure 4.4: (Upper) The efficiency of the SINISTRA electron finder to find an electron (points) and photon (open circles) candidates as a function of the true particle energy based on the MC simulation. (Lower) Distributions of the true particle energy.

In fig. 4.4 the efficiency to find an electron or a photon candidate as a function of the true energy is shown. The efficiency was determined with the GenDVCS MC sample (see Sec. 3.2.1) generated for $Q^2 > 1\,GeV^2$. For electrons the efficiency is always close to 1, as their energy does not drop below 9 $GeV$ and they always hit the RCAL for which the electron finder was tuned to yield the highest efficiency. The photon efficiency is about 95%

at 2.5 $GeV$ reaching 100% at 7 $GeV$. At low energies the photon efficiency drops significantly, because a low energy electromagnetic particle may be faked by electromagnetic showers from $\pi^0 \rightarrow \gamma\gamma$ decays or by low energy hadrons from photoproduction events, where the scattered electron escapes down the beam pipe.

The energy of each SINISTRA candidate is calculated from the sum of energies over all cells belonging to an island.

The position of the cluster is calculated by the ELECPO [99] package. This algorithm studies the shower profile to properly determine the impact position of the particle. The $X$, $Y$ and $Z$ positions are calculated as a weighted average of the centers of the cells belonging to the candidates, where the weights are proportional to the logarithm of the energy deposited in that cell. For candidates in RCAL or FCAL the $Z$ position is fixed while for the ones in BCAL the radius $r = \sqrt{X^2 + Y^2}$ is fixed. SRTD and HES position measurements are used to improve the CAL position when the candidates are found in their acceptance.

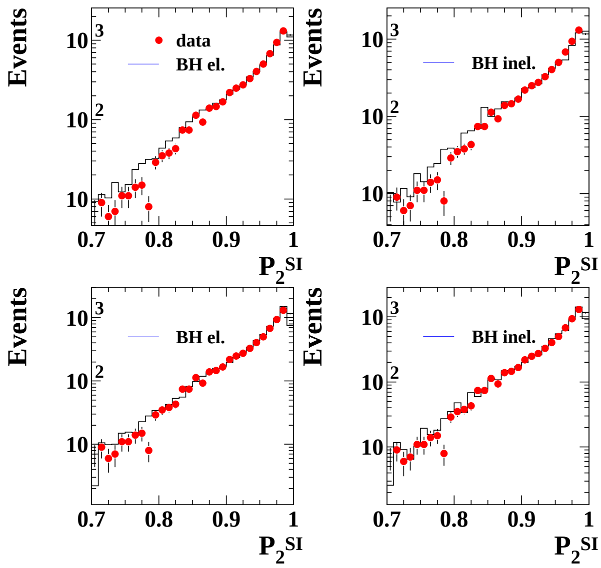


Figure 4.5: (Upper) Comparison of the data (dots) with the elastic and inelastic BH simulation (line) for the distribution of the SINISTRA probability of the second em candidate before the reweighing procedure. (Lower) Comparisonof the data (dots) with the elastic and inelastic BH simulation (line) for the distribution of the SINISTRA probability of the second em candidate after the reweighing procedure.

Figure 4.5(*upper*) shows the agreement between the data and the BH elastic and inelastic MC$_s$ for the SINISTRA probability to find the second electromagnetic cluster (EM2), $P_2^{SI}$. All selection critera (discussed in Sec. 5.2) together with the requirement of a positive-charged track pointing to the EM2 cluster were applied. The agreement is slightly bad at low probability values; the log scale imposed on the plot enphatizes this difference. Since $P_2^{SI} > 0.7$ will be a threshold in our data sample selection (see Sec. 5.2), a reweighting of the BH Monte Carlo was performed in order to achieve e better description of the data.

To study a proper reweight, the energy of the second SINISTRA candidate was divided in 20 bins within the intervall $2.5 < E_2 < 12.5\ GeV$ and for each bin the ratio $frac = \frac{P_2^{data}}{P_2^{MC}}$ between the data and the BH elastic MC events was calculated. The Result, depicted in fig. 4.6 as function of $E_2$, showed an excess of data at low energies. The function $frac$ was applied as weight to both BH elastic and inelastic MC$_s$. Figure 4.5(*lower*) shows the very good agreement of the data with the elastic and inelastic MC$_s$ after the reweighting procedure.

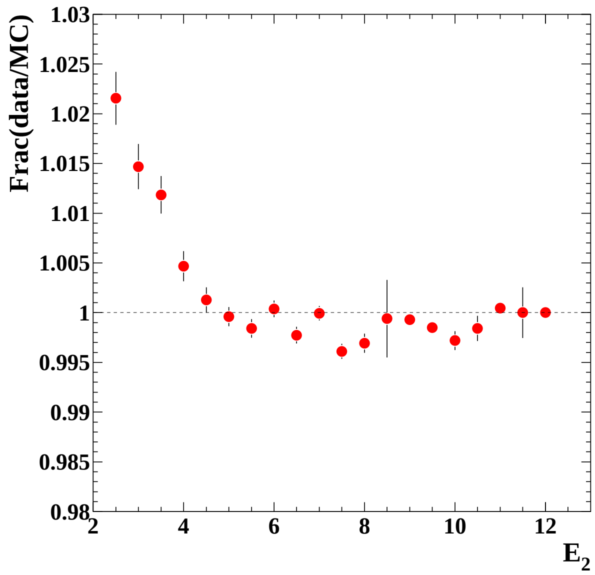


Figure 4.6: Fraction $frac = \frac{P_2^{data}}{P_2^{MC}}$ between the sinistra pobabilities, $P_2^{SI}$, for the data and the elastic BH simulation, as a function of the cluster energy.

### 4.3.1 The energy scale study

The energy scale due to the electromagnetic shower leakage in the calorimeter was studied in this work by the comparison of the energy, $E_2$, deposited in the CAL and the momentum of the track, $p_2$, measured in the CTD, for the second electron candidate, EM2, found by sinistra after all selection critera in Sec. 5.2 and the requirement of a positive-charged track pointing to the cluster. The following quantity was calculated

$$R_p = \frac{E_2}{p_2} - 1. \tag{4.2}$$

If the $R_p$ distribution is piked at 0 the energy scale is equal to 1 and no correction is need. This method povides an absolute energy scale of the response of the CAL indipendently in the data and the MC simulation.

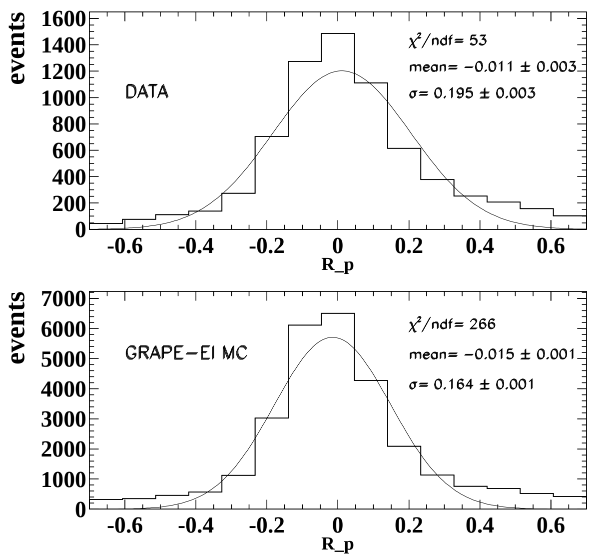


Figure 4.7: Distribution of $\langle R_p \rangle$ for the $e$ sample in the data (upper) and MC simulation (lower).

Figure 4.7 shows the $R_p$ distribution for data and MC events. A gaussian fit was performed for both distributions with the result

$$\langle R_p^{data} \rangle = 0.011 \pm 0.003,$$
$$\langle R_p^{MC} \rangle = -0.015 \pm 0.001,$$

for data and MC respectively.

An additional study of $R_p$ was performed in bins of $p_2$, which is the variable giving the best energy determination for a charged particle. The $e$ sample was divided into four bins of $2.5 < p_2 < 6.5$ $GeV$ and $\langle R_p \rangle$ was calculated for the data and the Grape MC simulation indipendently in each bin. Figure 4.8 shows $\langle R_p \rangle$ values as function of $p_2$ for both data and MC distribution. One can see that all the values are competible with zero for each $p_2$ bin within the uncertainties and also data and MC are compatible each other excepted the first bin. Figure 4.8 depicts also the value of the difference $\langle R_p^{MC} \rangle - \langle R_p^{data} \rangle$ for each bin of $p_2$ showing no significant difference within statistical uncertainties between data and MC. A linear fit was imposed and the trend resulted quite flat.

It can be achieved, as conclusion of this study, that MC does not show either a significant energy scale nor e significant difference with data and a correction is negligible for the proposals of this analysis.

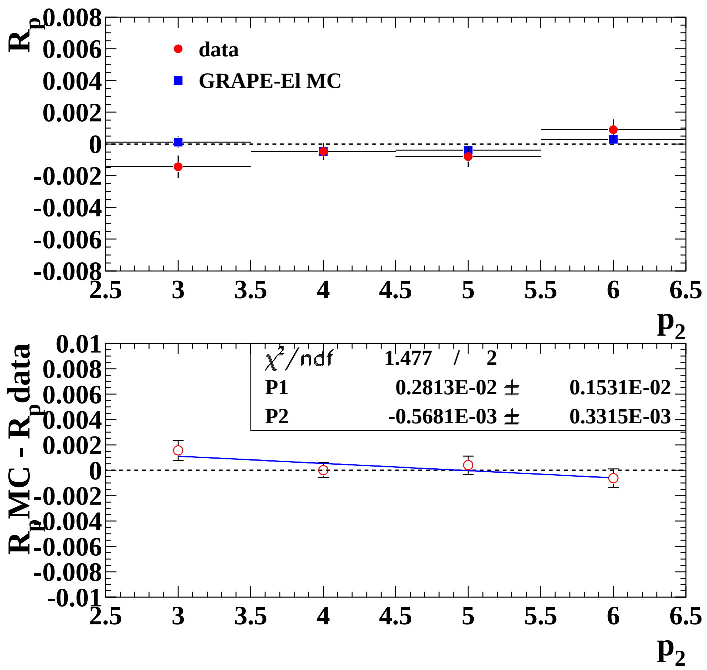


Figure 4.8: (Upper) Distribution of $\langle R_p \rangle$ as a function of $p_2$ for data (red dots) and MC simulation (blue squares). (Lower) $\langle R_p^{MC} \rangle - \langle R_p^{data} \rangle$ difference as a function of $p_2$ with a linear fit superimposed.

## 4.4 Kinematic veriables reconstruction

Measurement of the DVCS cross sections requires a precise determination of the kinematic variables.

The relevant kinematic variables for DVCS events can be determined from the energy and the polar angle of either the scattered electron or the photon or from any combination of two of these four variables together with the four-momenta of the electron and the proton in the initial state. The uncertainties of the kinematic variables depend on the detector resolution and on the chosen reconstruction method and vary strongly over the phase space.

The three methods used to determine kinematic variables $y$, $Q^2$ and $x$ are the following:

#### The electron method

The electron method [100] was used first in fixed target experiments. The formulae for kinematic variables are as follows

$$y_{el} = 1 - \frac{E'_e}{2E_e}(1 - \cos\theta'_e), \tag{4.3}$$

$$Q^2_{el} = 2E_e E'_e(1 + \cos\theta'_e), \tag{4.4}$$

$$x_{el} = \frac{E_e}{E_p} \cdot \frac{E'_e(1 + \cos\theta'_e)}{2E_e - E'_e(1 - \cos\theta'_e)}. \tag{4.5}$$

It seems to be the simplest method, since it requires only the measurement of the energy $E_e$ and the polar angle $\theta'_e$ of the scattered electron.

The $Q^2$ resolution in this method is quite good as long as the electromagnetic shower associated with the scattered electron is fully contained in the CAL. In general, the resolution of this variable depends on the resolution of the measurement of the electron polar angle and its energy. Its disadvantages are: a bad $x$ resolution at small $y$ and a large sensitivity to radiative effects. However, the $x$ resolution is very good at large $y$.

#### The double-angle method

The double-angle method (DA) [100] relies on the measurement of the electron polar angle $\theta'_e$ and the polar angle of the hadronic final state $\theta'_h$ (in case of the DVCS process it consists in the photon angle $\theta'_\gamma$). This method is motivated by the fact that usually angles are measured with better accuracy than energies. The kinematic variables are given by

$$y_{DA} = \frac{\sin\theta'_e(1-\cos\theta'_\gamma)}{\sin\theta'_e+\sin\theta'_\gamma-\sin(\theta'_e+\theta'_\gamma}, \tag{4.6}$$

$$Q^2_{DA} = 4E_e^2\frac{\sin\theta'_\gamma(1+\cos\theta'_e)}{\sin\theta'_e+\sin\theta'_\gamma-\sin(\theta'_e+\theta'_\gamma}, \tag{4.7}$$

$$x_{DA} = \frac{E_e}{E_p}\cdot\frac{\sin\theta'_e+\sin\theta'_\gamma+\sin(\theta'_e+\theta'_\gamma}{\sin\theta'_e+\sin\theta'_\gamma-\sin(\theta'_e+\theta'_\gamma}. \tag{4.8}$$

### The Jacquet-Blondel method

The Jacquet-Blondel method (JB) [101] relies entirely on the detection of the hadronic system. In case of the DVCS process when the proton goes downstream the beam pipe the measurement of an hadronic final state is synonymous with the measurement of the photon. This method is based on the assumption that the total transverse momentum carried by hadrons which are undetected in the proton beam pipe as well as the energy carried by particles escaping in the electron direction are negligible. The $JB$ method yields

$$y_{JB} = \frac{E'_\gamma(1-\cos\theta'_\gamma)}{2E_e}, \tag{4.9}$$

$$Q^2_{JB} = \frac{2E_e(E'_\gamma\sin\theta'_\gamma)^2}{2E_e-E'_\gamma(1-\cos\theta'_\gamma)}, \tag{4.10}$$

$$x_{JB} = \frac{Q^2_{JB}}{sy_{JB}}. \tag{4.11}$$

As can be seen in fig. 4.4 the $Q^2_{el}$ reconstruction is rather precise for large $Q^2$ values. The reconstruction of $W_{el} = 4E_eE_p\cdot y_{el}$ and $x_{el}$ is not good at low values of $W$ and $x$ because events tend to migrate from the low $y$ and $x$ range to the higher values of $y$ and $x$. According to that, in this analysis electron method was choosen for $Q^2$ reconstruction whereas duble angle method was used to calculate $y$ and then $W$ energy.

## 4.4.1 Kinematic variables resolution

A study of the resolution of the kinematic variables was performed using the MC sample based on the GenDVCS program by direct comparison of the reconstructed quantities, obtained after the full detector simulation, and the generated ones.

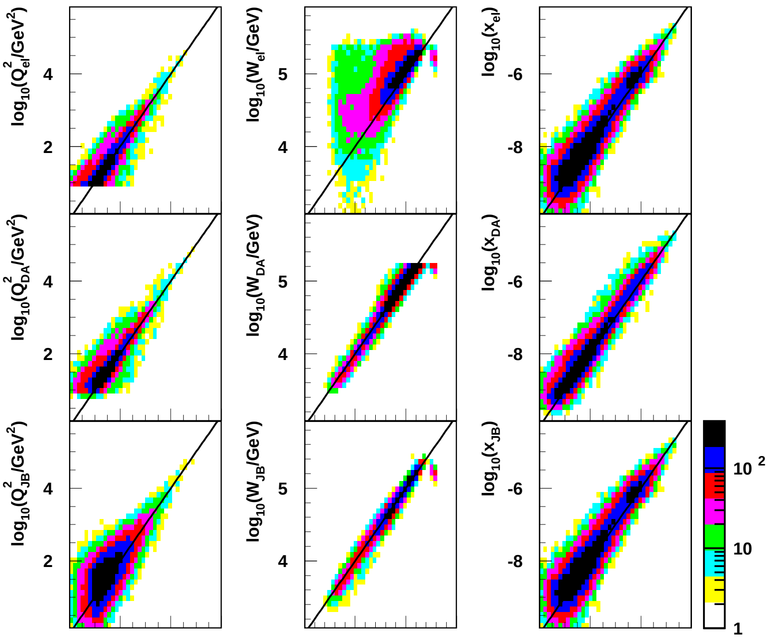


Figure 4.9: Reconstructed values of $Q^2$, $W$ and $x$ compared to the generated values (in abscissa).

The resolution for a generic variable $X$, defined as

$$Res = \frac{X_{rec} - X_{gen}}{X_{gen}}, \tag{4.12}$$

was calculated for several bins of the same variable at the generator level and for each bin a Gaussian fit was imposed to evaluate the distribution width. Then the resolution with its uncertainty is shown in fig. 4.10 for the kinematic variables $Q^2$, $W$, $x_l$ and $t$. The $W$ variable is reconstructed with the duble angle method and a resolution always below 11% whereas $Q^2$ is reconstructed using the electron method with a resolution below 21%. The resolutions for $x_L$ and $t$ variables are 1.2% and 24% respectively.

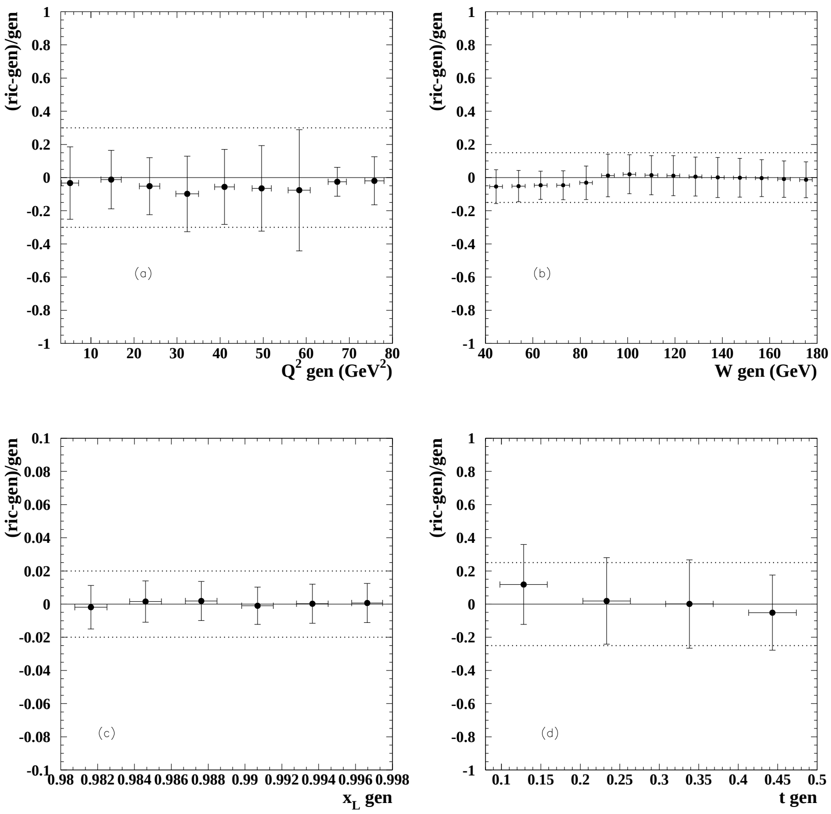


Figure 4.10: Resolution of the kinematic variables $Q^2$ (a), $W$ (b), $x_L$ (c) and $t$ (d) as a function of the corresponding generated variables.

# Chapter 5

# Selection of the DVCS events

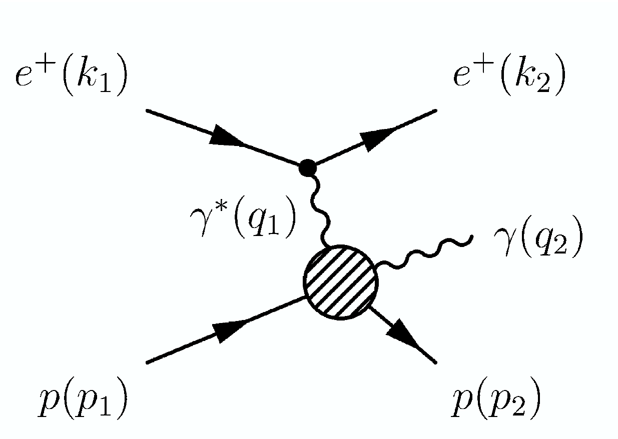


Figure 5.1: Diagram of a tipical DVCS event.

The final state topology of a DVCS event, shown in fig. 5.1 contains one track and two electromagnetc clusters together with a proton scattered at a very small angle. The technique for measuring the DVCS consists to first extract from the amount of data collected by ZEUS during the 1999-2000 $e^+$ data taking period a sample of events characterized by the DVCS topology. In order to select this sample a three level dedicated trigger was requered and then a set of off-line selection criteria was imposed.

The main source of back-ground for DVCS process is coming from Bethe-Heitler (BH) events (see Sec. 1.5) because they have the same final state, then the selected sample will contain a mixture of DVCS + BH. Assuming that interference between the two processes is suppressed (see Sec. 1.5), in a second step, the BH contribution can be subtracted from the sample using the MC predictions leading to a *pure* DVCS sample.

In this chapter the on-line and off-line DVCS selection is shown and the strategy to reduce the background is described in detail. Finally, the additional selection criteria used to extract a sample of events using the LPS detector to have a direct measure of $t$ four-momentum are listed.

## 5.1 Trigger selection

In order to select events in a particular physics channel, the ZEUS experiment implements different logic *slots* at each of the three levels trigger system in order to achieve the necessary rate reduction together with a high efficiency in selecting the physics events.

To select a good sample for the DVCS study it was required a trigger chain, dedicated to the selection of events with two electromagnetic clusters, named *QED Compton* trigger. It requires at the first level the logical slot FLT62. This slot triggers on two or more isolated electromagnetic (EM) clusters, ISOE. The cluster is considered as electromagnetic if more than 90% of its energy is deposited in the EMC. This slot yields a low rate and was not prescaled throughout the entire period of the data taking. The definition of ISOE depends on the region of the location of the EM cluster. If the cluster is located in the RCAL or in the BCAL then the condition $E_{ISOE} > 2\,GeV$ is imposed. If it is located in the FCAL, the energy threshold depends on the impact position in the FCAL ring: in the first ring is infinite, in the second ring $E_{ISOE} > 20\,GeV$, in the third ring $E_{ISOE} > 10\,GeV$ and outside the third inner ring $E_{ISOE} > 5\,GeV$.

Due to the specific definition of the FLT62 the efficiency of this slot strongly depends on the energy of a less energetic cluster. This effect was studied in this analysis and is described in Sec. 5.2.1.

On the basis of the FLT62 bit a more detailed trigger selection was carried out at the second level trigger (SLT) stage. At this level the full CAL information is available in terms of energy deposits and timing.

The SLT selection makes use of the SLT05 slot which is devoted to the QED-Compton study. At this stage more accurate clustering algorithms are available. The cuts on energy of the EM clusters are more restrictive depending on the impact position of a particle. If the cluster is located in the RCAL or in the BCAL, the condition imposed is $E^{RCAL,BCAL} > 2\,GeV$, whereas for the FCAL the threshold is $E^{FCAL} > 10\,GeV$. This high energy cut in the FCAL takes into account possibility of a detection of particles coming from the dissociation of the proton.

Moreover the SLT is used to reduce the *beam-gas* interactions background due to interactions between the beam and the residual gas in the beam pipe.

Beam-beam interactions can be distinguished from the beam-gas background thanks to the calorimeter timing. This is possible because *ep* interactions take place within the vertex region of the detector during the time interval defined by the bunches traversing the centre of the ZEUS detector contrary to the proton-gas interactions in the beam pipe.

Furthermore, events are vetoed at the SLT when one of the following conditions holds:

- $E - p_z + 2E_{LUMI\gamma} < 30\,GeV$,
- $E - p_z > 100\,GeV$,

where $E$ and $p_Z$ are the total energy and the longitudinal momentum assuming a nominal vertex position at 0, and $E_{LUMI\gamma}$ denotes the energy measured in the $LUMI\gamma$ calorimeter. This condition is formulated in a way to retain initial state radiation (ISR) events in which the incoming electron radiates a photon in the backward direction of the CAL.

Since each CAL cell is read out by two PMTs, a high PMT imbalance suggests that most of the energy deposited in the cell was sampled by only one PMT, while a low imbalance means that both PMTs sampled the same amount of energy. A very high imbalance which can be caused by a self-maintained discharge, is a signature of sparks. Sparks are suppressed at the SLT level by removing single isolated cells with the imbalance above the certain threshold.

The last stage of the trigger selection is the off-line third level trigger (TLT). At this level more refined electron finder algorithms for the electron identification can be used for event selection. The logical definition of the TLT for DVCS events can be described in the following way, assuming the logical AND between all the following conditions:

- zero hadronic islands with energy greater that 2 $GeV$,
- two EM islands,
- one EM island with energy greater than 4 $GeV$,
- another EM island with energy greater than 2 $GeV$,
- HAC0[3] islands are considered as EM ones,
- energy associated to the FCAL first ring is less than 50 $GeV$,
- difference of azimuthal angles for islands is greater than $\pi/2$ radians,

[3]HAC0 is the inner shell in the hadronic calorimeter

- $E - p_z > 30\,GeV$, where both quantities are calculated using the CTD tracks if they are available or CAL deposits are used otherwise.

In addition, the characteristic patterns of hit cells for cosmic muons and for muons which travel in the proton beam-halo are used at the TLT to reject these backgrounds. Moreover, tighter timing cuts comparing to the SLT selection as well as special algorithms to reject beam-halo are applied.

It can be noticed that the TLT trigger used in the DVCS analysis basically does not depend on the tracking information and is predominantly a calorimeter trigger.

## 5.2 Off-line selection criteria

As already introduced, the DVCS event topology shows two electromagnetic clusters in the final state while the proton, scattered at a very low angle, escapes trough the beam pipe. No hadronic activity is expected and only one track can be observed if the lepton steps within the CTD acceptance. This topology is common for DVCS and BH events with the only difference that the DVCS channel is dominated by a final state with a lepton closer to the beam pipe than the photon whereas for BH events the lepton angle can be, with the same probability, lower than the photon one. All selection requests are voted to select events having the DVCS topology which, for the kinematic range of this analysis, consists of a photon and a scattered electron with balanced transverse momenta.

The event sample obtained after the trigger selection chain still contains some contamination from unphysical processes (not originated from the *ep* interaction) and from other reactions with a different topology than DVCS (BH) events which must be removed.

The final selection was based on the two isolated EM clusters in the EMC. Henceforth we will denote as EM1 the cluster with the largest polar angle $\theta_1$, which means the cluster closer to the beam pipe in the rear direction, while the other cluster will be indicated as EM2.

The EM1 was required to be in the RCAL and the EM2 either in the BCAL or in the RCAL. In order to identify elastic events, there should be no additional signal in the CAL above the noise level. The following selection criteria were applied:

- EM1 in the RCAL with energy $E_1 > 10\,GeV$ and EM2 with polar angle $\theta_2 < 2.85\,rad$, either in the RCAL with energy $E_2 > 3\,GeV$ or in the BCAL with energy $E_2 > 2.5\,GeV$. The angular range of the EM2 corresponds to the limit of the CTD acceptance.

- At most one track in the CTD. If a track was found, it was required to match one of the EM clusters with a *distance of the closest approach*[4] (DCA) less than 20 $cm$.

- The probabilities $P_1^{SI}$ and $P_2^{SI}$ of being a scattered electron for the EM1 and EM2 clusters were required to be greater than 0.9 and 0.7, respectively. These variables are calculated by the SINISTRA95 electron finder.

- $40 < E - p_z < 70\,GeV$, where $E$ is the total energy and $p_z$ the sum of $E\cos\theta$ over the whole CAL. This requirement rejects photoproduction events and beam-gas background. Therefore, this cut also rejects events where photons, radiated from the incoming electrons, carry an energy.

- Total energy deposited in the FCAL was required to be less than 1 $GeV$ and the energy measured in the FPC to be less than 1 $GeV$ to suppress the proton-dissociative events.

- Energy in the hadronic part of the BCAL should be less than 1 $GeV$ to ensure that clusters are electromagnetic and, therefore, suppress background from hadrons.

- Calorimeter cells not associated with the two EM clusters in the CAL were required to have energy less than: 200 $MeV$ in the FEMC and 270 $MeV$ in the FHAC, 340 $MeV$ in the BEMC and 310 $MeV$ in the BHAC, 200 $MeV$ in the REMC and 240 $MeV$ in the RHAC. These thresholds were determined by means of randomly triggered events, requiring that only up to 0.1% of all events have the maximal cell energy above the threshold. This elasticity requirement as well as the next selection criterion rejects most inelastic events in which the proton dissociates into a hadronic system.

- If a vertex is reconstructed, its $Z$ coordinate is requested to be within the interval $-100 < Z_{vtx} < 50$ $cm$ in order to avoid satellite vertex events.

- *H1 box cut* was applied (see fig. 5.2, red line). All events for which a position of the EM1 cluster satisfied one of the condition: $|X_1| < 13\,cm$ and $|Y_1| < 8$ $cm$ were rejected. In the region in RCAL close to the beam hole the reconstruction of the energy and impact position of the electron is affected by energy leakage into the beam hole. In order to

[4]Distance of the closest approach is a distance of the cluster from the CTD track extrapolation.

ensure an accurate reconstruction of the EM1 cluster an above cut on its impact position at the RCAL surface was applied. It ensures a minimum distance to the edge of the RCAL hole of about 4 *cm*.

- The two regions in RCAL with

$$(X_1, Y_1) : \begin{cases} -13 < X_1 < -8\,cm & \text{and } Y_1 < 4\,cm \\ 8 < X_1 < 13\,cm & \text{and } Y_1 > -4\,cm \end{cases}$$

  were excluded from the analysis. This *calorimeter cracks cut*, shown fig. 5.2 (blue line), was applied due to the poor MC simulation of the energy leakage in the crack region between the north and the south halves of the RCAL, Another reason to reject these regions is the loss of efficiency of the electron finders in the cracks. Moreover, neither the SRTD nor the RHES fully cover the crack region which results in the poor reconstruction of the impact position.

- *Pipe cut* was applied (see fig. 5.2, green line). The position of the EM1 cluster $(X_1, Y_1)$ was required to be found in the RCAL outside the following four regions

$$(X_1, Y_1) : \begin{cases} -14 < X_1 < -7\,cm & \text{and } |Y_1| < 11\,cm \\ 4 < X_1 < 13\,cm & \text{and } |Y_1| < 11\,cm \end{cases}$$

  The average signal in the SRTD is approximately proportional to the amount of inactive material in front of the RCAL. It was shown [102] that the amount of the dead material is substantially higher in the regions close to the corners of the RCAL beam hole. Since the exact position and the amount of inactive material differs between the data and the MC simulation, it was decided to reject from this analysis events with hits in these regions.

After applying the above cuts, a total of 13084 events remains in the sample.

The analysis is splitted in two parts. First, to measure the cross section as a function of $Q^2$ and $W$, we applied a selection for DVCS events without any requirement about the outgoing proton excepted the request of no signal in the forword part of the ZEUS detector. Then a further selection was performed using informations on the scattered proton coming from the LPS spectrometer to have a direct measurement of $t$ four-momentum. This LPS sample is dedicated to the measurement of the differential cross section as a function of $t$ and the extraction of its $b$ slope.

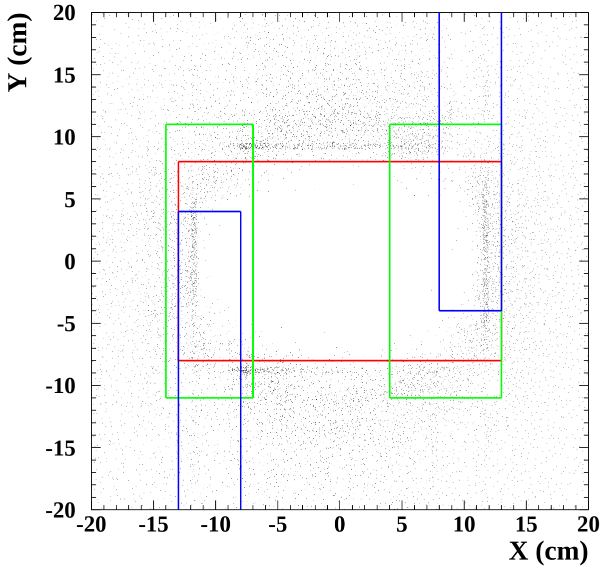


Figure 5.2: Coverage of the $X - Y$ plane in the Caloremeter. Colored lines show the CAL zone rejected by the H1 box cut (red line), caloremeter crack cut (blue line) and pipe cut (green line).

### 5.2.1 Trigger efficiency study

Since the definition of the FLT62 slot contains the cut on the cluster energy to be greater than 2 $GeV$, which is equal to the selection cut for the second SINISTRA candidate $E_2 > 2\ GeV$ in this analysis, the selection can be affected by threshold effects and the FLT62 trigger efficiency as a function of $E_2$ has to be studied.

Trigger slots are also simulated for MC events and both data and MC events pass through the same trigger chain. Therefore the simulation should reproduce the data behavior and FLT62 trigger efficiency must be compared between data and MC.

To study the FLT62 efficiency, the independent trigger bits,FLT30 and [DST52 or DST53], were selected. They are performed for inclusive DIS data, do not have a low energy cut in their definition and they are not prescaled.

A data sample was selected requering one track pointing to the BCAL or to the RCAL cluster and at least one isolated EM cluster in the RCAL, satisfying all cuts defined in Sec. 5.2. Additionally more restrictive conditions were imposed on the selection:

- one track originating from a vertex and associated to the low energy cluster,

- $Z_{vtx}$ coordinate of the vertex satisfying $|Z_{vtx}| < 50\,cm$ to exclude *satellite bunches* taking part in the interaction,

- $dE/dx > 1.2$, where $dE/dx$ is the energy loss in the CTD normalised to $dE/dx$ for pions in the momentum range $0.3 - 0.4\,GeV$,

- $0 < Z_{width} < 0.7$, where $Z_{width}$ is the energy weighted width of the cluster in the $Z$ direction. It is defined as

$$Z_{width} = \frac{\sum_i(|Z^i_{cell} - \bar{Z}|.\, E^i_{cell})}{\sum_i E^i_{cell}} \tag{5.1}$$

  where $E^i_{cell}$ and $Z^i_{cell}$ denote the energy and $Z$ coordinate of the i-th cell and $\bar{Z}$ stands for the average $Z$ coordinate of the EM cluster. The sum is over all cells of the EM cluster.

Using this sample, the FLT62 trigger efficiency has been calculated as a function of the energy $E_2$ by the following definition

$$\mathit{Efficiency} = \frac{N^{FLT62}}{N^{sample}}, \tag{5.2}$$

where $N^{sample}$ is the number of events in the sample selected by means of the all analysis selection criteria excluding the FLT62 trigger requirement, cuts defined above and independent triggers whereas $N^{FLT62}$ is the number of events in the sample with in addiction the FLT62 requirement.

Efficiency has been calculated for data and MC (GRAPE) separately. Figure 5.3 shows the FLT62 trigger efficiency as a function of $E_2$ for the three data sets divided on two cases when the cluster is either in the BCAL or in the RCAL. The FLT62 trigger efficiency is significantly below 50% for $E_2 < 2\,GeV$ and for higher $E_2$ values it grows up rapidly reaching almost 100% at $E_2 \approx 6(5)\,GeV$ in the BCAL (RCAL).

Finally, the difference between the FLT62 trigger efficiency for the data and the MC simulation has to be corrected. To match the behavior of data and MC, a correction factor $we(E_2)$ defined as

$$we(E_2) = \frac{\mathit{Efficiency}(data)}{\mathit{Efficiency}(MC)} \tag{5.3}$$

has been applied to MC events.

Figure 5.4 shows $we(E_2)$ for clusters in BCAL and RCAL separately.

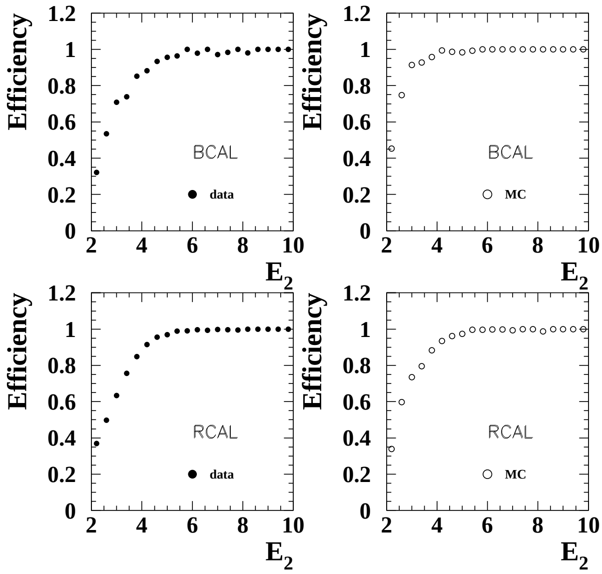


Figure 5.3: FLT62 trigger efficiency as a function of $E_2$ for data (dots) and MC simulation (circles) in the BCAL (up) and the RCAL (down) separately.

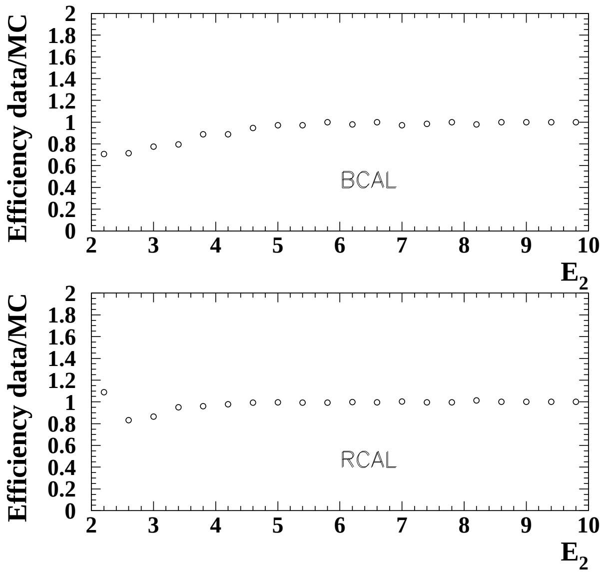


Figure 5.4: FLT62 trigger efficiency correction factor as a function of $E_2$ in the BCAL (on) or in the RCAL (down).

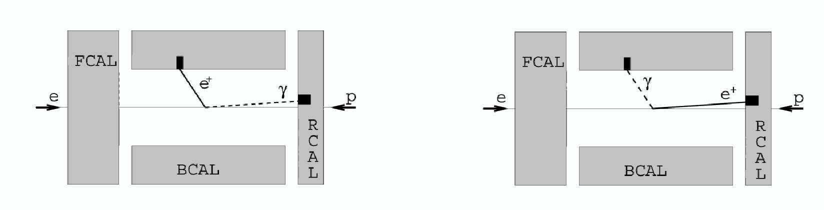


Figure 5.5: Topology of events in the $e$ sample (left), with a positive charge track fitting the EM2 candidate and in the $\gamma$ sample (right), with no track pointing to the EM2 candidate.

## 5.3 Analysis strategy

The sample selected as in Sec. 5.2 mainly contains events belonging to both DVCS and BH reactions. It is possible to obtain a pure DVCS sample only after the BH contribute subtraction. Here the strategy followed to obtain data samples for DVCS and BH reactions without background from other physics processes is presented.

All the events surviving the selection cuts were subdivided into three samples defined as follows:

- $\gamma$ ***sample***: this sample contains events with no track pointing to the second electromagnetic candidate EM2, which is then identified as the photon(see fig. 5.5, right), whereas EM1 is the scattered electron candidate. Both BH and DVCS processes contribute to this topology. The sample consisted of 4570 events.

- e ***sample***: this sample contains events with a positive-charge track pointing to the second candidate EM2, which then corresponds to the scattered positive-charge electron whereas EM1 is identified as the real photon. This topology (see fig. 5.5, left) is dominated by BH processes. The contribution from DVCS is predicted to be negligible, due to the large $Q^2$ required for a large electron scattering angle. This sample contained 8027 events.

- ***wrong-sign*** e ***sample***: this sample contains events with a wrong-charge-sign (negative in this analysis) track pointing to EM2 candidate. It may have originated from the $e^+e^-$ final state accompanying the scattered electron, where one of the right-sign electrons escaped the detector. This background sample is due mainly to non-resonant $e^+e^-$ production and to $j/\psi$ production with a subsequent decay in an electron-positron pair. Other sources are found to be negligible, as will be discussed in Sec. 5.3.1. This sample consisted of 487 events.

The wrong-sign-$e$ sample was used to subtract the background contributions to the $e$ sample and gain a pure BH sample. The pure BH sample was then used to statistically subtract the BH contribution to the $\gamma$ sample obtaining a pure DVCS sample.

In the following, the main background sources contributing to the DVCS process are investigated.

### 5.3.1 $e$ sample background study

Although the $e$ sample is dominated mainly by BH events, additional processes can contribute to the same event topology as the BH events in the $e$ sample: the elastic and inelastic dilepton production in two-photon interactions and the diffractive electroproduction of vector mesons with a lepton pair in the final state.

The dilepton and vector mesons production processes were studied using the wrong-sign-$e$ sample, because both processes have a wrong-charged electron in the final state. Processes contributing to the wrong-sign-$e$ sample also contribute to the $e$ sample with the same probability, then the wrong-sign-$e$ sample can be used to obtain the estimation of a number of events for the processes contributing to the background in the $e$ sample.

The first investigated source of background was the elastic and inelastic dilepton production in two-photon events, $ep \to ee^+e^-p$ and $ep \to ee^+e^-X$. It can contribute to the same event topology as the BH events when one of the final-state electrons escapes detection, so only two of them are observed in the CAL. Moreover, if a track associated with one of detected electrons is not measured in the CTD due to a large polar angle, this electron is classified as a photon in the $e$ sample. The second observed electron deposits an energy either in the RCAL or in the BCAL. If the charge of a track is the same as the initial electron, the event is classified to the e sample, otherwise the event is recognised as belonging to the wrong-sign-$e$ sample. The third electron is not seen in the CAL either because an energy deposit is less than the noise level or due to a very small or very large polar angle not being within the CAL coverage.

The dilepton production was studied using events belonging to the wrong-sign-$e$ sample and simulated by GRAPE-Dilepton MC. The samples for the elastic and inelastic dilepton events were normalized at the respective cross section and mixed together with a fraction of 70% and 30% respectively. In fig. 5.6 distributions of $W$ and $Q^2$ are shown for the wrong-sign-$e$ sample representing the data and the MC dilepton events. Nevertheless, the excess of events observed in high $W$ and low $Q^2$ region over the MC expectation,

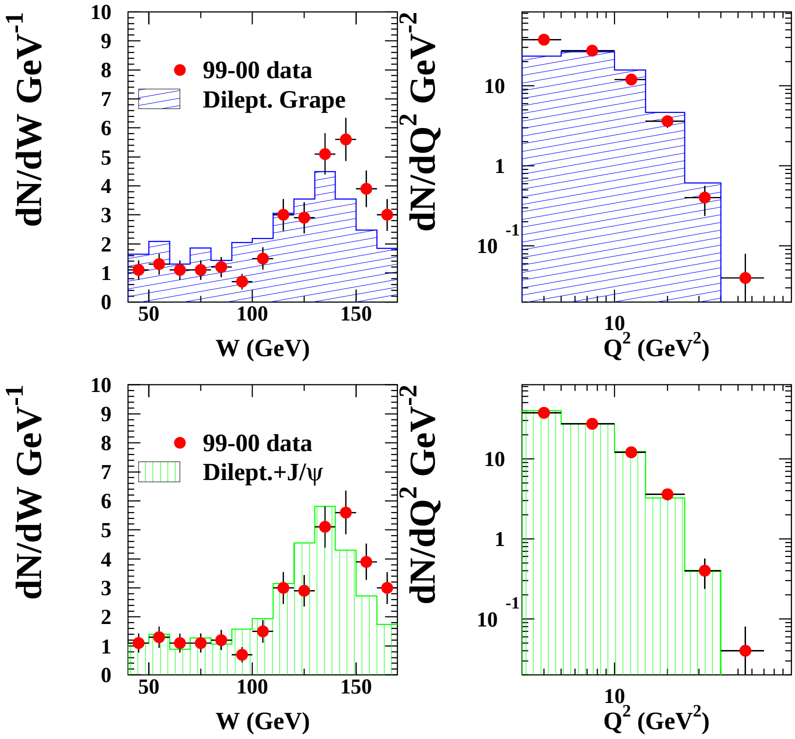


Figure 5.6: Distributions of $W$ (left) and $Q^2$ (right) for the wrong-sign-$e$ sample. The 99-00 data (dots) are compared with the GRAPE-Dilepton MC expectation (histograms).

suggested that an additional process can contribute to the wrong-sign-$e$ sample.

It was then taken in to account the diffractive elastic $J/\psi$ vector-meson electroproduction $ep \to e(J/\psi)p$, with $J/\psi \to e^+e^-$. It can yield the same event topology as the $e$ sample, when one of the final-state electrons escapes detection.

This background was also studied by means of the wrong-sign-$e$ sample. $J/\psi$ events can contribute to this sample when the opposite-charged electron is detected while the right-charged one escapes detection. In Fig. 5.6 the wrong-sign-$e$ sample is compared to the sum of two background contributions from the dilepton and $J/\psi$ electroproduction processes. Using the $\chi^2$ minimisation method, it was found that the best description of the data is for 31% dilepton and 69% $J/\psi$ events.

It was then investigated a possible background to the $e$ sample coming from the diffractive $\rho$ vector-meson electroproduction $ep \to e\rho p$, with $\rho \to \pi^+\pi^-$. This process can also contribute to the wrong-sign-$e$ sample as it has charged particles in the final state which can fake the electron signal.

A reach MC sample was generated for $\rho$ vector-mesons production simulation using the ZEUSVM software. After the wrong-sign-$e$ sample selection was imposed and the normalisation at the luminosity of data required, it was found that the contribution the contribution from $\rho$ vector-meson production to the wrong-sign-$e$ and then to the $e$ sample is negligible.

The other sources of background taken into account as a potential contribution to the $e$ sample are:

- diffractive $\phi$ meson electroproduction ($ep \to e\phi p, \phi \to \pi^0\pi^+\pi^-$),
- diffractive $\omega$ mesons electroproduction ($ep \to e\omega p, \omega \to \pi^0\pi^+\pi^-$).

All these processes were studied in detail in [103] by the generation of dadicated $\mathrm{MC_s}$ and it was fount that their contribution is negligeble an our phase space, after all selection criteria are applied.

Finally, it can be concluded that the $e$ sample consists only of the elastic and inelastic BH processes which altogether comprise about 92% of this sample. Remaining events comes from the dilepton production and diffractive $J/\psi$ electroproduction processes, all other background sources were found to be negligible within the phase space of this work.

Figure 5.7 shows several distributions for the $e$ sample compared to the MC predictions for the BH process, dilepton production and diffractive $J/\psi$ electroproduction events. The MC distributions are normalised to the data in such a way that the sum of dilepton and $J/\psi$ events is normalised to the wrong-sign-$e$ sample, then this normalised background is added to the MC expectations for the BH process and a final normalisation is established to the total number of events in the $e$ sample. One can see that the MC predictions are in good agreement with the data.

### 5.3.2 $\gamma$ sample background study

The final selection criteria to extract elastic DVCS events from the data also select a small fraction of inelastic events in which secondary particles of the low-mass hadronic system escape detection in the CAL. This proton-dissociative background arises in the $e$ sample as well as in the $\gamma$ sample.

Measurements of the elastic vector-meson production performed by the ZEUS collaboration [104, 48] have found that, with relatively high uncertainties, the fraction of proton-dissociative events in diffractive interactions is process independent. Since the DVCS MC program used in this analysis

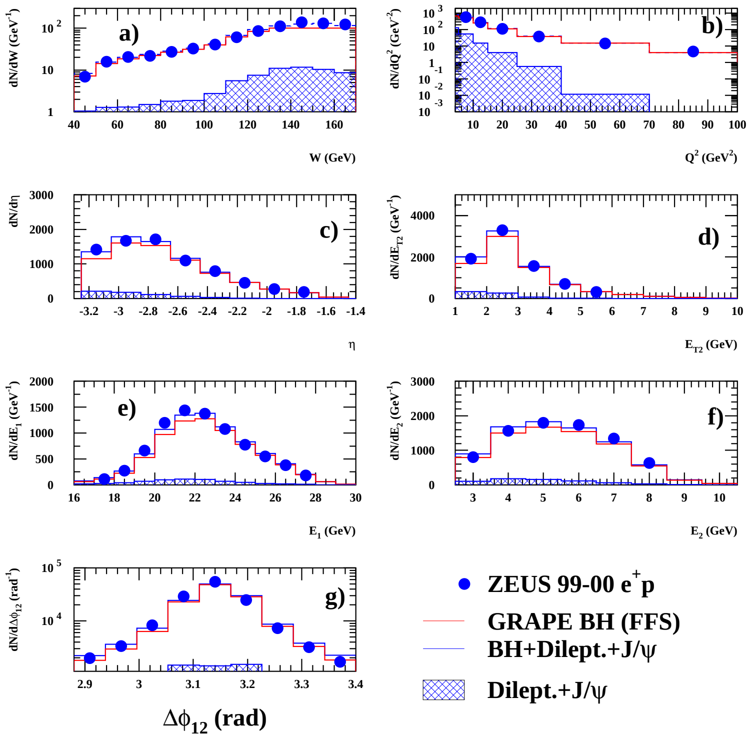


Figure 5.7: Distributions of the $e$ sample in (a) $W$, (b) $Q^2$, (c) $\eta_2$ - the pseudorapidity of the electron, (d) $E_T^2$ - the transverse energy of the electron, (e) $E_1$ - the energy of the photon, (f) $E_2$ - the energy of the electron, and (g) $\Delta\phi_{12}$ the difference in the azimuthal angles of $\gamma$ and $e$. The data are represented by the points and the histograms represent: the sum of the prediction of GRAPE for the BH process and dilepton and $J/\psi$ background (solid); the prediction of GRAPE for the BH alone (dashed) normalised to the data (including elastic and inelastic BH contributions); and the prediction of the dilepton and $J/\psi$ alone (hatched).

doesn't simulate the inelastic DVCS processes, as estimation of the DVCS inelastic ontribution was taken the fraction $F_{p.diss}$ determined in [48] for diffractive $J/\psi$ photoproduction measurements in the 98-00 data taking period

$$F_{p.diss} = 17.5 \pm 1.3(stat.)^{+3.7}_{-3.2}(syst.)\%.$$

The estimation a fraction of inelastic BH events in the data is based on the fact that the GRAPE MC program can generate the elastic as well the inelastic contributions to both samples and this inelastic component can be used to the proton-dissociative background study. For a clean sample of the elastic BH events one should observe a balance of the transverse momenta of the two final-state particles. It means that the difference of the azimuthal angles $\Delta\phi_{12}$ for these two particles should have a peak very close around $\pi$ radians, whereas a larger distribution reflects mainly the inelastic background.

Analysing the data belonging to the $e$ sample, it was found that the difference in the azimuthal angles $\Delta\phi_{12}$ for EM1 and EM2 clusters is not well described by the elastic GRAPE MC component solely. The addition of the inelastic contribution improves the agreement between the data and the GRAPE MC expectation. Figures 5.8a to 5.8c show the $\Delta\phi_{12}$ distribution for the elastic and inelastic GRAPE MC sample and the data, respectively. Mixing up the elastic and inelastic components of the MC events and fitting to the data in order to minimise the $\chi^2$ function (see Fig. 5.8e), it was found that the best description of data by GRAPE is achieved for $87 \pm 8\%$ of the elastic component, so the BH inelastic contribution is completely campatible with the estimated value $F_{p.diss}$ for the proton dissociation in diffractive reactions. Figure 5.8d depicts the comparison of the $\Delta\phi_{12}$ distribution for data with the best mixture of the elastic and inelastic MC components of the BH process. One can see that mixed GRAPE MC describes the data.

A possible contribution to the $\gamma$ sample background coming from vector-meson and dilepton production was also investigated using the MC samples generated for the $e$ sample back ground study but none of these processes survived the $\gamma$ sample selection

After all studies were performed, it can be concluded that the $\gamma$ sample consists only of the elastic and inelastic DVCS events as well as the elastic and inelastic BH background which comprises about 63% of this sample. Figure 5.9 shows the fraction of the BH contamination in the $\gamma$ sample. One can see that at low $W$ values the BH contribution is negligible whereas at high $W$ values it reaches the 80% of the sample.

A proper estimation of the number of BH events contributing to the sample is then a crucial point for the subsequent extraction of the DVCS

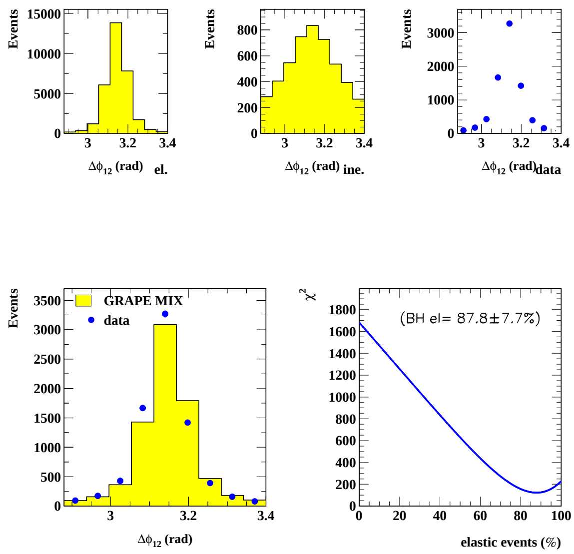


Figure 5.8: Distribution of the difference in the azimuthal angle for an electron and a photon $\Delta\phi_{12}$ for the BH process; (a) elastic component of the GRAPE MC sample, (b) inelastic component of GRAPE, (c) the 99-00 data, (d) the comparison of the data (points) with the best mixture of the elastic and inelastic MC components (histogram), (e) the $\chi^2$ distribution as a function of the fraction of elastic contribution to the BH process.

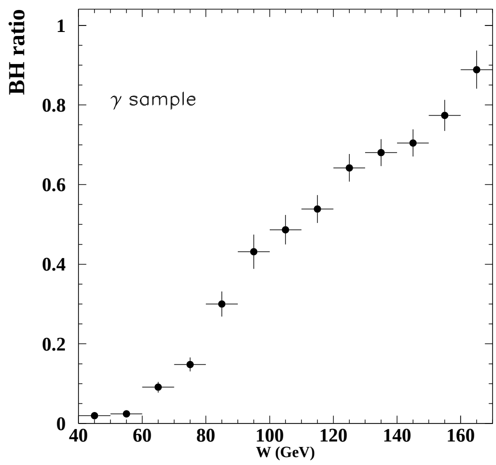


Figure 5.9: Fraction of the BH contamination in the $\gamma$ sample as a function of the $W$ energy.

cross sections. An absolute normalisation of the GRAPE MC sample was done according to the predicted BH cross section.

Figure 5.10 shows several distributions for the $\gamma$ sample after the BH background subtraction. The data are compared with the GenDVCS MC prediction, normalised to the number of data, for many variables distribution: $W$, $Q^2$, the rapidity and the energy of the two electromagnetic clusters and the difference in their azimuthal angles.

## 5.4 LPS sample

In the previous three selected samples the presence of a low angle scattered proton is simply guaranteed by the lack of signal in the forward region of the detector.

A further data sample was performed to measurement of the DVCS differential cross section as a function of $t$. This sample was selected using events which pass trough the previous selection criteria together with the request of the presence of a scattered proton identified by the LPS detector.

The addictional requests for this sample are:

- $x_L > 0.96$ and $x_L < 1.04$;
- $|t| > 0.07\,GeV^2$ and $|t| < 0.53\,GeV^2$;
- $E + p_z < 1865\,GeV$;
- distance of minimum approach of the proton track to the beam pipe $> 0.04\,cm$.
- the $X$ coordinate measured in each LPS station must be greater than 33 $cm$ due to a bud Monte Calro sibulation of the detector below this treshold.

The kinematic phase space is the same as before.

After all these selection criteria the LPS sample contained 55 events: 33 in the $\gamma$ sample, 20 in the $e$ sample and 2 in the wrong-sign $e$ sample.

The principal source of background in the LPS sample are *beam-halo* interactions coming from the interaction between the proton beam and the residual gas into the beam pipe or with the proton beam magnets. These tracks have an energy close to the proton beam and give a signal at $x_L = 1$ in the LPS in coincidence with an $ep$ interaction in the main detector.

Because there is not any correlation, for these events, between the LPS and ZEUS signals, the measured total hadronic energy is not necessarely

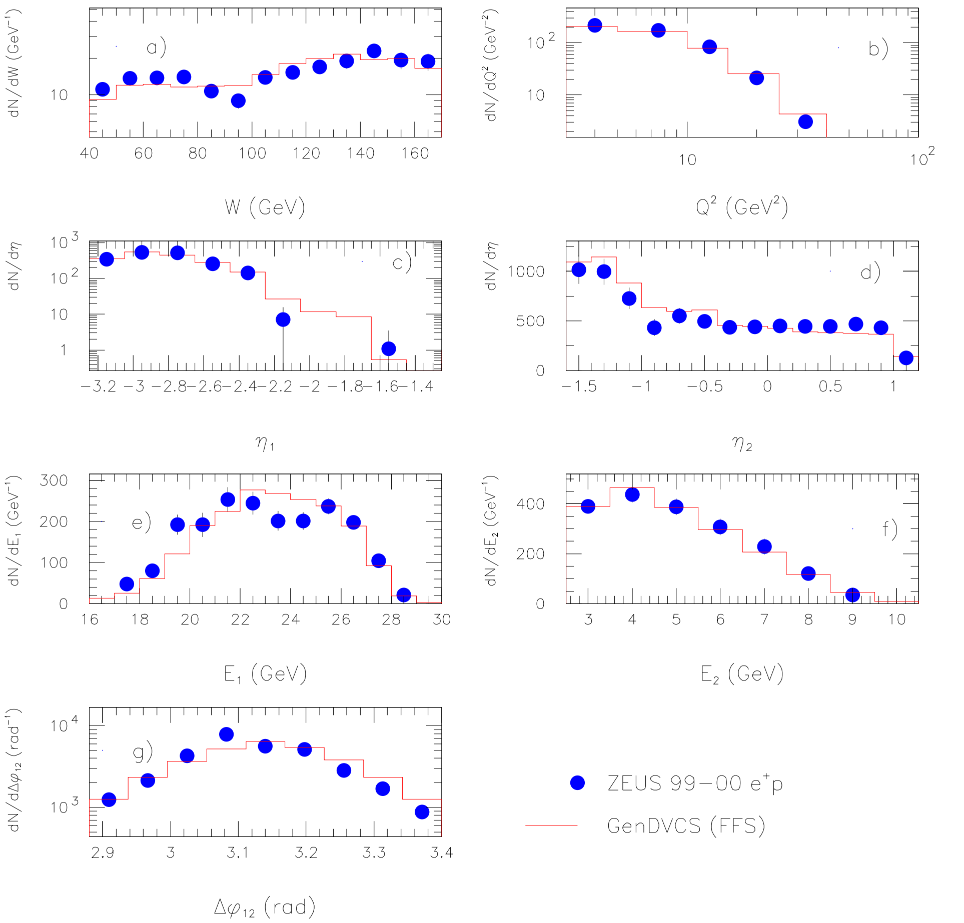


Figure 5.10: Distributions of the $\gamma$ sample in (a) $W$, (b) $Q^2$, (c) $\eta_1$ - the pseudorapidity of the electron, (d) $\eta_2$ - the pseudorapidity of the photon, (e) $E_1$ - the energy of the photon, (f) $E_2$ - the energy of the electron, and (g) $\Delta\phi_{12}$ the difference in the azimuthal angles of $\gamma$ and $e$. The data are represented by the points and the histograms represent the prediction of GRAPE for the BH process, normalised to the $e$ sample (including elastic and inelastic contributions).

conserved and the variable $E+p_z+2\cdot p_z^{LPS}$[5] can be used to reject part of the background. If the event is completely contained into the calorimeter, this quantity should be equal to $2\cdot E_p$ (1840 $GeV$ in the data taking period of this analysis) while beam halo events can overcome this value. The beam halo background in the an LPS diffractive sample was studied in [105] and it was found that for $E+p_z+2\cdot p_z^{LPS} > 1860$ beam halo dominate, so these events are rejected in this work. Morover, a low part of the beam halo background still persists at $E+p_z+2\cdot p_z^{LPS} < 1860$ and it was estimated to be $\sim 3\%\pm0.1\%$ of the total sample, which is negligible in this analisis due to the really poor statistics.

The strategy to obtain a pure DVCS sample is the same early described in Sec . 5.3. In fig. 5.11 the procedure is summarized depicting the data/MC comparison for the variables $x_L$ and $t$ in different samples: on the top is shown the data/MC comparison for the $e$ sample, in the middle the $\gamma$ sample shape is depicted and on th bottom the final data/MC agreement, after subtraction of BH contribution from the $\gamma$ sample, is presented. It was found a negligible background to the $e$ sample whereas a contamination of 22% BH elastic events in the the $\gamma$ sample was achieved. This contamination is much lower than in for the analisys without the LPS spectrometer mainly because the presence of a leading proton in this detector totally suppresses any inelastic contribution to the background.

[5]where $E$ and $p_z$ are measured by the caloremeter and $p_z^{LPS}$ is the proton momentum measured in the LPS

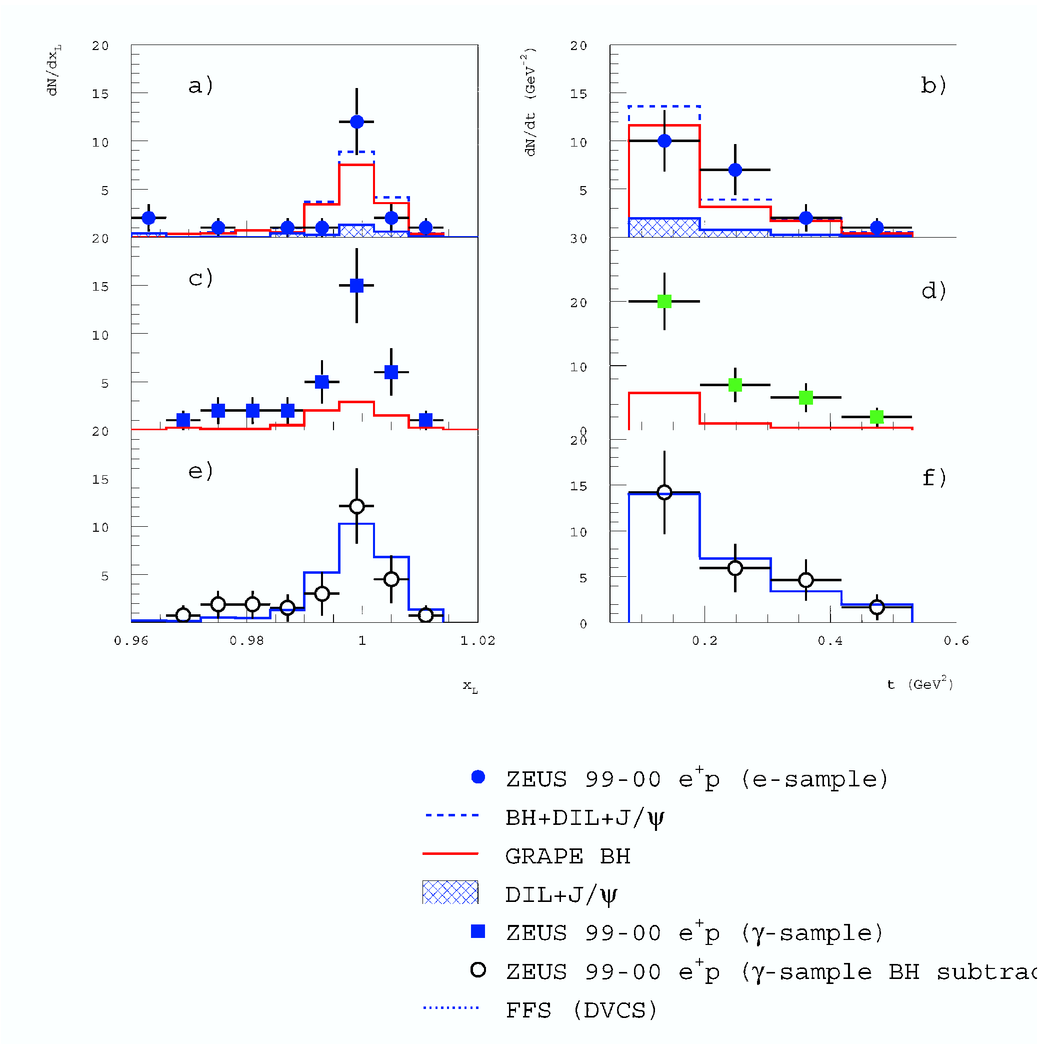


Figure 5.11: Distributions of $x_L$ and $t$ variables for the LPS sample. On the top data (blue dots) in the $e$ sample are compared with the BH MC (red line) and with MC including VM contribution (green dashed line), VM contribution is superimposed (blue histogram). In the middle data (green quadrats) in the $\gamma$ sample are compared with the BH MC (red line). On the bottom data (white circles) in the DVCS sample (cleaned $\gamma$ sample) are compared with DVCS MC (dotted line).

# Chapter 6

# Cross sections extraction

In the previous chapter has been shown the feasibility of a good DVCS data sample extraction, in a large kinematic region of $Q^2$ and $W$, from the whole data sample collected during the ZEUS 1999-2000 $e^+p$ running period. Moreover the possibility of the selection of a data subsample where the information on the scattered proton momentum is available was presented.

This chapter will show how the selected DVCS sample has been used to calculate the DVCS cross sections for the processes $e^+p \rightarrow e\gamma p$ and $\gamma^* p \rightarrow \gamma p$ as a function of $Q^2$ and $W$. Morover the extraction, from the restricted sample selected using the LPS, of the differential $\gamma^* p$ cross section as a function of $t$ will be presented together with its slope value $b$.

## 6.1 Efficiency, purity and acceptance

The aim of this analysis is to extract the cross sections as a function of $Q^2$ calculated with the electron method (see Sec. 4.4), $W$ calculated using the double angle method (see Sec. 4.4) and $t$ directly measured by the LPS spectrometer. The DVCS data sample was opportunely binned, according to the statistical precision of the data and the resolution of each kinematic variable, in 7 bins for $3 < Q^2 < 100$ $GeV^2$ and 13 bins for $40 < W < 170$ $GeV$. The quality of the binning can be determined introducing, for each bin $i$, the efficiency $\mathcal{E}_i$, purity $\mathcal{P}_i$ and acceptance $\mathcal{A}_i$ defined, for the MC

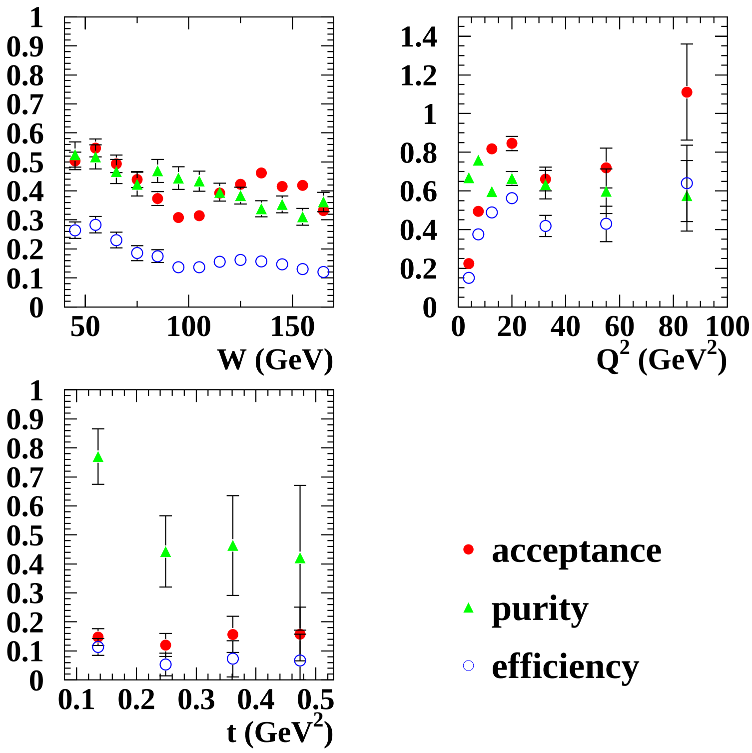


Figure 6.1: Bin acceptance( red dots), purity (green triangles) and efficiency (blue circles) for the $W$, $Q^2$ and $t$ variables.

sample, as

$$\mathcal{E}_i = \frac{N_i^{gen\,\&\,meas}}{N_i^{gen}},$$
$$\mathcal{P}_i = \frac{N_i^{gen\,\&\,meas}}{N_i^{meas}},$$
$$\mathcal{A}_i = \frac{N_i^{meas}}{N_i^{gen}},$$

where $N_i^{meas}$ is the number of events measured in the $i$-th bin after all selection criteria, $N_i^{gen}$ is the number of generated events in the $i$-th bin and $N_i^{gen\,\&\,meas}$ represents the number of events measured in the same bin in which they have been generated.

The previous three quantities are linked by the relation

$$\mathcal{E}_i = \mathcal{P}_i \cdot \mathcal{A}_i \tag{6.1}$$

The efficiency is an expression of the probability that an event is reconstructed in the same bin in which it was generated. The bin purity is an estimation of migration from an adjacent bin to the measured one. The acceptance checks the effect of the trigger and off-line selection criteria on the measured number of events. The overall acceptance is due to various factors, mainly to geometrical acceptance of the detector, trigger efficiency, reconstruction efficiency.

Figure 6.1 shows the efficiency, purity and acceptance for each bin of $W$, $Q^2$ and $t$ variables.

## 6.2 Extraction of the $ep$ and $\gamma^*p$ cross sections

In the kinematic region of this analysis the interference between the DVCS and BH processes is negligible when the cross section is integrated over the angle between the $e$ and $p$ scattering planes [32, 29]. Then the cross section for exclusive production of real photons may be treated as a simple sum of the contributions from the DVCS and the BH processes. The latter can, therefore, be subtracted and the DVCS cross section determined.

The DVCS differential cross sections as a function of a generic kinematic variable $X = Q^2$, $W$, $t$, described in [33] and discussed in Section 1.5.1, have been experimentally extracted, for $ep \to \gamma p$ and $\gamma^*p \to \gamma p$ processes, according to

$$\frac{d\sigma(ep \to e\gamma p)}{dX_i} = \frac{\mathcal{L}^{MC}}{\mathcal{L}^{data}} \cdot \frac{N_i^{evt}(1 - f_{p.diss.})}{N_i^{MC}} \cdot \frac{d\sigma_{DVCS}^{FFS}(ep \to e\gamma p)}{dX_i}, \quad (6.2)$$

$$\sigma(\gamma^*p \to \gamma p)(X_i) = \frac{\mathcal{L}^{MC}}{\mathcal{L}^{data}} \cdot \frac{(N_i^{evt})(1 - f_{p.diss.})}{N_i^{MC}} \cdot \cdot\, \sigma_i^{FFS}(\gamma^*p \to \gamma p)(X_i), \quad (6.3)$$

where $N_i^{evt} = (N_{observed} - N_{background}^{BH})_i$ is the number of DVCS events observed in the $i - th$ bin after the BH background subtraction, $N_i^{MC}$ is the number of DVCS events reconstructed by Monte Carlo, $f_{p.diss.}$ is the fraction of events of proton dissociation (see Sec. 5.3.2), $\mathcal{L}^{data}$ and $\mathcal{L}^{MC}$ are the integrated luminosities for data and Monte Carlo, finally, $\sigma_{DVCS}^{FFS}(ep \to \gamma p)$ and $\sigma_{DVCS}^{FFS}(\gamma^*p \to \gamma p)$ are the cross sections calculated following the FFS model (see Sec. 1.5.1) which includes the radiative corrections.

## 6.3 Systematic uncertainties

The systematic uncertainties on the measured cross sections were determined by changing the selection criteria according to the resolution of the corresponding variables. The following checks were performed (numbers in brackets are the bits used to indicate each systematic check)

- $DCA < 15\ cm$ (1) and $DCA < 25\ cm$ (2),
- $P_1^{Si} > 0.85$ (3) and $P_1^{Si} > 0.95$ (4),
- $P_2^{Si} > 0.65$ (5) and $P_2^{Si} > 0.75$ (6),
- $E - p_z > 35\,GeV$ (7) and $E - p_z > 45\,GeV$ (8),
- $E - p_z < 65\,GeV$ (9),
- $E_1 > 8\,GeV$ (10) and $E_1 > 12\,GeV$ (11),
- $E_2 > 3\,GeV$ (12) and $E_2 > 2\,GeV$ (13),
- $\theta_2 < 2.75\,rad$ (14) and $\theta_2 < 3.14\,rad$ (15).

Limits of the H1 box, pipe and crack cuts have been varied (16).
The cut on the $Z_{vtx}$ was restricted to: $|Z_{vtx}| < 50\,cm$ (17).
The trigger efficency correction was varied (18).
The fraction of the $J/\psi$ events in the wrong-sign-e sample was varied

$$DIL = 50\% \quad \text{and} \quad J/\psi = 50\%\ (19).$$

The fraction of the inelastic component of the BH events was varied

$$BH_{inel} = 15\%\ (20),$$
$$BH_{inel} = 25\%\ (21).$$

Energy thresholds in the elasticily cuts has been variated $+30\ MeV$ (22) and $-30\ MeV$ (23).

The energy scale correction was implemented in the analysis (24).

The cut on the energy in the FPC was reduced to $E_{FPC} < 0.5\ GeV$ (25).

Figure 6.2 shows the effect of each systematic check in each $Q^2$ and $W$ bin, one can see that this effect is often largely smaller than 10%. The most significant contribution to $\sigma(Q^2)$ comes from systematics 5, 8 and 17 carring a relative sistematic uncertainty greater than 10% in the highest $Q^2$ bin, whereas for the $\sigma(W)$ measurement the most relevant contribution comes from bit 14, carring a relative sistematic uncertainty greater than 20%.

Contribution coming from each systematic check are summed in quadrature. Figure 6.3 shows the positive and negative contribution to the systematic uncertainty for each bin of $Q^2$ and $W$.

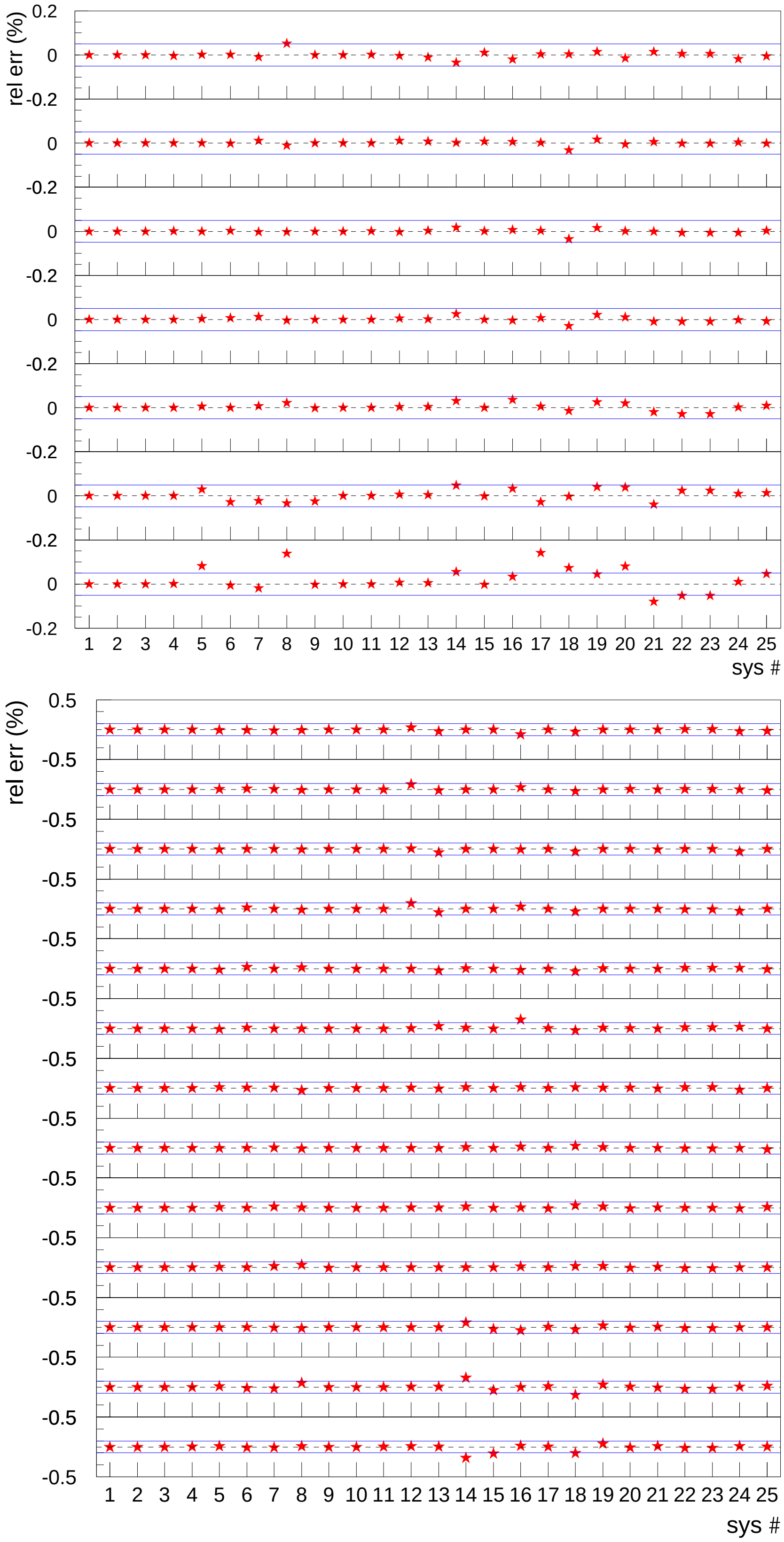


Figure 6.2: Relative systematic uncertainty for each check number in each $Q^2$ and $W$ bin in the $\gamma^*p$ cross section measurement.

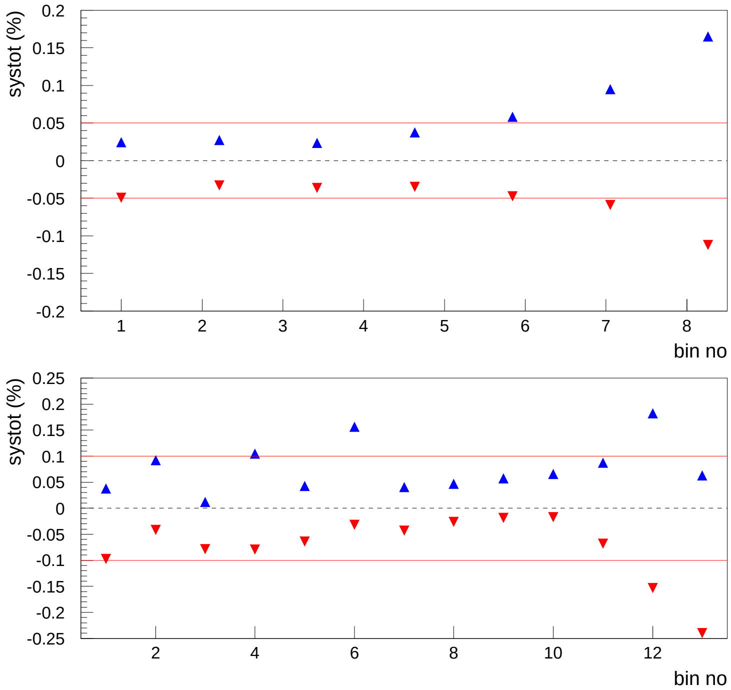


Figure 6.3: Positive (triangles) and negative (reversed triangles) contribution to the total sistematic uncertainty for each bin in $Q^2$ (upper) and $W$ (lower).

## 6.4 Results

The first set of results concerns the comparison with the DVCS cross section measurement [45] as a function of $Q^2$ and $W$ published by the ZEUS collaboration in the year 2003 using the whole $96-00$ $e^+p$ ($\mathcal{L} = 95.0\ pb^{-1}$) data sample in the kinematic region: $5 < Q^2 < 100\ GeV^2$ and $40 < W < 140\ GeV$. The comparison with this analysis has been performed in order to check the backward compatibility of the results. Figure 6.4 shows the $\gamma^* p$ cross sections as a function of $Q^2$ and $W$ in this restricted phase space. One can see that an excellent agreement with the published values was achieved. All small differences are understood and corresponds to an improvement of the understanding of the ZEUS detector response then in the past.

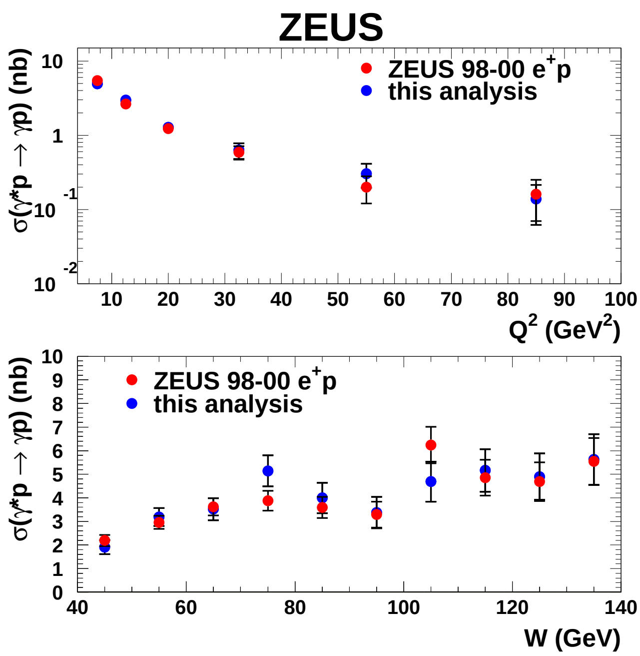


Figure 6.4: Comparison of cross section $\gamma^* p \to \gamma p$ measurements as a function of $Q^2$ (upper) and $W$ (lower) for the ZUES published analysis (red dots) and this work (blue dots). Only statistical uncertainties are quoted.

In this analysis the kinematic region has been extended to $3 < Q^2 < 100\ GeV^2$ and $40 < W < 170\ GeV$. This choice was made to enrich the results obtained by the collaborations ZEUS [45] and H1 [46, 47] adding a new bin at low $Q^2$ and three new bins at high $W$.

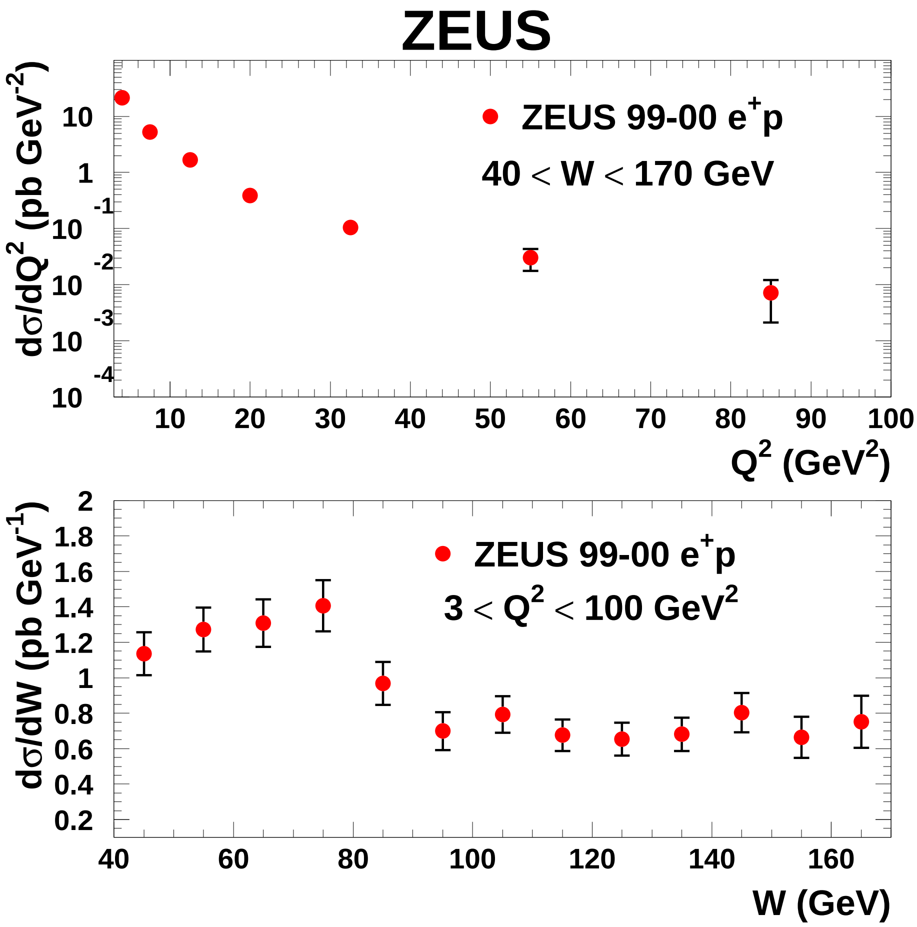


Figure 6.5: Cross section $ep \rightarrow e\gamma p$ measurements as a function of $Q^2$ (upper) and $W$ (lower). Only statistical uncertainties are quoted.

The DVCS $ep \to e\gamma p$ cross sections as a function of $Q^2$ and $W$ have been extracted. Results are reported in tables 6.1 and 6.2 respectively, and shown in fig. 6.5.

A measurement of the DVCS cross section $\gamma^* p \to \gamma p$ has been performed as a function of $Q^2$ for $\langle W \rangle = 107\,GeV$. The results are reported in tab. 6.3 and depicted in fig. 6.6(upper).

A fit of the form $Q^{-2n}$, applied to the DVCS cross section, gives $n = 1.56 \pm 0.08$ $(stat.)$ $(\chi^2/ndof = 0.61)$ which totally agrees with the published value [45] and is lower than the characteristic value for the exclusive vector-meson production $n \simeq 2$ [104, 107]. This is an indication that the DVCS cross section is less suppressed in $Q^2$ than the exclusive vector meson electroproduction.

The DVCS $\gamma^* p \to \gamma p$ cross section as a function of $W$ has been extracted for $\langle Q^2 \rangle = 5.9\,GeV^2$. The results are listed in tab. 6.4 and shown in fig. 6.6(lower).

A fit of the form $\sigma_{DVCS} \sim W^{\delta}$ was performed and it gives as result $\delta = 0.58 \pm 0.11$ $(\chi^2/ndof = 1.31)$ which agrees, within the uncertainties, with the previous published values [45] and it is entirely compatible with the one obtained for the $J/\psi$ photoproduction [48]. This $W$ energy dependence is directly linked to the gluon density inside the proton [108].

The $W$ dependence of $\gamma^* p \to \gamma p$ cross section in three $Q^2$ bins was presented in [45]. In this work, thanks to the enlargement of the kinematic phase space, we added a new set of measurements at lower $Q^2$. The results, shown in Fig.6.7, are compatible with no dependence of $\delta$ on $Q^2$ although also with the increase with $Q^2$ observed in exclusive production of light vector mesons [104, 109].

A further DVCS sample, containing 33 events, was produced, in order to measure the differential cross section as a function of $|t|$.

The systematic checks applied for the $d\sigma/d|t|$ corresponds to the following variations of the LPS data sample selection criteria

- distance of minimum approach to the beam pipe $> 0.1\ cm$,
- $(E + p_z)_{CAL} + 2E_p \cdot x_L < 1855\ GeV$,
- $0.09 < t < 0.5\ GeV^2$,
- $X^{LPS\,station} > -32\ cm$.

This led to a total systematic uncertainty contribution of 7% for each $|t|$ bin in the cross section.

Results are collected in tab. 6.5 and presented in fig. 6.8.

In order to extract the $b$ slope value from the $d\sigma/dt \sim e^{-b|t|}$ cross section an exponential fit was imposed to the data. It was found $b = 4.4 \pm$

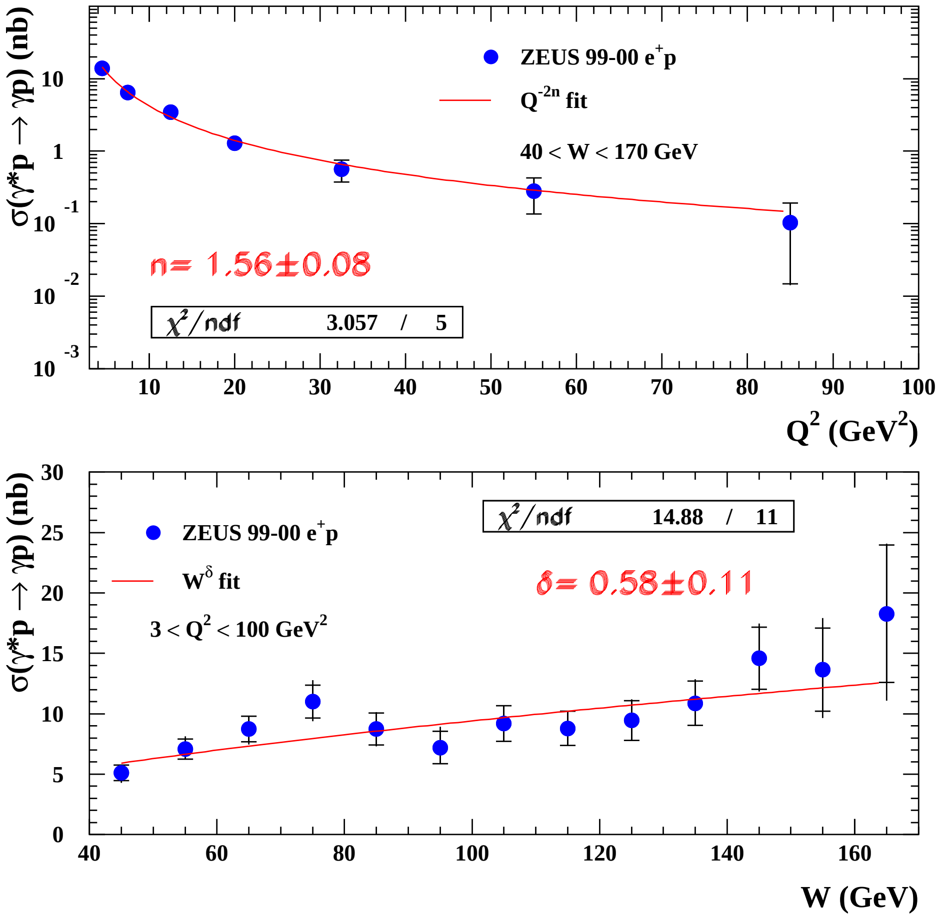


Figure 6.6: Cross section $\gamma^* p \to \gamma p$ measurements as a function of $Q^2$ (upper) and $W$ (lower). The inner error bars indicate statistical uncertainties while the external bars indicate the sum in quadrature of statistical and systematic uncertainties.

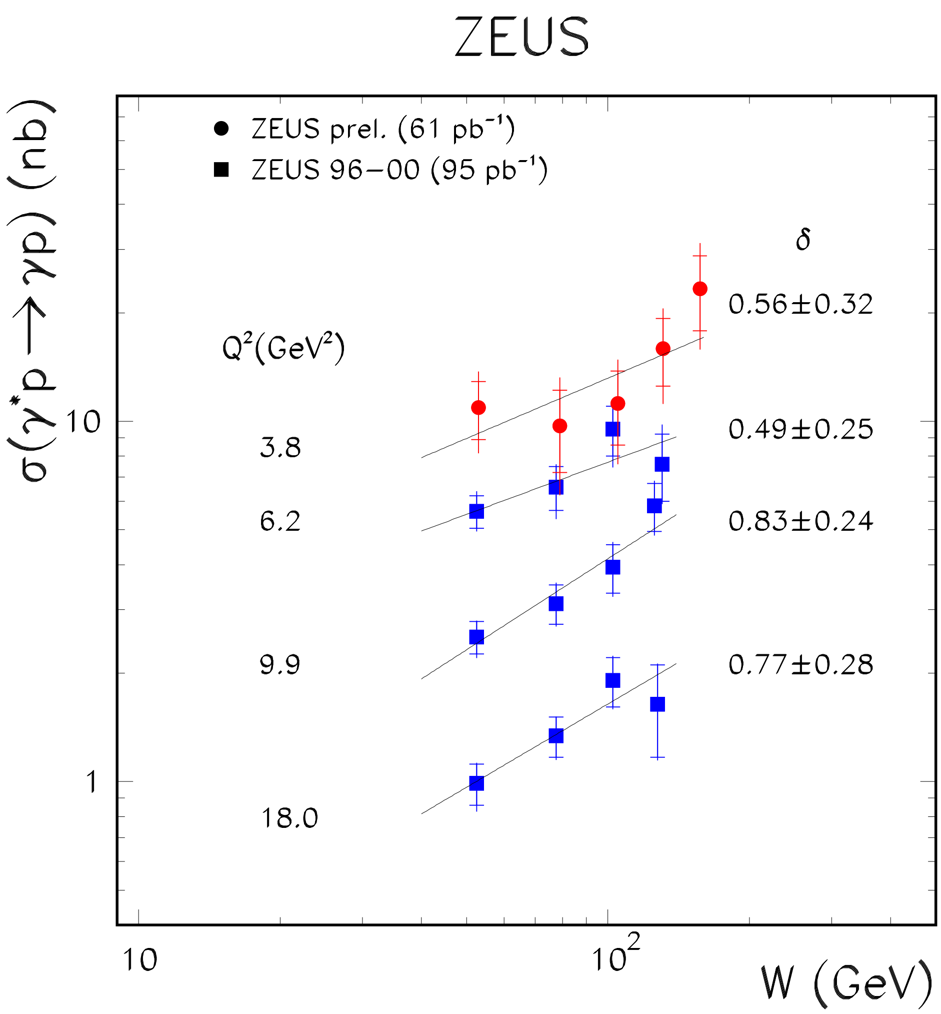


Figure 6.7: The DVCS cross section, $\sigma(\gamma^* p \to \gamma p)$, as a function of $W$ for four $Q^2$ values for $e^+p$. The higher $Q^2$ ranges are got from the published ZEUS data [45] (blue squares) and the lower $Q^2$ range is from this work (red circles). The solid line is the result of the fit $W^\delta$. The values of $\delta$ and their statistical uncertainties are given in the figure.

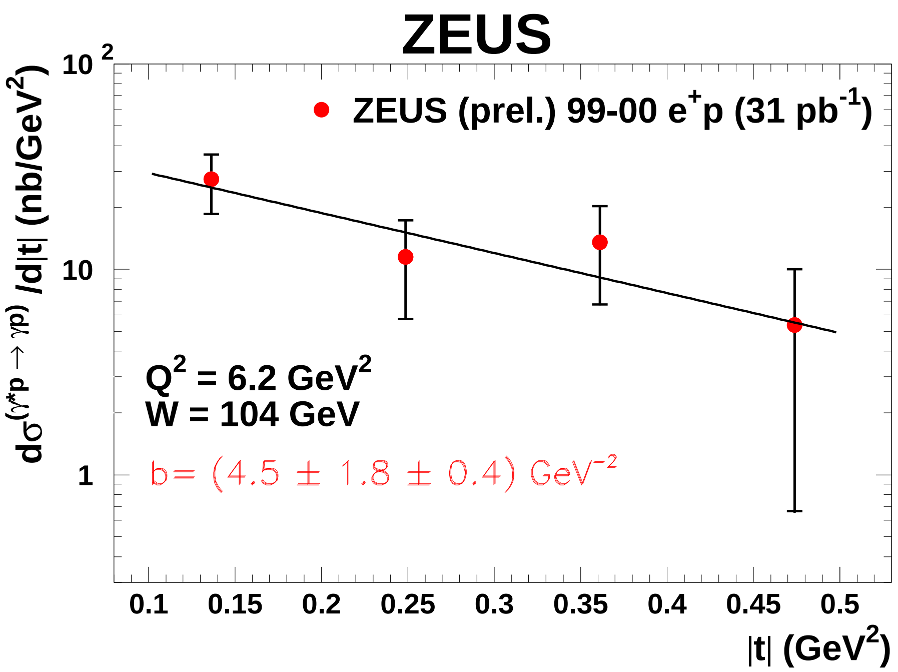


Figure 6.8: Differential cross section as a function of $t$. The inner error bars indicate statistical uncertainties while the external bars indicating the sum in quadrature of statistical and systematic uncertainties are not distinguishable. The $b$ slope value, obtained by a log-likelihood fit, is reported together with its statistical and systematic uncertainties.

2.3($stat.$) $GeV^{-2}$ with a $\chi^2/ndf = 0.23$. Due to the poor statistics in the LPS sample, the statistical uncertainty is really high.

In order to reduce the uncertainty, a new fit was performed to extract the value of the $b$ slope, using the unbinned log-likelihood maximisation method [106], which is more precise at low statistics. This technique is based on a comparison between a Monte Carlo sample, generated with a fixed $b_{gen}$ value, and the unbinned data sample.

Fig. 6.9 shows our log-likelihood distribution as a function of $b_{gen}$. Its maximum value, $Max[ln(L)] = 4.5\ GeV^{-2}$, is the result of the fit and the half of its standard deviation $\sigma_{logL}/2 = 1.8\ GeV^{-2}$ represents the statistical uncertainty, which results to be improved of 18% respectly to the the uncertainty coming from the $\chi^2$ minimisation fit.

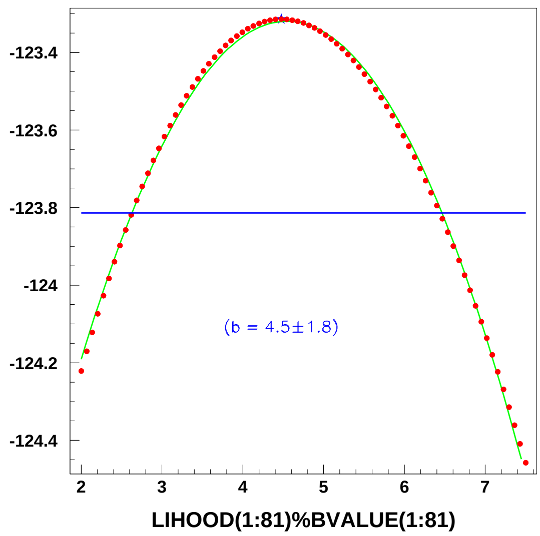


Figure 6.9: log-likelihood distribution as a function of $b_{gen}$ value. The maximum is at $b = 4.5\,GeV^{-2}$.

Additional systematic checks were performed to evaluate the systematic uncertainty on the $b$ slope value. These new systematics are relative to the log-likelihood fit procedure:

- variation of inelastic BH fraction in the MC mix used for the log-likelihood calculation,

- variation of histogram binning for the BH MC mix.

After this additional check, the total relative sistematic uncertainty on the $b$ slope measurement was estimated to be 8%.

In fig. 6.8 is displayed the result of log-likelihood fit, which indicates a slope value

$$b = 4.5 \pm 1.8(stat.) \pm 0.4(syst.).$$

It is compatible, within the uncertainties with the values measured by the H1 collaboration [47] where $t$ was calculated using the approximation that the variable $t$ is close to the negative square of the transverse momentum of the outgoing proton which can be computed form the vector sum of the transverse momenta of the final state photon $\vec{P}_{T_\gamma}$ and of the scattered electron $\vec{P}_{T_e}$ leading to the relation: $t \simeq -|\vec{P}_{T_\gamma} - \vec{P}_{T_e}|^2$.

## 6.5 Summary and conclusions

Deeply Virtual Compton Scattering was studied in this work within the phase space $3 < Q^2 < 100\ GeV^2$ and $40 < W < 170\ GeV$, using the ZEUS 1999-2000 $e^+p$ data sample corresponding to an integrated luminosity $\mathcal{L} = 61\ pb^{-1}$.

Thanks to a better understanding of the ZEUS detector responce, this analysis extends the kinematic region with respect to the published results.

A DVCS selection was performed looking at those events with two electromagnetic clusters, at least one track and without any hadronic activity. A large background contribution coming from Bethe-Heitler processes, which have the same topology as the DVCS events, was observed, estimated and subtracted to the sample.

The DVCS cross section as a function of $Q^2$ has been measured, showing a dependence $\sigma(Q^2) \sim Q^{-2n}$, $n = 1.56 \pm 0.08$ totally in agreement with the ZEUS published value [45] and lower than for the exclusive vector-meson porduction $n \simeq 2$ [104, 107].

The DVCS cross section has been also measured as a function of $W$. The $W$ energy dependence, relevant because it is directly linked to the gluon density inside the proton [108], showed a dependence $\sigma(W) \sim W^\delta$, $\delta = 0.58 \pm 0.11$ which agrees, within the uncertainties, with the ZEUS published values [45] and is compatible with the $J/\psi$ photoproduction [48].

The $W$ dependence of the DVCS cross section was published by the ZEUS collaboration in bins of $Q^2$ for the first time at ZEUS in 2003 [45] observing no dependence, although it was seen with the increase of $Q^2$ in exclusive production of light vector mesons [104, 109]. Thanks to the larger phase space in this analysis, a new measurement at $Q^2 = 3.8\ GeV^2$ has been added to the previous measurement and also for this new bin no dependence of the slope on $Q^2$ has been observed.

A subsample of the ZEUS 2000 $e^+$ data with the requirement of a proton detected with the Leading Proton Spectrometer, which comprise a total luminosity: $\mathcal{L} = 31\ pb^{-1}$, was used for the measurement of DVCS differential cross section as a function of $|t|$ extracted, for the first time, by a direct measurement of the scattered proton momentum.

A log-likelihood fit was performed, indicating a slope value

$$b = 4.5 \pm 1.8(stat.) \pm 0.4(syst.).$$

compatible, within the uncertainties, with the values measured by the H1 collaboration [47] where $t$ was calculated using the approximation that the variable $t \simeq |\vec{P}_{T_P}|$ is close to the negative square of the transverse momentum of the outgoing proton.

The results of this analysis have been declared as preliminary by the ZEUS collaboration, presented at the conference EPS07 [110] and are close to a complete publication.

After the HERA upgrade using polarized beams a very high data luminosity, $\mathcal{L} = 400\ pb^{-1}$, was collected by ZEUS. The analysis of those data could lead to a more precise DVCS cross section measurement. Morover, a measurement of the beam-spin asymmetry in a plolarized $ep$ scattering can allow the extraction of the immaginary part of the DVCS amplitude and then the Generalized Parton Distributions calculation. All these studies could contribute to the description of the Higg boson production in the diffractive channel which will be experimentally investigated as soon as the LHC accelerator will be in operation at the CERN laboratory in Geneve.

The analysis described in this thesis and the results presented are my personal contribute and my encouragement for future studies on DVCS with the HERAII data.

| $Q^2$ bin $(GeV^2)$ | $Q^2$ $(GeV^2)$ | $d\sigma/dQ^2$ $(pb/GeV^2)$ |
|---|---|---|
| $3-5$ | 4 | $21.31 \pm 1.94$ |
| $5-10$ | 7.5 | $5.24 \pm 0.33$ |
| $10-15$ | 12.5 | $1.67 \pm 0.14$ |
| $15-25$ | 20 | $0.39 \pm 0.05$ |
| $25-40$ | 32.5 | $0.10 \pm 0.03$ |
| $40-70$ | 55 | $0.03 \pm 0.01$ |
| $70-100$ | 85 | $0.007 \pm 0.005$ |

Table 6.1: Values of the $ep$ cross sections for the DVCS processes as a function of $Q^2$.

| $W$ bin $(GeV)$ | $W$ $(GeV)$ | $d\sigma/dW$ $(pb/GeV)$ |
|---|---|---|
| $40-50$ | 45 | $1.14 \pm 0.12$ |
| $50-60$ | 55 | $1.27 \pm 0.12$ |
| $60-70$ | 65 | $1.31 \pm 0.13$ |
| $70-80$ | 75 | $1.41 \pm 0.14$ |
| $80-90$ | 85 | $0.97 \pm 0.12$ |
| $90-100$ | 95 | $0.70 \pm 0.11$ |
| $100-110$ | 105 | $0.79 \pm 0.10$ |
| $110-120$ | 115 | $0.68 \pm 0.09$ |
| $120-130$ | 125 | $0.65 \pm 0.09$ |
| $130-140$ | 135 | $0.68 \pm 0.09$ |
| $140-150$ | 145 | $0.82 \pm 0.12$ |
| $150-160$ | 155 | $0.70 \pm 0.14$ |
| $160-170$ | 165 | $0.85 \pm 0.22$ |

Table 6.2: Values of the $ep$ cross sections for the DVCS processes as a function of $W$.

| $Q^2$ bin $(GeV^2)$ | $Q^2$ $(GeV^2)$ | $\sigma(Q^2)$ $(nb)$ |
|---|---|---|
| $3-5$ | 4 | $13.89 \pm 1.54^{+0.34}_{-0.69}$ |
| $5-10$ | 7.5 | $6.46 \pm 0.49^{+0.18}_{-0.21}$ |
| $10-15$ | 12.5 | $3.44 \pm 0.35^{+0.08}_{-0.12}$ |
| $15-25$ | 20 | $1.29 \pm 0.22^{+0.05}_{-0.04}$ |
| $25-40$ | 32.5 | $0.56 \pm 0.19^{+0.03}_{-0.03}$ |
| $40-70$ | 55 | $0.28 \pm 0.14^{+0.03}_{-0.02}$ |
| $70-100$ | 85 | $0.10 \pm 0.09^{+0.02}_{-0.01}$ |

Table 6.3: Values of the $\gamma^* p$ cross sections for the DVCS processes as a function of $Q^2$. Values are quoted at the centre of each $Q^2$ bin and for the average $W$ value of the whole sample, $W = 107\ GeV$.

| $W$ bin ($GeV$) | $W$ ($GeV$) | $\sigma(W)$ ($nb$) |
|---|---|---|
| $40-50$ | 45 | $5.11 \pm 0.65^{+0.19}_{-0.50}$ |
| $50-60$ | 55 | $7.09 \pm 0.82^{+0.65}_{-0.30}$ |
| $60-70$ | 65 | $8.74 \pm 1.07^{+0.10}_{-0.68}$ |
| $70-80$ | 75 | $11.00 \pm 1.36^{+1.15}_{-0.87}$ |
| $80-90$ | 85 | $8.74 \pm 1.33^{+0.38}_{-0.56}$ |
| $90-100$ | 95 | $7.19 \pm 1.34^{+1.12}_{-0.23}$ |
| $100-110$ | 105 | $9.20 \pm 1.47^{+0.38}_{-0.39}$ |
| $110-120$ | 115 | $8.79 \pm 1.41^{+0.41}_{-0.23}$ |
| $120-130$ | 125 | $9.45 \pm 1.64^{+0.54}_{-0.17}$ |
| $130-140$ | 135 | $10.87 \pm 1.84^{+0.71}_{-0.18}$ |
| $140-150$ | 145 | $14.60 \pm 2.58^{+1.28}_{-0.99}$ |
| $150-160$ | 155 | $13.66 \pm 3.44^{+2.49}_{-2.09}$ |
| $160-170$ | 165 | $18.27 \pm 5.69^{+1.16}_{-4.38}$ |

Table 6.4: Values of the $\gamma^* p$ cross sections for the DVCS processes as a function of $W$. Values are quoted at the centre of each $W$ bin and for the average $Q^2$ value of the whole sample, $Q^2 = 5.9\ GeV^2$.

| $\|t\|$ bin ($GeV^2$) | $\|t\|$ ($GeV^2$) | $d\sigma/d\|t\|$ ($nb/GeV^2$) |
|---|---|---|
| $0.08-0.19$ | 0.14 | $27.43 \pm 8.80\ (stat.) \pm 1.9\ (sys.)$ |
| $0.19-0.31$ | 0.25 | $11.53 \pm 5.79\ (stat.) \pm 0.8\ (sys.)$ |
| $0.31-0.42$ | 0.36 | $13.53 \pm 6.77\ (stat.) \pm 0.9\ (sys.)$ |
| $0.42-0.53$ | 0.47 | $5.35 \pm 4.68\ (stat.) \pm 0.4\ (sys.)$ |

Table 6.5: Values of the $\gamma^* p$ cross sections for the DVCS processes as a function of $|t|$. Values are quoted at the centre of each $|t|$ bin and for the average $Q^2$, $W$ values of the whole sample, $Q^2 = 5.9\ GeV^2$ and $W = 107\ GeV$ respectively.

# Chapter 7

# A new theoretical model for DVCS amplitude

A new factorized Regge-pole model [1] for deeply virtual Compton scattering is described in this chapter.

The use of an effective logarithmic Regge-Pomeron trajectory allows the description of both *soft* (*small* $|t|$) and *hard* (*large* $|t|$) dynamics. The model contains explicitly the photoproduction and the DIS limits and fits are performed the existing HERA data on deeply virtual Compton scattering.

## 7.1 An introduction to the model

The $Q^2$ evolution of the DVCS amplitude has been studied in several papers, mainly in the context of perturbative quantum chromodynamics (QCD) [31, 34, 42, 111] and recently in [112].

The $t$ dependence in many papers was introduced by a simple factorized exponential in $t$, which however differs from the Regge pole theory. Since the electron-proton scattering at HERA is dominated by a single photon exchange, the calculation of the DVCS scattering amplitude reduces to that of the $\gamma^* p \to \gamma p$ amplitude, which at high energies, in the Regge pole approach, is dominated by the exchange of positive-signature Reggeons, associated with the Pomeron and the $f$-trajectories [2]. This DVCS amplitude is shown in fig. 7.1b in a Regge-factorized form. In the figure $q_{1,2}$ are the four-momenta of the incoming and outgoing photons, $p_{1,2}$ are the four-momenta of the incoming and outgoing protons, moreover $r$ is the four-momentum of the Reggeon exchanged in the $t$ channel, $r^2 = t = (q_1 - q_2)^2$ and $s = W^2 = (q_1 + p_1)^2$ is the squared centre-of-mass energy of the incoming system.

Unless specified (as in the deep inelastic scattering (DIS) limit, discussed

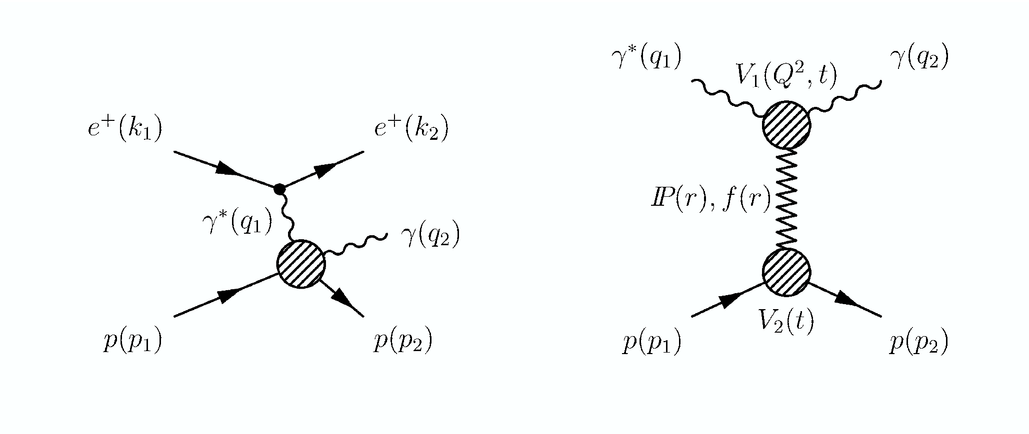


Figure 7.1: a) Diagram of a DVCS event at HERA; b) DVCS amplitude in a Regge-factorized form.

in Sec. 7.2.1), $q_2^2 = 0$, and hence, for brevity, $q_1^2 = -Q^2$. In the upper vertex $V_1$ in fig. 7.1b, a virtual photon with four-momentum $q_1$, and a Reggeon (e.g. Pomeron) with four-momentum $r$, enter and a real photon, with four-momentum $q_2 = q_1 + r$ appears in the final state as an outgoing particle. The vertex $V_1$ depends on all the possible invariants constructed with the above four-momenta, $V_1[q_1^2, r^2, q_1\cdot r]$, where $r^2 = t \leq 0$, $q_1^2 = -Q^2 \leq 0$.

The three invariants are not independent since the mass-shell condition for the outgoing photon, $q_2^2 = (q_1 + r)^2 = 0$, provides the relation.

$$q^2\cdot r = \frac{-q_1^2 - r^2}{2} = \frac{Q^2 - t}{2}. \tag{7.1}$$

Hence, the vertex can be considered as a function of the invariants $[Q^2, q_1\cdot r]$ or $[t,\, q_1\cdot r]$.

This does not mean that the variables cannot appear separately but it could also happen that $q_1\cdot r$ become a scaling variable, and consequently the vertex will finally depend on $q_1\cdot r$ only. It depends on the dynamics of the process and, for the moment, we prefer to keep $t$, apart from $Q^2$, as the second independent variable.

Electroproduction of a vector meson gives another example since in this case $(q_1 + r)^2 = M_V^2$, and the variable $q_1\cdot r$ becomes

$$q_1\cdot r = \frac{M_V^2 - q_1^2 - r^2}{2} = \frac{M_V^2 + Q^2 - t}{2}. \tag{7.2}$$

The interplay of the $Q^2$- and $t$-dependence in the DVCS amplitude was recently discussed in [113], where the existence of a new, universal variable $z$

was suggested. The basic idea is that $Q^2$ and $t$, both having the meaning of a squared mass of a virtual particle (photon or Reggeon), should be treated on the same footing, by means a new variable, defined as

$$z = q_1^2 + t = -Q^2 + t \tag{7.3}$$

in the same way as the vector meson mass squared is added to the squared photon virtuality, giving $\tilde{Q}^2 = Q^2 + M_V^2$ in the case of vector meson electroproduction [114, 115].

In the model presented in this work the $Q^2$- and $t$-dependences were determined by the $\gamma^* IP\gamma$ vertex. It is suggested the use of the new variable defined in 7.3 with its possible generalization to vector meson electroproduction,

$$z = t - (Q^2 + M_V^2) = t - \tilde{Q}^2, \tag{7.4}$$

or virtual photon (lepton pair) electroproduction,

$$z = t - (Q_1^2 + Q_2^2), \tag{7.5}$$

where $Q_2^2 = -q_2^2$. However, differently from [113], here it is introduced the new variable only in the upper, $\gamma^* IP\gamma$ vertex, to which the photons couple.

In the next Section the model will be introduced. Its viability is supported by the correct photoproduction- ($Q^2 = 0$) and DIS- ($Q^2 > 0$ and $t \to 0$) limits, demonstrated in Sec. 7.2.1.

## 7.2 The model

According to fig. 7.1b, the DVCS amplitude can be written as

$$A(s,t,Q^2)_{\gamma^* p \to \gamma p} = -A_0 V_1(t,Q^2) V_2(t) (-is/s_0)^{\alpha(t)}, \tag{7.6}$$

where $A_0$ is a normalization factor, $V_1(t, Q2)$ is the $\gamma^* IP\gamma$ vertex, $V_2(t)$ is the $pIPp$ vertex and $\alpha(t)$ is the exchanged Pomeron trajectory, which we assume in a logarithmic form

$$\alpha(t) = \alpha(0) - \alpha_1 \ln(1 - \alpha_2 t). \tag{7.7}$$

Such a trajectory is nearly linear for small $|t|$, thus reproducing the forward cone of the differential cross section, while its logarithmic asymptotics provides for the large-angle scaling behavior [116, 117], typical of hard collisions at small distances, with power-law fall-off in $|t|$, obeying quark counting rules [116, 118, 119]. Here we are referring to the dominant Pomeron contribution plus a secondary trajectory, e.g. the $f$-Reggeon. Although we are aware of the importance of this subleading contribution at HERA energies, nevertheless we cannot afford the duplication of the number of free parameters, therefore we include it effectively by rescaling the parameters. Ultimately, the Pomeron and the $f$-Reggeon have the same functional form, differing only by the values of their parameters.

Furthermore, the Pomeron [120] itself is unlikely to be a single term, so instead of including several Regge terms with many free parameters, it may be reasonable to comprise them in a single term, called *effective Reggeon* or *effective Pomeron*, depending on the kinematical region of interest. Although the parameters of this effective Reggeon (Pomeron) (e.g. its intercept and slope) can be close to the *true* one (whose form is at best a convention), for the above reason they never should be taken as granted.

For convenience, and following the arguments based on duality (see Ref. [121] and references therein), the $t$ dependence of the $pIPp$ vertex is introduced via the $\alpha(t)$ trajectory: $V_2(t) = e^{b\alpha(t)}$ where $b$ is a parameter. A generalization of this concept will be applied also to the upper $\gamma^* IP\gamma$ vertex by introducing the *trajectory*

$$\beta(z) = \alpha_0 - \alpha_1 \ln(1 - \alpha_2(z)), \tag{7.8}$$

where the value of the parameter $\alpha_2$ may be different in $\alpha(t)$ and $\beta(z)$ (a relevant check will be possible when more data will be available). Hence the scattering amplitude 7.6, with the correct signature, becomes

$$A(s,t,Q^2)_{\gamma^* p\to\gamma p} = -A_0 e^{b\alpha(t)} e^{b\beta(z)} (-is/s_0)^{\alpha t} = -A_0 e^{(b+L)\alpha(t)+b\beta(z)}, \tag{7.9}$$

where $L \equiv \ln(-is/s_0)$.

The model contains a limited number of free parameters. Moreover, most of them can be estimated a priori. The product $\alpha_1\alpha_2$ is just the forward slope $\alpha'$ of the Reggeon ($\approx 0.2GeV^{-2}$ for the Pomeron, but much higher for $f$ and/or for an effective Reggeon)[6]. The value of $\alpha_1$ can be estimated from the large-angle quark counting rules [116, 118, 119]. For large $t$ ($|t| \gg 1GeV^2$) the amplitude goes roughly (a detailed treatment of this point can be found in Refs. [116, 117]) like $\sim e^{-\alpha_1 \ln(-t)} = (-t)^{\alpha_1}$ , where the power $\alpha_1$ is related to the number of quarks in a collision [116, 118, 119], e.g. their number minus one. Various versions of the counting rules suggest different combinatorics

[6]As emphasized in a number of papers, e.g. in Ref. [122], the wide-spread prejudice of the *flatness* of the Pomeron in electroproduction is wrong for at least two reasons: one is that it was deduced by fitting data to a particular effective Reggeon and the second is that the Pomeron is universal, and its nonzero slope is well known from hadronic reactions.

giving slightly different values for this power. In this work it was set: $\alpha_1 = 1$, and hence $\alpha_2 = \alpha'$. For the intercept of our effective Reggeon, dominated by the Pomeron, it was set $\alpha(0) = 1.25$ as an average over the $soft + hard$ Pomerons [7]. The above values of the parameters should not be taken as granted, they should be considered as starting values in the fitting procedure presented in Sec. 7.3.

From Eq. 7.9 the slope of the forward cone is

$$B(s, Q^2, t) = \frac{d}{dt} \ln |A|^2 = 2[b + \ln(\frac{s}{s_0})] \frac{\alpha'}{1 - \alpha_2 t} + 2b \frac{\alpha'}{1 - \alpha_2 z}, \tag{7.10}$$

which, in the forward limit, $t = 0$ reduces to

$$B(s, Q^2) = 2[b + \ln(\frac{s}{s_0})]\alpha' + 2b \frac{\alpha'}{1 - \alpha_2 Q^2}. \tag{7.11}$$

Thus, the slope shows shrinkage in $s$ and antishrinkage in $Q^2$.

### 7.2.1 Photoproduction and DIS limits

In the $Q^2 \to 0$ limit the Eq. 7.9 becomes

$$A(s, t) = -A_0 e^{2b\alpha(t)} (-is/s_0)^{\alpha(t)} \tag{7.12}$$

where we recognize a typical Regge-behaved photoproduction (or, for $Q^2 \to m_H^2$, on-shell hadronic (H)) amplitude. The related deep inelastic scattering structure function is recovered by setting $Q_1^2 = Q_2^2 = Q^2$ and $t = 0$, to get a typical elastic virtual forward Compton scattering amplitude

$$A(s, Q^2) = -A_0 e^{b(\alpha(0) - \alpha_1 \ln(1 + \alpha_2 Q^2))} e^{(b + \ln(-is/s_0))\alpha(0)} \propto -(1 + \alpha_2 Q^2)^{-\alpha_1} (-is/s_0)^{\alpha(0)}. \tag{7.13}$$

In the Bjorken limit, when both $s$ and $Q^2$ are large and $t = 0$ (with $x \approx Q^2/s$ valid for large $s$), the structure function is given by

$$F_2(s, Q^2) \approx \frac{(1 - x) Q^2}{\pi \alpha_e} \mathcal{I} A(s, Q^2)/s, \tag{7.14}$$

[7] This is an obvious simplification and we are fully aware of the variety of alternatives for the energy dependences, e.g. that of a dipole Pomeron, as in Ref. [121], a $soft$ plus a *hard* one, as e.g. in Ref. [31]. Ultimately, from QCDs BFKL equation [120] an infinite number of Pomeron singularities follows unless simplifications are used. For the present study in term of the new $z$ variable the simplest *supercritical* Pomeron [31] with an effective intercept is suitable.

| parameter | $\sigma_{DVCS}$ vs $Q^2$ | $\sigma_{DVCS}$ vs $t$ | $\sigma_{DVCS}$ vs $W$ |
|---|---|---|---|
| $\lvert A_0\rvert^2$ | $0.08 \pm 0.01$ | $0.11 \pm 0.24$ | $0.06 \pm 0.01$ |
| $b$ | $0.93 \pm 0.05$ | $1.04 \pm 0.91$ | $1.08 \pm 0.10$ |
| $\chi^2/ndof$ | 0.57 | 0.15 | 1.15 |

Table 7.1: The values of the fitted parameters quoted in Eq. 7.9.

where $\alpha_e$ is the electromagnetic coupling constant and the normalization is $\sigma_t(s) = \frac{4\pi}{s}\mathcal{I}A(s,Q^2)$. The resulting structure function has the correct (required by gauge invariance) $Q^2 \to 0$ limit and approximate scaling (in $x$) behavior for large enough $s$ and $Q^2$.

It should be noted, however, that the Regge behavior has a limited range of validity in $Q^2$. The smooth transition to DGLAP evolution was studied in Ref. [123], while a relevant explicit model was developed in Ref. [124].

## 7.3 Fits to HERA data

A standard procedure for the fit to the HERA data on DVCS [45, 46, 47] based on Eq. 7.9 has been adopted. A detailed analysis of the data would require a sum of a Pomeron plus an $f$-Reggeon contribution

$$A = A^P + A^f \tag{7.15}$$

To avoid the introduction of too many parameters, given the limited number of experimental data points, we use a single Reggeon term, as already discussed in Sec. 7.2, which can be treated as an effective Reggeon. The parameters $\alpha(0)$, $\alpha_1$ and $\alpha'$ have been fixed to 1.25, 1.0 and 0.38 $GeV^2$ respectively and the values of the fitted parameters $A_0$ and $b$, described in Eq. 7.9 are listed in Table 7.1. The value of $\alpha'$ has been determined in an exploratory fit with this parameter left free to vary between 0.2 and 0.4 $GeV^{-2}$.

The ZEUS measurements have been rescaled to the $W$ and $Q^2$ values of the H1 measurements. The mean value of $|t|$ has been fixed to 0.17 $GeV^2$ according with the H1 measurements of the differential cross-section in the range (0.1 - 0.8) $GeV^2$ for H1 [47] taking into account the value 6.02 $GeV^{-2}$ for the slope $B$ as determined by the experiment.

The results of the fits to the HERA data on DVCS are shown in fig. 7.2. The cross section $\sigma(\gamma^* p \to \gamma p)$ as a function of $Q^2$ and $W = \sqrt{s}$ are presented respectively in fig. 7.2a and fig. 7.2b. The differential cross section $d\sigma(\gamma^* p \to \gamma p)/dt$, given by

$$\frac{d\sigma}{dt}(s,t,Q^2) = \frac{\pi}{s^2}|A(s,t,Q^2)|^2, \tag{7.16}$$

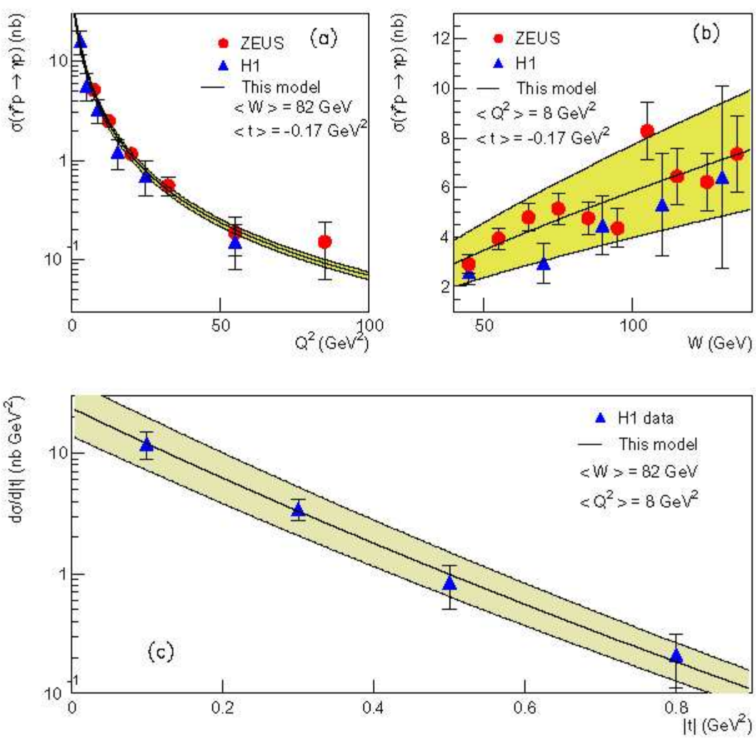


Figure 7.2: The $\gamma^* p \to \gamma p$ cross section as a function of $Q^2$ (a), of $W$ (b) $t$ (c) measured by H1 and ZEUS experiments. The ZEUS measurements have been rescaled to the $W$ and $Q^2$ H1 values. The lines show the results of the fits obtained from Eq. 7.16 to the data.

is presented in fig. 7.2c.

Although the present HERA data on DVCS are well within the $soft$ region, the model potentially is applicable for much higher values of $|t|$, dominate by hard scattering.

The behavior of $F_2(s, Q^2)$ at small $x$ and moderate $Q^2$ with the parameters fitted above to the DVCS data, is shown in fig. 7.3

Finally, Fig. 7.4 shows antishrinkage in $Q^2$ and shrinkage in $W$ of the forward cone, according to Eqs. 7.10 and 7.11. The curves are compared with the H1 experimental results.

## 7.4 Conclusions

The model presented here has been published in [1] during the second year of my PhD studies. The fits to the HERA data do not include the results

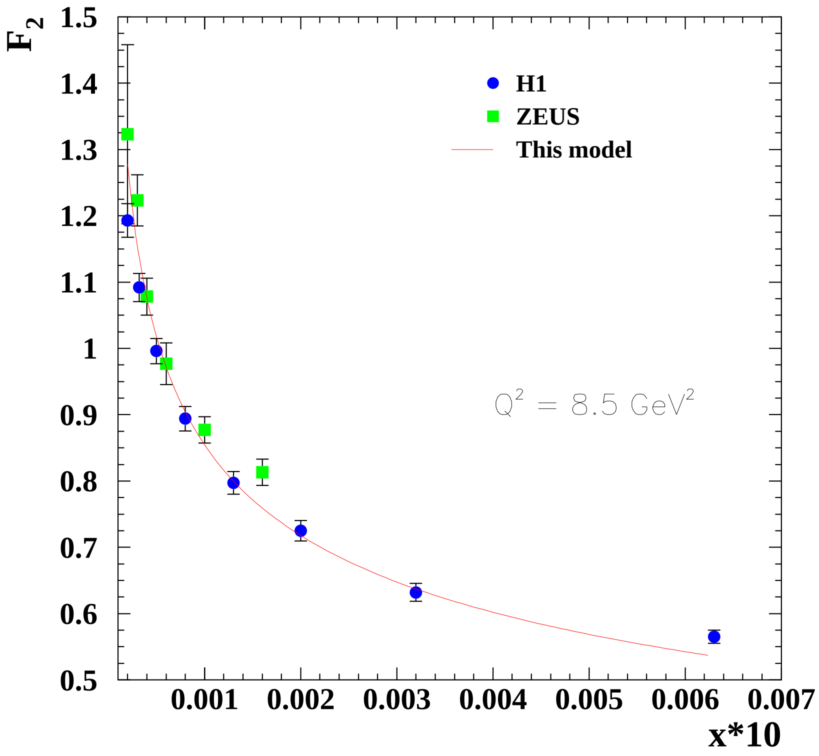


Figure 7.3: The behavior of the DIS structure functions, Eq. 7.14, shown together with the H1 and ZEUS data.

collected in this thesis and presented in Sec. 6.4. A new paper with the evolution of the model and new fits including all recent experimental results is in progress. Thanks to the higher statistics including new measurements, the model can be enriched by accounting for the Pomeron(s) and $f$-Reggeon contributions separately as well as by using expressions for Regge trajectories which take exactly into account analyticity and unitarity.

This model can be used to study various extreme regimes of the scattering amplitude in all the three variables it depends on. For that purpose, however, the transition from Regge behavior to QCD evolution at large $Q^2$ should be accounted for. A formula interpolating between the two regimes (Regge pole and asymptotic QCD evolution) was proposed [124] for $t = 0$ only. Its generalization to non zero $t$ value is possible by applying the ideas and the model presented in this paper. The applicability of the model in both soft and hard domains can be used to learn about the transition between perturbative (QCD) and non-perturbative (Regge poles) dynamics.

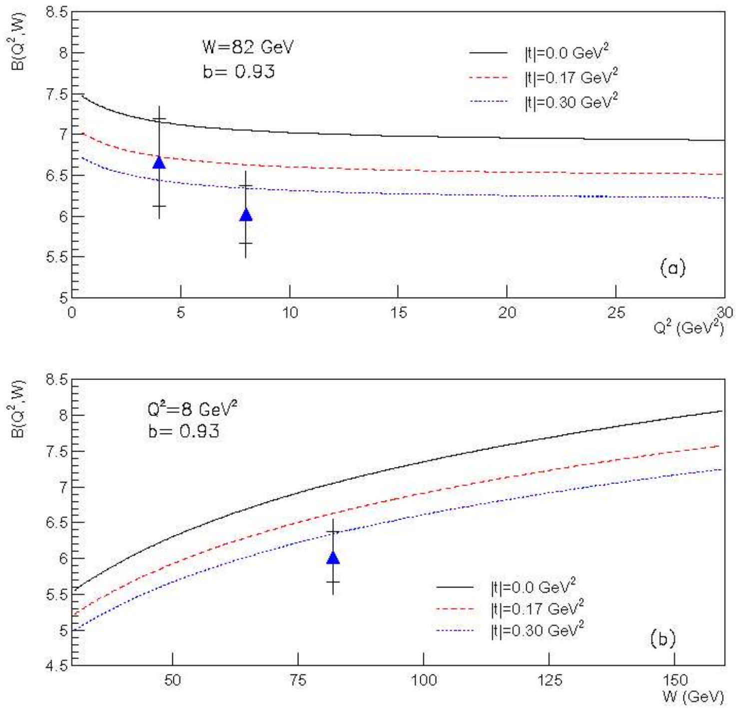


Figure 7.4: The $Q^2$- and $s$ dependence of the local slope described in Eq. 7.10 (dotted and dashed line) and Eq. 7.11 (solid line). The triangles show the experimental measurements of H1.

Independently of the pragmatic use of this model, it can be regarded also as an explicit realization of the corresponding principle [125] of exclusive-inclusive connection in various kinematical limits.

Last but not least, the simple and feasible model of DVCS presented in this paper can be used to study general parton distributions (GPD). As emphasized in Ref. [126], in the first approximation, the imaginary part of the DVCS amplitude is equal to a GPD. The presence of the Regge phase in our model can be used for restoring the correct phase of the amplitude, for which the interference experiments (with Bethe-Heitler radiation) are designed.

# Bibliography


[1] M. Capua, S. Fazio, R. Fiore, L. Jenkovszky, F Paccanoni, Ph. Lett. B 645, 161-166 (2007).

[2] P. D. B. Collins, *An Introduction to Regge Theory and High Energy Physics*, Cambridge University Press, Cambridge (1977).

[3] G. Ingelman and P. E. Schlein, Phys. Lett. B 152, 256 (1985).

[4] L.N. Hand, Phys. Rev. 129, 1834 (1963).

[5] E.D. Bloom et al., Phys. Rev. Lett. 23, 930 (1969);
M. Breidenbach et al., Phys. Rev. Lett. 23, 935 (1969).

[6] H1 Coll., S. Aid et al., Nucl. Phys. B 470, 3 (1996);
ZEUS Coll., M. Derrick et al., Z. Phys. C 72, 399 (1996).

[7] J.D. Bjorken, Phys. Rev. 163, 1767 (1967);
R.P. Feynman, Phys. Rev. Lett. 23, 1415 (1969).

[8] M. Gell-Mann, Phys. Lett. 8, 214 (1964);
G. Zweig. CERN-TH-412.

[9] T. Eichten et al., Phys. Lett. B 46, 274 (1973).

[10] J. C. Collins, D. E. Soper and G. Sterman, Nucl. Phys. B 261, 104 (1985).

[11] A. Courau and P.Kessler, Phys. Rev. D 46, 117 (1992).

[12] G. Alberi and G. Goggi, Phys. Rep. 74, 1 (1981).

[13] K. Goulianos, Phys. Rep. 101, 169 (1983).

[14] ZEUS Coll., M. Derrick et al., Phys. Lett. B 315, 481 (1993).

[15] G.F. Chew and S.C. Frautschi, Phys. Rev. Lett. 8, 41 (1962).

[16] V.N. Gribov, Sov. Phys. JETP 14, 478 (1962).

[17] I.Y. Pomeranchuk, Sov. Phys. JETP 7, 499 (1985).

[18] H1 Coll., C. Adloff et al., Z. Phys. C 74, 221 (1997);
H1 Coll., T. Ahmed et al., Nucl. Phys. B 429, 477 (1994).

[19] A. Donnachie and P.V. Landshff, Phys. Lett. B 296, 227 (1992).

[20] X. Ji, Phys. Rev. D 55, 7114 (1997).

[21] A. Belitsky, A. Freund and D. Muller, Nucl. Phys. B 574, 347 (2000).

[22] A.V. Radyushkin, Phys. Lett. B 380, 417 (1996).

[23] A.V. Radyushkin, Phys. Rev. D 56, 5524 (1997).

[24] M. Guidal, Nucl. Phys. A 699, 200 (2002).

[25] M. Diehl, Phys. Rept. 388, 41 (2003).

[26] A. Freund, Phys. Lett. B 472, 412 (2000).

[27] A. Freund, Phys. Lett. B 472, 412 (2000).

[28] J.C. Collins and A. Freund, Phys. Rev. D 59, 74009 (1999).

[29] A.V. Belitsky, D. Muller and A. Kirchner, Nucl. Phys. B 629, 323 (2002).

[30] M. Diehl et al., Phys. Lett. B 411, 193 (1997).

[31] A. Donnachie and H.G. Dosch, Phys. Lett. B 502, 74 (2001);

[32] L. Frankfurt, A. Freund and M. Strikman, Phys. Lett. B 460, 417 (1999).

[33] L.L. Frankfurt, A. Freund and M. Strikman, Phys. Rev. D 58, 114001 (1998). Erratum ibid.D 59 119901 (1999).

[34] A. Freund, M. McDermott and M. Strikman, Phys. Rev. D 67, 036001 (2003).

[35] A. Freund and M. McDermott, Eur. Phys. J. C 23, 651 (2002); A. Freund and M. McDermott, Phys. Rev. D 65, 091901 (2002).

[36] N.N. Nikolaev and B.G. Zakharov, Z. Phys. C 49, 607 (1991).

[37] A.H. Mueller and B. Patel, Nucl. Phys. B 425, 471 (1994).

[38] K. Golec-Biernat and M. Wüsthoff, Phys. Rev. D 59, 014017 (1999).
J.R. Forshaw, G. Kerley and G. Shaw, Nucl. Phys. A 675, 80c (2000).

[39] J.R. Forshaw, G. Kerley and G. Shaw, Phys. Rev. D 60, 074012 (1999).

[40] M. McDermott, R. Sandapen and G. Shaw, Eur. Phys. J. C 22, 655 (2002).

[41] M. McDermott et al., Eur. Phys. J. C 16, 641 (2000).

[42] L. Favart and M. Machado, Eur. Phys. J. C 29, 365 (2003).

[43] L. Favart and M. Machado, *QCD evolution and skewedness effects in color dipole description of DVCS*, Eur. Phys. J. C 34, 429 (2004).

[44] K. Golec-Biernat and M. Wüsthoff, Phys. Rev. D 60, 114023 (1999).

[45] ZEUS Coll., *Measurement of Deeply Virtual Compton Scattering at HERA*, Phys. Lett. B573 46-62 (2003).

[46] H1 Coll., *Measurement of Deeply Virtual Compton Scattering at HERA*, Phys. Lett. B517 47-58 (2001).

[47] H1 Coll., *Deeply Virtual Compton Scattering at HERA*, Eur. Phys. J. C 44, 1-11 (2005);
H1 Coll., *Measurement of Deeply Virtual Compton Scattering and its $t$-dependence at HERA*, DESY 07-142, September 2007.

[48] ZEUS Coll., S. Chekanov et al., Eur. Phys. J. C 24, 345 (2002).

[49] A. V. Belitsky, D. Mueller, L. Niedermeier and A. Schafer, Nucl. Phys. B 593, 289 (2001).

[50] HERMESS Coll., A. Airapetian et al., *Measurement of the Beam-Spin Azimuthal Asymmetry associated with Deeply-Virtual Compton Scattering*, Phys. Rev. Lett. 87, 182002 (2001);
HERMESS Coll., A. Airapetian et al., *The Beam-Charge Azimuthal Asymmetry and Deeply Virtual Compton Scattering* Phys. Rev. D 75, 011103(R) (2007).

[51] CLAS Collab., S. Stepanyan et al., Phys. Rev. Lett. 87, 182002 (2001).

[52] M. V. Polyakov and C. Weiss, Phys. Rev. D 60, 114017 (1999).

[53] *HERA: A Proposal for a Large Electron Proton Colliding Beam Facility at DESY*, DESY-HERA-81/10, Hamburg (1981).

[54] ZEUS Coll., U. Holm (ed.), *The ZEUS Detector. Status Report* (unpublished), DESY (1993), available on http://www-zeus.desy.de/bluebook/bluebook.html.

[55] N. Harnew et al., Nucl. Inst. Meth. A 279, 290 (1989);
B. Foster et al., Nucl. Phys. Proc. Suppl. B 32, 181 (1993);
B. Foster et al., Nucl. Inst. Meth. A 338, 254 (1994).

[56] A. Bamberger et al., Nucl. Inst. Meth. A 401, 63 (1997).

[57] M. Derrick et al., Nucl. Inst. Meth. A 309, 77 (1991);
A. Andresen et al., Nucl. Inst. Meth. A 309, 101 (1991);
A. Caldwell et al., Nucl. Inst. Meth. A 321, 356 (1992);
A. Bernstein et al., Nucl. Inst. Meth. A 336, 23 (1993).

[58] ZEUS Coll., FPC group, A. Bamberger et al., Nucl. Inst. Meth. A 450, 235 (2000).

[59] A. Bamberger et al., Nucl. Inst. Meth. A 382, 419 (1996);
S. Magill and S. Chekanov, Proc. of the IX International Conference on Calorimetry in High Energy Physics, B. Aubert et al. (eds.), p. 625, Annecy, France (2000).

[60] A. Dwurazny et al., Nucl. Inst. Meth. A 277, 176 (1989).

[61] M. Bobrowski et al., Nucl. Inst. Meth. A 323, 309 (1992).

[62] B. Bednarek et al., Nucl. Inst. Meth. A 348, 228 (1994).

[63] ZEUS Coll., J. Breitweg et al., Z. Phys. C 75, 421 (1997).

[64] ZEUS Coll., M. Derrick et al., Z. Phys. C 73, 253 (1997).

[65] ZEUS Coll., FNC group, S. Bhadra et al., Nucl. Inst. Meth. A 394, 121 (1997).

[66] B. Surrow, *Measurement of the Proton Structure Function $F_2$ at Low $Q^2$ and Very Low $x$ with the ZEUS Beam Pipe Calorimeter at HERA.* Ph.D. Thesis, Univ. of Hamburg, Report DESY-THESIS-1998-004, 1998.

[67] J. Andruszkow et al., Preprint DESY-92-066, DESY, 1992;
ZEUS Coll., M. Derrick et al., Z. Phys. C 63, 391 (1994);
J. Andruszkow et al., Acta Phys. Pol. B 32, 2025 (2001).

[68] R. Hall-Wilton et al., *The CTD Tracking Resolution* (unpublished). ZEUS-99-024, internal ZEUS-note, 1999.

[69] E. Bernardi et al., Nucl. Inst. Meth. A 262, 229 (1987).

[70] F. Goebel, *Measurement of the Diffractive Contribution to the DIS Cross Section Using the ZEUS Forward Plug Calorimeter.* Ph.D. thesis, Univ. of Hamburg, Hamburg, Germany, Report DESY-THESIS-2002-002, 2001.

[71] ZEUS Collaboration, *The ZEUS detector, Status Report 1993*, edited by U. Holm (1993).

[72] H. Larsen, *Leading Proton Sprctrometer - Read-Out Controller*, CERN-LAA Internal Report (1994).

[73] E. Barberis et al., *A Fast Shaping Amplifier-Comparator Integrated Circuit for Silicon Strip Detectors*, SCIPP 92/40 1992.
E. Barberis et al., *A Low Power Bipolar Amplifier Integrated Circuit for the ZEUS Silicon Strip System*, SCIPP 92/35 1992.

[74] J, De Witt, *The Digital Time Slice Chip*, University of California, Santa Cruz, June 7, 1991.

[75] H. Bethe and W. Heitler, Proc. Roy. Soc. Lond. A 146, 83 (1934).

[76] M. van der Horst, Nucl. Phys., p. 149 (1990).

[77] K. Piotrzkowski and M. Zachara, *Determination of the ZEUS Luminosity in 1994* (unpublished). ZEUS-95-138, 1995.

[78] T. Haas, *Generation Monte Carlo events with MOZART*. ZEUS Note 92-021 (1992).

[79] R. Brun et al., *GEANT*3. Technical Report CERN-DD/EE/84-1,CERN, 1987.

[80] Els de Wolf (editor) et al., *ZGANA, ZEUS trigger simulation library*.

[81] P.R.B. Saull, *A Monte Carlo Generator for Deeply Virtual Compton Scattering at HERA*, 1999, available on *http://www-zeus.desy.de/physics/diff/pub/MC*.

[82] H. Abramowicz and A. Levy, Preprint DESY-97-251 (hep-ph/9712415), DESY, 1997.

[83] H. Spiesberger, *An Event Generator for ep Interactions at HERA Including Radiative Processes (Version 4.6)*, 1996, available on *http://www.desy.de/˜hspiesb/heracles.html*.

[84] T. Abe, Comp. Phys. Comm. 136, 126 (2001).

[85] F.W. Brasse et al., Nucl. Phys. B 110, 413 (1976).

[86] H. Burkhardt and B. Pietrzyk, Phys. Lett. B 356, 398 (1995).

[87] T. Sjöstrand, Comp. Phys. Comm. 82, 74 (1994).

[88] A. Mücke et al., Comput. Phys. Commun. 124, 290 (2000).

[89] K. Muchorowski, Ph.D. Thesis, Warsaw University, 1998 (unpublished).

[90] G.F. Hartner et al., VCTRAK (3.07/04): *Off-line Output Information*. ZEUS Note 97-064 (1997).

[91] P. de Jong, *Status of the Uranium Calorimeter Reconstruction Software*. ZEUS Note 92-019 (1992);
M. de Kamps, *Changes and extensions of the calorimeter reconstruction programme*. ZEUS Note 94-014 (1994).

[92] N. Tuning, *Proton Structure Functions at HERA*. Ph.D. Thesis, Amsterdam University, 2001.

[93] J. Ng and W. Verkerke, *An Overview of SRTD Analysis.* ZEUS Note 95-037 (1995).

[94] J.I. Fleck and K. Ohrenberg, *Electron Identification in the HES and a new way to determine the efficiency of electron finders.* ZEUS Note 95-009 (1995).

[95] A. Meyer, *Electron Energy Correction with the Presampler, Part I.* ZEUS Note 99-066 (1999);
A. Meyer, *Electron Energy Correction with the Presampler, Part II.* ZEUS Note 00-036 (2000).

[96] A. Caldwell, W. Liu and B. Straub, *BCAL Electron Studies Part II: Energy Scale Calibration.* ZEUS Note 98-018 (1998).

[97] R. Sinkus, *Measurement of the Proton Structure Function F2 from the 1994 HERA Data using a Neural Network for the Identification of the Scattered Lepton.* Thesis, Hamburg University,1994.

[98] R. Sinkus and T. Voss, Nucl. Inst. Meth. A 391, 360 (1997).

[99] T. Doeker, A. Frey and M. Nakao, *Electron Position Reconstruction - Update of the ELECPO routines.* ZEUS Note 94-123 (1994);
Ch. Amelung, *Electron Position Reconstruction in ZEUS: Further Update of the ELECPO Package (Based on 1995 Data).* ZEUS Note 96-093 (1996);
Ch. Amelung, *Electron Position Reconstruction in ZEUS: Another Update of the ELECPO Package (Based on 1995/96 Data).* ZEUS Note 97-053 (1997);
C. Catterall, F. Pelucchi, *Comparison of CTD and Calorimeter Measurement of the DIS Positron Angle in High Q2 Events.* ZEUS Note 97-056 (1997).

[100] S. Bentvelsen, J. Engelen and P. Kooijman, *Proc. Workshop on Physics at HERA*, W. Buchmüller and G. Ingelman (eds.), Vol. 1, p. 23, Hamburg, Germany, DESY (1992);
K.C. Höger, ibid, p.43.

[101] F. Jacquet and A. Blondel,*Proceedings of the Study for an ep Facility for Europe*, U. Amaldi (ed.), p. 391. Hamburg, Germany (1979). Also in preprint DESY 79/48.

[102] F. Goebel, *Measurement of the Diffractive Contribution to the DIS Cross Section Using the ZEUS Forward Plug Calorimeter.* Ph.D. thesis, Univ. of Hamburg, Hamburg, Germany,Report DESY-THESIS-2002-002, 2001.

[103] I. Grabowska-bołdt, *Measurement of Deeply Virtual Compton Scattering Using the ZEUS Detector at HERA.* Ph.D. Thesis, AGH Univ. of Science and Technology in Cracow, Report DESY-THESIS-2004-034, 2004.

[104] ZEUS Coll., J. Breitweg et al., Eur. Phys. J. C 6, 603 (1999); ZEUS Coll., J. Breitweg et al., Eur. Phys. J. C 14, 213 (2000).

[105] ZEUS Coll., S. Chekanov et al., *A Measurement of Inclusive Diffraction at HERA*, ZEUS paper in progress, July 2006, currently available on: (*http://www-zeus.desy.de/physics/phch/ZEUS/zep.html*).

[106] Thomas J. Santner, Diane E. Duffy *The Statistical Analysis of Discrete Data*, edited by Springer (1989).

[107] H1 Coll., C. Adloff et al., Phys. Lett. B 483, 360 (2000).

[108] M. Capua, *Contribute at the Conference: Small x and Diffraction 2003*, Chicago, Sept. 2003 (*http://conferences.fnal.gov/smallx*);
M. Capua, *Contribute at the workshop: IFAE04*, Turin, April 2004 (*http://www.ph.unito.it/ifae*).

[109] H1 Coll., C. Adloff et al., Eur. Phys. J. C 13, 371 (2000).

[110] The 2007 European Physical Society Conference, Manchester (UK), 19-25 July 2007. Proceedings available on: *http://www.hep.man.ac.uk/HEP2007*

[111] V. Guzey, M.V. Polyakov, Eur. Phys. J. C 46, 151 (2006).

[112] D. Müller, *Pomeron dominance in deeply virtual Compton scattering and the femto holographic image of the proton*, arXiv:hep-ph/0605013.

[113] R. Fiore, L. Jenkovszky, V. Magas, and A. Prokudin, *Interplay between $Q^2$- and $t$ dependences in deeply virtual Compton scattering*, In the Proceedings of the Crimean conference *"New Trends in High-Energy Physics"*, Yalta, 10-17 September 2005.

[114] I.P. Ivanov, N.N. Nikolaev, A.A. Savin, *Diffractive Vector Meson Production at HERA:from Soft to Hard QCD*, Phys.Part.Nucl. 37, 1-85 (2006).

[115] E.S. Martynov, E. Predazzi, A. Prokudin, Phys. Rev. D 67, 074023 (2003).

[116] D.D. Coon, J.F. Gunion, Tran Thanh Van, R. Blankenbecler, *Phenomenology of High Momentum Trensfer Elastic Processes*, SLAC-PUB-1483 (September 1974), Phys. Rev.D 18, 1451 (1978).

[117] L.L. Jenkovszky, Z.E. Chikovani, Yad. Fizika 30 (1979) 531 (English translation: Sov.J. Nucl. Phys.);
A.I. Bugrij, Z.E. Chikovani, L.L. Jenkovszky, Z. Phys.C, *Particles and Fields*, 4, 45 (1980);
L.L. Jenkovszky, Nucl. Phys. B (Proc. Suppl.) 12, 317 (1990);
R. Fiore, L.L. Jenkovszky, V.K. Magas, and F. Paccanoni, Phys. Rev. D 60, 116003 (1999).

[118] V.A. Matveev, R.M. Muradyan, A.N. Tavkhelidze, Lett. Nuovo Cim, 7, 719 (1973).

[119] S. Brodsky and G. Farrar, Phys. Rev. Lett. 31, 1153 (1973).

[120] V.S. Fadin, E.A. Kuraev, L.N. Lipatov, Phys. Lett., B 60, 50 (1975);
I.I. Balitsky,L.N. Lipatov, Yad. Fizika 28, 822 (1978).

[121] L.L. Jenkovszky, Rivista Nuovo Cim., 10 (1987) 1;
M. Bertini et al. ibid 19 (1996) 1.

[122] R. Fiore, L.L. Jenkovszky, F. Paccanoni and A. Papa, Phys. Rev. D 65 (2002);
R. Fiore,L.L. Jenkovszky, F. Paccanoni and A. Prokudin, Phys. Rev. D 68, 014005 (2003).

[123] L. Csernai et. al., Eur. Phys. J. C 24, 205 (2002).

[124] P. Desgrolard, L.L. Jenkovszky, E. Paccanoni, Eur. Phys. J. C 7, 263 (1999).

[125] J. D. Bjorken and J. Kogut, Phys. Rev. D8, 1341 (1973).

[126] R. Fiore, L.L. Jenkovszky and V.K. Magas, *Generalized Parton Distributions, Analyticity and Crossing*, Nuclear Phys. B (Proc. Suppl.) 146 (2005).

# Acknowledgements

Many people gave a great effort to this work and I'd like here to thank all of them.

I'd like to thank my supervisor, Prof. Giancarlo Susinno for giving me the opportunity to become a member of the ZEUS Collaboration.

I due the most part of my scientific training to the Dr. Marcella Capua. I've not words enough to thank her for the constant support and guidance. Working together was a fulfilling experience!

I'd like to thank Prof. Enrico Tassi for all suggestions and support he offered to me during these three years of my PhD studies.

A special thank to Prof. Halina Abramowicz, Prof. Michele Arneodo, Dr. Marta Ruspa, Prof. Alexander Proskuryakov, Dr. Alessia Bruni and Prof. Aharon Levy, for all fruitful discussions and for helping me to solve several practical tasks during my analysis work.

Many thanks to all my Italian friends in Hamburg! A special thank to Lorenzo Rinaldi (who introduced me to the Data Quality Monitoring job!), Paolo Bellan, Marcello Bindi, Nicola D'Ascenzo, Michele Salvadore, Nicola Coppola. I kiss hands to all of you guys!

I cannot forget to thank my nice house owner Frau Erika Kader and my funny house mate Julia Grebenyuk for the nice time spent together.

I take this opportunity to thank Prof. Laszlo Jenkovszky, Prof. Roberto Fiore and Prof. Francesco Paccanoni for the exiting opportunity they gave to me to broad my research experience to the field of phenomenological models.

I share the office in Cosenza with two pretty mates, Evelin Meoni (my favourite shopping fellow) and Rossella Falcone. I'm sorry I disturbed very often your important conversations on the hair style physics and the theory of pretty boys and cooking, I hope you will forgive me one day!

Thanks to Tatjana Zivkovic, for nice variegate coffees and teas, the beautiful Norwegian experience and parties with Maria Fernanda Rivera Velasquez (your name is too long but many many many thanks!!! Long as well!) and thanks also to smurfette Kathrin Hopmann, I hope we'll meet again for a big ice-cream.

It is time now to say thank you to all my friends in Cosenza! Especially to Vincenzo and Amedeo Lavorini, Manuele Armentano, Gianluigi and Elisabetta Filippelli, Vincenzo and Manuela Ursino, Ilaria Guagliardi, Giuseppe Fiorita, Antonio Ferraro, Lorenzo Parrotta, Valentino Pingitore, Sarah Rudi, Rossana De Marco and the hundreds of other dear friends, I have everybody in my heart.

Many thanks to all my relatives and to my grand-fathers and grand-mothers watching me from the sky.

Last but obviously not least the best thank is to my parents. You always believed and supported me transmitting to me moral values and the love for the knowledge and learning; spending your days to grow up a good guy. I am proud to be your son!

Father of Heaven, God of Abraham, who created the world so beautiful and support us with the Holy Spirit Paraclete; Mother of Heaven, Theotokos, who lead us to your Son, our Salvation, the last line of this work is for you as my praise and prayer.